# Diffusion weighted MRI for tumor delineation in head and neck radiotherapy

Tim Schakel

**Diffusion weighted MRI for tumor delineation in head and neck radiotherapy**
PhD thesis, Utrecht University, The Netherlands

# Diffusion weighted MRI for tumor delineation in head and neck radiotherapy

**Diffusie gewogen MRI voor tumor intekening in hoofd-hals radiotherapie**

(met een samenvatting in het Nederlands)

Proefschrift

ter verkrijging van de graad van doctor aan de Universiteit Utrecht
op gezag van de rector magnificus, prof. dr. G.J. van der Zwaan,
ingevolge het besluit van het college voor promoties
in het openbaar te verdedigen
op donderdag 24 mei 2018 des middags te 2.30 uur

door

**Tim Schakel**

geboren op 16 juni 1987
te Oirschot

# Contents

# Chapter 1

# Introduction

## 1.1 Radiotherapy for head and neck cancer

In the Netherlands, head and neck cancer is diagnosed in approximately 3000 patients each year [1, 2]. Head and neck cancers typically originate from the squamous cells that form the mucosal layers. The most common subsites are the oral cavity, larynx, oropharynx and hypopharynx. In locally advanced head and neck cancers radiation therapy, or radiotherapy, is often the main treatment choice [3].

In radiotherapy high-energy ionizing radiation is used to destroy malignant tumor tissue. An optimal radiotherapy treatment delivers a high, lethal dose of radiation to the tumor while sparing the surrounding healthy tissue. The radiation, delivered by a linear accelerator, or linac in short, interacts with the tissue and causes DNA damage. When the dose is high enough, the cells will die. Generally, the higher the dose to the tumor cells, the higher the probability that these will be destroyed. A radiation treatment is typically divided into multiple fractions. Between the fractions, delivered on a daily basis, the healthy tissue will recover from the radiation dose whereas the tumor tissue, having reduced repair mechanisms, will have less recovery.

Radiation delivery techniques have developed from delivering large square fields to delivering complex dose distributions. These high-precision radiation delivery techniques, such as intensity modulated radiation therapy (IMRT) and volumetric modulated arc therapy (VMAT), allow for the creation of conformal treatment plans that sculpt the dose around the target area while reducing the dose to the surrounding healthy tissue (figure 1.1) [4]. For curative intent in
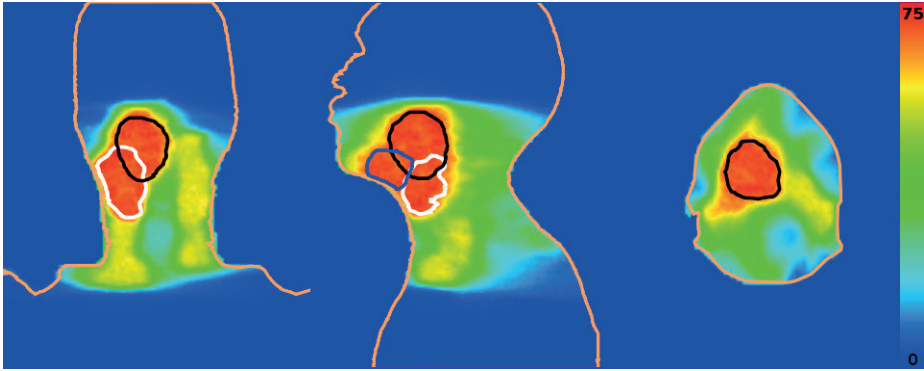
Figure 1.1: Example of a head and neck cancer treatment plan, showing a coronal, sagittal and transversal view of the 3D dose distribution. The planning target volume of the primary tumor is shown in black. The planning target volumes of two positive lymph nodes are shown in blue and white respectively. Units on the colorbar are in Gy.

head and neck cancer, the radiation dose to the target can be up to 70 Gy, typically delivered over 5 to 7 weeks in fractions of 1.5-2.3 Gy.

## 1.2  Target volume definition

An important requirement for the successful delivery of IMRT and VMAT treatments is the accurate and precise definition of the target [5–7]. The definition of the target volume is performed manually by a radiation oncologist, according to definitions suggested by the International Commission on Radiation Units and measurements (ICRU) [8]. First, the gross tumor volume (GTV) is delineated. This GTV is the gross demonstrable extent and location of the tumor. The GTV can be defined using information from clinical examinations and various types of three-dimensional imaging. The GTV is expanded into the clinical target volume (CTV), a volume of tissue that contains the demonstrable GTV with the addition of the presumed microscopic tumor spread, which cannot be observed or visualized. Typically, the GTV is expanded by a margin to define the CTV. The CTV is the region that is considered relevant for treatment. To ensure the prescribed dose is delivered to the CTV, an additional margin is added to form the planning target volume (PTV). The PTV is introduced to account for geometric inaccuracies, such as uncertainties in patient setup and tumor position. The uncertainties in patient setup are reduced through the use of individualized head supports and immobilization masks. This mask covers the head, neck and shoulders allowing for a more reproducible patient setup.

The additional margins added to the GTV can result in large treatment

volumes, which make it difficult to spare adjacent organs at risk (OAR). In the head and neck region, the salivary glands are important OAR. When irradiated, they can lose their functionality and the result is xerostomia, the sensation of dry mouth [9]. Therefore, it is not only important to include all tumor tissue in the treatment volume, but also to keep the overestimation to a minimum while doing so. Large treatment volumes will most likely include all tumor tissue, but consequently large amounts of healthy tissue will also be irradiated, potentially resulting in severe complications.

## 1.3   Imaging for target volume delineation

In modern radiotherapy, imaging is essential for target delineation. And as the treatments are delivered with the patient in an immobilization mask, all imaging should also be performed in such a mask to reflect the situation at time of treatment as much as possible. And in the case of multi modality imaging, to allow for accurate registration between the different modalities. Currently, computed tomography (CT) is widely used for GTV delineation. CT images reflect differences in the attenuation of x-rays. The benefits of CT are that it has a high imaging speed, high spatial resolution, excellent geometrical accuracy, it is relatively cheap and widely available. Additionally, CT also provides electron density information, essential for the dose calculations in radiotherapy planning. The main disadvantage of CT is the poor soft tissue contrast.

Positron emission tomography (PET) is another frequently used imaging modality for head and neck cancer patients. In PET positron emitting tracers are injected in the patient. The most commonly used tracer is $^{18}$F-fluorodeoxy-glucose (FDG), a glucose analog. Consequently, FDG-PET allows for visualization of differences in the uptake of glucose or metabolic activity. Since tumors typically demonstrate higher glucose healthy tissue, which yields images with a high tumor-to-background ratio. This makes these images suitable for automatic segmentation of the target and numerous different methods have been described in literature [10–12]. Yet, little consensus on which method is most suitable seems to exist. Additionally, the spatial resolution of PET is relatively low. In order to optimally combine PET and CT images, PET scanners are often combined with CT scanners, providing an intrinsic image registration between the two modalities. Moreover, the tissue densities from the CT images can be used for attenuation correction of the PET signals.

Besides CT and PET, magnetic resonance imaging (MRI) is increasingly used in target delineation [13, 14]. MRI has superior soft tissue contrast when compared to CT and is also capable of generating multiple different image contrasts. Furthermore, MRI does not use ionizing radiation during image acquisition. In contrast to CT and PET, an MRI can be acquired with many different endogenous contrasts, such as T1-weighted (T1w), T2-weighted (T2w), proton density
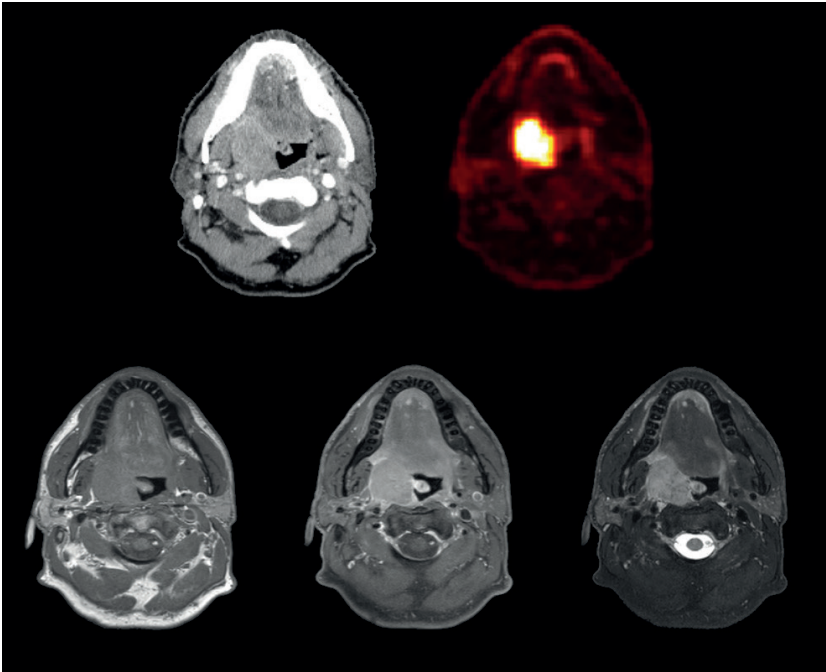
Figure 1.2: Example of different imaging modalities of a patient with an oropharyngeal tumor prior to treatment. All imaging was performed in the immobilization mask. Top row: CT after contrast injection and FDG-PET. Bottom row: T1w, T1w with fat suppression after gadolinium contrast agent injection, T2w with fat suppression.

and T2* weighted. The most commonly used MRI images are T1w and T2w images. The contrast in these scans is based on differences in the T1 and T2 magnetic relaxation rates respectively. Additionally, exogenous contrast agents can be injected during an MRI examination which shorten the relaxation rates in the tissues in which the contrast agent distributes. The most commonly used contrast agents contain gadolinium, which shortens the T1 relaxation rates. The increased use of MRI in radiotherapy is underlined by the introduction of hyrbrid MR-Linac systems [15, 16], which integrate radiation treatment machines with MR systems, offering MRI images at the time of treatment.

## 1.4 Diffusion weighted MRI

Diffusion weighted MRI (DW-MRI) is an MRI technique that provides information on the microscopic mobility of water in tissues. The contrast is endogenous; it does not require the administration of a contrast agent. Driven by thermal equilibrium, water molecules are constantly moving, the so-called Brownian mo-

tion. The distance water molecules travel, or rather diffuse, given a certain time period can be characterized by the diffusion coefficient (expressed in mm$^2$/s). In free water, as in a glass of water, at body temperature the diffusion coefficient is 3.0 mm$^2$/s following a Gaussian distribution. This means that after 50 ms, about 32% of the water molecules traveled 17 μm, while only 5% has traveled 34 μm or more [17]. In biological tissues however, the free diffusion of water molecules is hindered due to the presence of obstacles such as cell membranes, macromolecules and extracellular tortuosity. Thus the diffusion coefficient derived from DW-MRI images will no longer reflect the free diffusion coefficient of water and will deviate from the Gaussian distribution. The apparent diffusion coefficient (ADC) was introduced to emphasize this effect [18]. Tissues with more obstacles will restrict the motion of water and will thus show contrast with the surrounding, less restricting tissues. As tumors generally have an increased cellularity and higher degree of tissue disorganization, they will exhibit more restriction of water diffusion. Tissues that restrict the diffusion will appear bright on diffusion weighted images and will consequently have a low ADC value (figure 1.3).

## Acquisition of diffusion weighted MRI

The MRI signal can be diffusion weighted through the inclusion of motion or diffusion sensitizing magnetic field gradients in the MRI sequence [19]. These gradients are inserted before and after a refocusing radiofrequency (RF) pulse in a standard T2w spin echo sequence (figure 1.4a). Following the initial excitation RF pulse, the excited magnetization will start to dephase. The initial diffusion sensitizing gradient will introduce a spatially dependent dephasing on this magnetization. Following the refocusing RF pulse, the magnetization starts to rephase again. The second diffusion sensitizing gradient is identical to the first one and will thus introduce a similar rephasing effect, resulting in echo signal formation (figure 1.4b). If however, water protons have displaced between the first and second diffusion sensitizing gradient, they will, due to the spatially dependent gradient, experience a slightly different rephasing effect. This imbalance between dephasing and rephasing will result in an attenuated echo signal (figure 1.4c). The signal attenuation is proportional to the distance the water protons displaced between the dephasing and rephasing gradients: the more displacement, the larger the imbalance between dephasing and rephasing, and the more the signal attenuation.

Diffusion sensitizing gradients can only encode for diffusion along the direction in which the gradient is applied. In DW-MRI the restriction of the free diffusion of water is assumed to be isotropic, i.e. the restriction is the same in all directions, contrary to diffusion tensor imaging for example, where the directional dependence of diffusion is measured. Therefore, the acquisition of a diffusion weighted image is typically repeated three times, with the diffu-
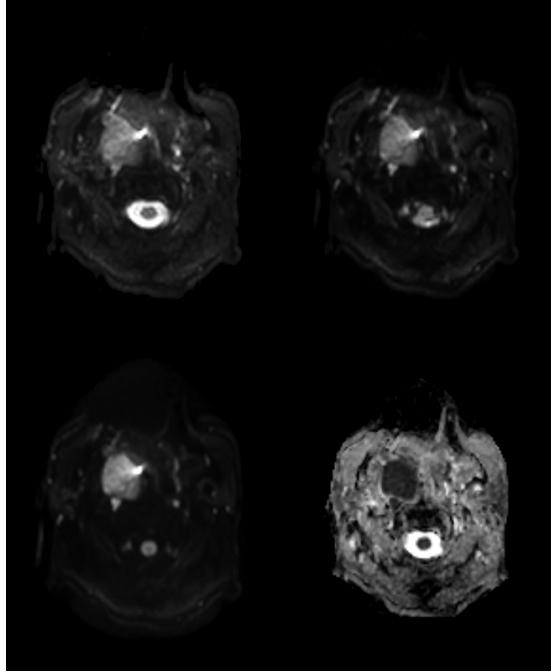
Figure 1.3: Diffusion weighted MRI, with different diffusion weightings and a calculated ADC map. The primary tumor exhibits diffusion restriction; it shows high signal intensity on the diffusion weighted images and low values in the corresponding ADC map. Top row: b = 0 s/mm$^2$ and b = 200 s/mm$^2$, bottom row: b = 800 s/mm$^2$ and ADC map.

sion sensitizing gradients in three different, orthogonal, directions, generating an isotropic diffusion weighted image. The strength and duration of the diffusion sensitizing gradients determine the amount of diffusion weighting encoded into the MRI acquisition. This is expressed in the b-value of the acquisition:

$$b = \gamma^2 G^2 \delta^2 \left( \Delta - \frac{\delta}{3} \right) \qquad (1.1)$$

with $\gamma$ the gyromagnetic ratio, $G$, and $\Delta$ and $\delta$, the strength and timings of the diffusion sensitizing gradients respectively [20, 21]. This expression is valid for rectangular gradient waveforms and can be expanded for trapezoidal waveforms. Typically, multiple acquisitions with increasing b-values are performed in order to estimate the ADC values. The desired b-value is achieved by increasing the gradient strength to the appropriate value, while keeping the timings of the sequence constant. With increasing b-value, the amount of diffusion weighting is increased and the measured signal will be increasingly attenuated. This signal attenuation as a function of b-value can be described as a mono exponential
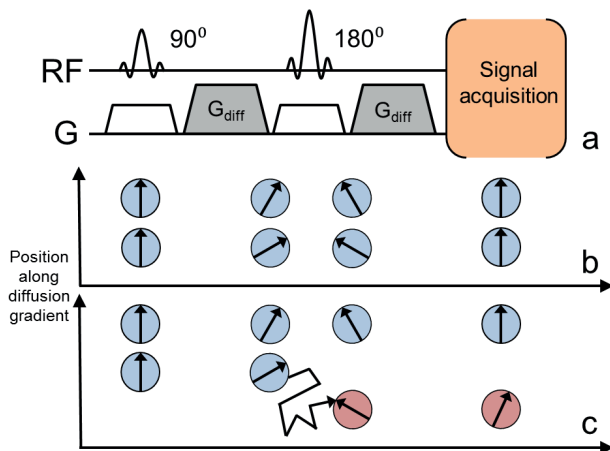
Figure 1.4: Illustration of a diffusion weighting MRI sequence diagram. The sequence diagram shows the timing of the diffusion sensitizing gradients ($G_{diff}$) with respect to the RF pulses (a). Bottom: dephasing and rephasing of spins at different positions along $G_{diff}$. The spins experience a different dephasing due to their different position along $G_{diff}$. The static spins have an equal rephasing effect (b). The moving spin experiences a different rephasing (c).

decay:

$$S = S_0 e^{(-bADC)} \tag{1.2}$$

with $S$ the measured signal in a voxel and $S_0$ the signal without diffusion weighting in the voxel [18].

## Echo planar imaging

As there is a lot of data, multiple directions and b-values, to be acquired in a DW-MRI series, the signal acquisition module is preferably very fast. Most commonly, signal acquisition is done using single shot echo planar imaging (EPI), where an entire slice is acquired following a single excitation RF pulse and subsequent diffusion encoding [22,23]. DW-EPI is thus very fast and efficient. However, it is also sensitive to image artefacts, especially geometrical distortions. In single shot EPI, the bandwidth in the phase encoding direction is very limited. Consequently, in regions with off-resonance effects, such as magnetic field ($B_0$) inhomogeneities, this can lead to errors in the spatial encoding of EPI: geometrical distortions [24–26]. The head and neck region is characterized by strong anatomical variations and air-tissue interfaces, giving rise to large susceptibility variations which result in large magnetic field inhomogeneities.

## Turbo spin echo

DW-MRI can also be acquired using a single shot turbo spin echo (TSE, also known as fast spin echo (FSE) and rapid acquisition with relaxation enhancement (RARE) [27]) sequence [28–30]. This sequence also acquires an entire 2D slice after a single excitation and diffusion preparation, however, it utilizes RF pulses in order to refocus the signal between consecutive echoes. The advantage of this is increased geometric accuracy, which is comparable to standard anatomical imaging that also utilizes TSE. The disadvantage is in acquisition speed, which is several factors lower in TSE than in EPI. Additionally, combining an TSE sequence with diffusion sensitizing gradients is less straightforward than with EPI.

The inclusion of RF refocusing pulses for every readout line adds a significant amount of time to the acquisition. Depending on the type of RF refocusing pulse used, this can be in the order of 1 to 5 ms per line. Compared to a DW-EPI sequence, it can take up to 5 times longer to acquire the same amount of data with DW-TSE. Moreover, since there is no data acquired during the RF refocusing pulses, the SNR per unit time is also lower. Furthermore, the addition of RF refocusing pulses increases the energy deposition in the subject. When the energy deposition would exceed safety limits, scan times are prolonged to remain within acceptable levels. In order to prevent this, the RF refocusing pulse angles are often decreased to much less than 180°.

Another challenge is maintaining a stable echo train, even with RF refocusing pulses smaller than 180°. Lower refocusing angles give rise to stimulated echo pathways that will contribute to the signal. TSE sequences are typically acquired under the Carr Purcell Meiboom Gill (CPMG) conditions, which dictate timings and phase relations of the RF pulses [31]. As part of the CPMG conditions, the MG phase condition requires that in a TSE sequence with echo spacing $\tau$, the magnetization at time $\tau/2$ should be aligned with the RF refocusing pulse. If this is not the case, the echo amplitudes will attenuate rapidly resulting in signal loss. From the MG phase condition, the magnetization at the start of the echo train can be divided into two components: MG and non-MG. For the non-MG component, the magnetization starts perpendicular to the RF refocusing pulse and destructive interference will arise between spin echoes and stimulated echoes, causing signal loss (figure 1.5). In DW-TSE, subject motion during the diffusion sensitizing gradients will results in a spatially varying, phase error, which consists of unknown amounts of MG and non-MG components. Moreover, this unknown phase error changes with every shot. Several approaches have been proposed to mitigate the effects of the non-MG component and create stable echo trains.

Phase cycling of the RF refocusing pulses in one of these approaches. This allows for a more stable echo train in the presence of phase errors [33,34]. These
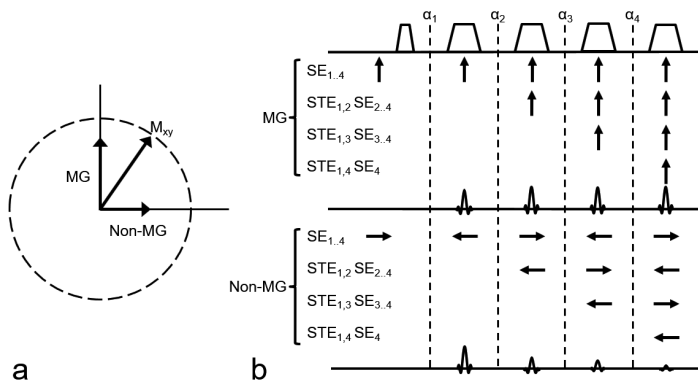
Figure 1.5: a) The transverse magnetization ($M_{xy}$) at the start of the echo train following motion during the diffusion sensitizing gradients. The magnetization is decomposed in a MG and non-MG component. b) Signal pathways for the MG (top) and non-MG component (bottom), following subsequent refocusing pulses ($\alpha_n$). $SE_{1..4}$ represents a pure spin echo train. $STE_{1,2}SE_{2..4}$ is the stimulated echo from RF pulse 1 and 2 and the subsequent spin echoes. The signal will interfere constructively for the MG component but destructively for the non-MG component due to the phase opposites, causing rapid signal decay (figure adapted from Schick and Jones [20, 32]).

methods however, often require high refocusing flip angles, which is an issue due to SAR limitations.

Alsop proposed a method to remove to non-MG component from the signal at the start of the echo train [35]. First a dephasing gradient is applied to create equal amount of MG and non-MG magnetization in each voxel. Following this dephasing gradient, a 90° reset pulse is applied in order to rotate the non-MG component to the longitudinal axis. The echo train will thus only consist of MG magnetization, which will lead to stable echo trains, also with refocusing pulses lower than 180°. Note, that this method does come at the cost of half the signal.

Another group of methods is known as echo parity selection [36]. The echoes formed in the pathways following the refocusing pulses can be divided into two groups: having experienced an odd or even number of refocusing pulses. These two groups form distinct echo parities. By using an imbalanced readout gradient (i.e. the dephaser gradient area is not half the readout gradient area), these echo parities can be separated in time. If the imbalance is large enough, one of the echo parities will displaced out of the readout window. Using this method, known as U-FLARE [37], stable echo trains are formed, but at the expense of half the SNR and it requires several dummy echoes for the signal to be stable.
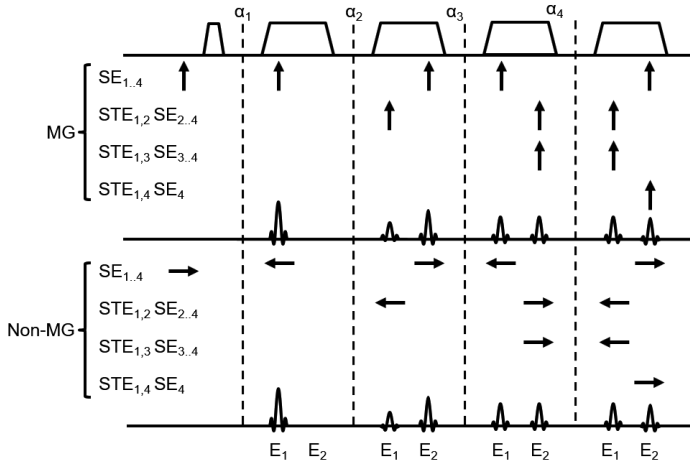
Figure 1.6: Signal pathways for the MG (top) and non-MG component (bottom), following subsequent refocusing pulses ($\alpha_n$). $SE_{1..4}$ represents a pure spin echo train. $STE_{1,2}SE_{2..4}$ is the stimulated echo from RF pulse 1 and 2 and the subsequent spin echoes. For both the MG and non-MG component, the echo parities $E_1$ and $E_2$ are separated in time. And for each parity the echoes have the same phase and will thus add constructively (figure adapted from Schick and Jones [20, 32]).

An different approach on parity selection was proposed by Schick [32]. After separation of the echo parities in time by an imbalanced readout gradient, they are both acquired separately (figure 1.6). Each acquisition is reconstructed separately and combined using magnitude averaging, This method is know as SPLICE (split acquisition of fast spin echo signals). Because both echoes are acquired in the same echo spacing, the SPLICE method does require an increased readout bandwidth, or an increased echo spacing. Additionally, some extra time is needed between the acquisition of the two parities to ensure they do not overlap. In practice, this is not a limiting factor due to the required hardware switching times. Moreover, like in U-FLARE, some dummy echoes are needed for the signal to stabilize.

## Fat suppression

Fat suppression can be performed by exploiting differences between water and fat. The short time inversion recovery (STIR) technique uses differences in T1 relaxation rates between water and fat. By applying an inversion pulse at the start of the sequence and waiting the appropriate time before the excitation pulse, fat can be removed from the signal. This generally results in good fat suppression, independent of magnetic field homogeneity. The disadvantage of

STIR are the reduced SNR, increased acquisition time and altered image contrast. The difference in resonance frequency between water and fat can also be used for fat suppression. Selective inversion (SPAIR) or excitation (SPIR) of the fat resonance can also remove the unwanted fat signal. SPIR fat suppression is most commonly used with DW-MRI because of its low penalty on acquisition speed. However, the performance of these methods suffers greatly from magnetic field inhomogenieties. Another method which utilizes the difference in resonance frequency between water and fat is the water-fat separation, also known as Dixon methods [38]. By acquiring data at different echo times, the water and fat signals will have a different phase with respect to each other. Using post processing algorithms the water and fat signals can be separated and water-only and fat-only images can be produced. Water fat separation is more robust for magnetic field inhomogeneities [39, 40].

## 1.5    Thesis outline

This thesis investigates the use of diffusion weighted MRI for tumor delineation in head and neck radiotherapy.

In chapter 2 the most commonly used sequence to acquire DW-MRI, echo planar imaging, is evaluated for geometric accuracy in the context of GTV definition. A retrospective analysis was performed on B0 maps from a patient dataset in order to quantify the geometric distortions in the GTV. It is shown that when using DW-EPI, severe distortions are present in the GTV area.

Given these severe distortions using the conventional sequence, a different sequence is proposed in chapter 3. A DW-TSE sequence, DW-SPLICE, is implemented and demonstrated in patients. This chapter also discusses some of the difficulties of adding diffusion weighting gradients to a TSE sequence. Diffusion weighted images with excellent geometrical accuracy were acquired of head and neck patients imaged in treatment position.

In chapter 4 the DW-SPLICE sequence is assessed in target volume delineation. Delineations made using DW-SPLICE were evaluated for interobserver variation and compared with automatic segmentations on FDG-PET. The target volumes from DW-SPLICE showed good interobserver agreement and a substantial overlap with the automatically segmented PET.

Chapter 5 presents an extension of the DW-SPLICE sequence in an attempt to improve the fat suppression. Within the sequence, additional acquisitions are performed at different echo times. This yields a dataset which is suitable for water fat separation. The results from the water fat separation are applied in order to provide a more robust and homogenous fat suppression in the head and neck region.

Initial results of pathological validation of DW-MRI are shown in chapter 6. Following total laryngectomy, the surgical specimen was digitally reconstructed to a 3D volume and registered to the in-vivo imaging prior to surgery. The specimen was stained and delineated by a pathologist under a microscope. This pathology delineation could then be projected onto the in-vivo imaging in order to assess their accuracy.

Finally, the most important results of this thesis are summarized and discussed in chapter 7.

# Chapter 2

# Diffusion weighted MRI in head and neck cancer: geometric accuracy

Schakel, Tim
Hoogduin, Hans M.
Terhaard, Chris H.J.
Philippens, Marielle E.P.

## Abstract

Introduction: The aim of this study is to assess the geometric accuracy of DW-MRI by quantification of geometric distortions in the GTV in HN cancer.

Materials & Methods: A retrospective analysis was performed on the data of 23 patients (with 24 lesions). For these patients, magnetic field maps and DW-MRI were acquired. The magnetic field maps were converted to voxel displacement maps. GTV delineations were transferred onto these voxel displacement maps and the voxel shifts in the GTV were analyzed.

Results: The median shift was 3.2 mm and the maximal posterior and anterior shifts were up to 15.0 and 26.0 mm respectively. The range of shifts varied from 11.8 to 25.6 mm. The percentage of GTV voxels that showed a shift of at least 6 mm was found to be 23.2%.

Conclusions: Current DW-MRI images of HN tumors show severe distortions up to centimeters, which restricts the use of DW-MRI scans for GTV definition in RT treatment planning.

# Introduction

Accurate target definition is a crucial step in radiotherapy (RT) planning. Generally, tumor definition is performed on CT. Interobserver studies showed a low concordance and pathological validation showed large overestimations of head and neck (HN) tumors [41,42]. Even with the addition of metabolic (FDG-PET) and soft tissue (MRI) information to CT this process of GTV definition remains challenging and a possible source of error [41–43].

In recent years, diffusion weighted (DW) imaging has been introduced in HN oncology, for diagnosing primary tumors [44, 45], nodal involvement [46] and recurrences [47]. DW-MRI has shown potential as a biomarker for early treatment response and response monitoring [48,49] and has recently been used to study target definition for dose escalation [50]. The high contrast between tumor and surrounding tissue in heavily diffusion weighted MRI nominates this technique as a promising potential candidate to facilitate the GTV definition in RT planning [51].

The diffusion contrast reflects the underlying micro-anatomical organization of a tissue. This contrast is based on differences in the restriction of the free diffusion of water molecules. When compared to normal tissue, tumors show an increased restriction of water diffusion due to an increased cellularity, tissue disorganization and increased extracellular space tortuosity [52]. This results in high signal intensity in tumors on DW-MRI.

However, the use of DW-MRI for GTV definition in radiotherapy is hampered by geometric distortions. These distortions are especially profound in the HN area where air-tissue transitions cause susceptibility differences leading to large magnetic field ($B_0$) inhomogeneities [23,24]. While these distortions are a known artefact in DW-MRI, their severity and extent has not yet been reported on in the context of GTV definition.

These distortions originate from the technique for geometric encoding in MRI. This is based on the resonance frequency and phase of the signal, which result from the underlying magnetic field. In areas of magnetic field inhomogeneities, this will lead to the assignment of an incorrect position to a voxel. For DW-MRI, data is generally acquired using echo planar imaging (EPI), which is particularly sensitive to magnetic field inhomogeneities. This will disturb the geometric encoding mainly in one direction, the phase encoding direction. The magnetic field can be determined directly and, with information from the EPI sequence, it can be applied to quantitatively estimate the voxel shifts and thereby the geometric distortions [53].

Geometric accuracy is vital in RT planning. While the geometric accuracy is well established for conventional MRI, DW-MRI potentially suffers from ge-

ometric distortions, which are known to be severe in regions with air-tissue transitions. The aim of this study was to quantify the geometric accuracy of DW-MRI in the GTV in HN cancer.

## Materials & Methods

### Patients

In this retrospective study, data from 23 HN cancer patients with a total of 24 lesions (Supplementary table 2.1), scanned between April 2011 and March 2012 at our department, was analyzed. For these patients, both a magnetic ($B_0$) field map and DW-MRI were acquired during the standard RT treatment planning scan protocol.

### Imaging

MR imaging was performed on a 3. 0T MRI scanner (AchievaTX, Philips Healthcare, Best, The Netherlands) using laterally placed Flex-M receive coils. Patients were scanned in treatment position in their RT immobilization mask to reduce motion artifacts and to improve image registration with other modalities.

$B_0$ field maps were acquired using a 3D mDixon FFE sequence; 3-point Dixon with separate acquisitions; $\Delta$ TE 1 ms; flip angle 20°; TR/TE 5.7/2.0 ms; acquired voxel size 2.0 x 2.0 x 2.0 mm$^3$; FOV 250 x 250 x 150 mm$^3$; SENSE factor 2; acquisition time 0m42s. The field maps were calculated directly on the scanner [54].

Diffusion weighted images were acquired using single-shot, single refocused, spin-echo EPI: EPI factor 43; phase encode direction anterior-anterior; max b-value 800 s/mm$^2$ with 6 averages; 3 b-values (0, 150, 800 s/mm$^2$) in total with diffusion encoding in 3 orthogonal directions; TR/TE 3699/66 ms; acquired voxel size 3.0 x 3.0 mm$^2$; reconstructed voxel size 0.98 x 0.98 mm$^2$; slice thickness 3.0 mm; total number of slices 40; FOV 250 x 250 x 120 mm$^3$; SENSE factor 2; Bandwidth/voxel (phase encode) 35 Hz; acquisition time 2m35s. Attention was paid to assure that the shimming and the frequency offset of the DW-MRI was equal to that of the $B_0$ field map. To account for exponential decaying eddy current, the default eddy current compensation of the system was used. This utilizes gradients of opposite polarity to counter the effects of eddy currents both in the gradient shape, the so-called preemphasis, and during the EPI train.

For the radiation treatment of the patient, the GTV was delineated by a HN radiation oncologist based on contrast enhanced CT, FDG-PET, T2 weighted MRI and T1 weighted MRI before and after contrast administration (Figure 2.1a-c). All scans were performed in RT immobilization mask.

## Data analysis

For each patient, the acquired $B_0$ field map was resampled to the resolution of the DW-MRI scans. Using the bandwidth of the DW-MRI scans, the $B_0$ field maps were subsequently converted to voxel displacement maps [53]. After image registration of the CT to the MRI, GTV delineations were transferred onto these voxel displacement maps and the expected shifts in the GTV were analyzed (Figure 2.1d).

From each GTV, the median, minimum and maximum estimated shift was calculated, as well as the range (difference between maximum and minimum) of shifts within a GTV. Phase encoding direction was performed in the anterior-posterior (AP) direction, such that positive shifts can be interpreted as a shift in A, while negative shifts can be interpreted as shifts in P. The shifts were further analyzed by calculating which percentage of the GTV volume was estimated to have a shift of at least a certain value. These thresholds were chosen based on the acquired voxel size, ranging from 1 to 5 voxels (or 3 to 15 mm respectively).

Using the voxel displacement maps, a distorted GTV volume was estimated. The volumes of these distorted GTV volumes were compared with the original, undistorted GTV volumes using a Bland-Altman plot. The derived voxel displacement maps were used to retrospectively correct the geometric distortions. This was done using the FUGUE software package [55].

## Results

The $B_0$ field maps of all patients showed a similar pattern. Large deviations were found in areas that were in or close to air, e.g. the nasal and oral cavity and the laryngeal space. The median volume of the GTV was 13.6 ml (range: 0.9 - 76.2 ml). All GTVs showed shifts, an example of a distorted DW-MRI is given in Figure 2.1e. Shifts were found both in the anterior and the posterior direction, with wide ranges; up to several centimeters (Supplementary figure 2.1).

The median shift of the GTVs was found to be 3.2 mm (approximately one voxel), while the maximal posterior and anterior showed shifts up to 15.0 mm (175.1 Hz) and 26.0 mm (303.7 Hz) respectively (Figure 2.2). The ranges of shifts within a GTV varied between 11.8 mm and 25.6 mm with a median of 19.8 mm. The median GTV volume percentage that showed a shift of at least 6 mm was found to be 23.2% (Figure 2.3), indicating that large parts of the GTV have significant shifts.

Bland-Altman analysis showed that the distortion introduced a volume increase of 4.6% on the average distorted GTV volume (Figure 2.4). Retrospective correction resulted in smearing in the images. The high signal intensity in the
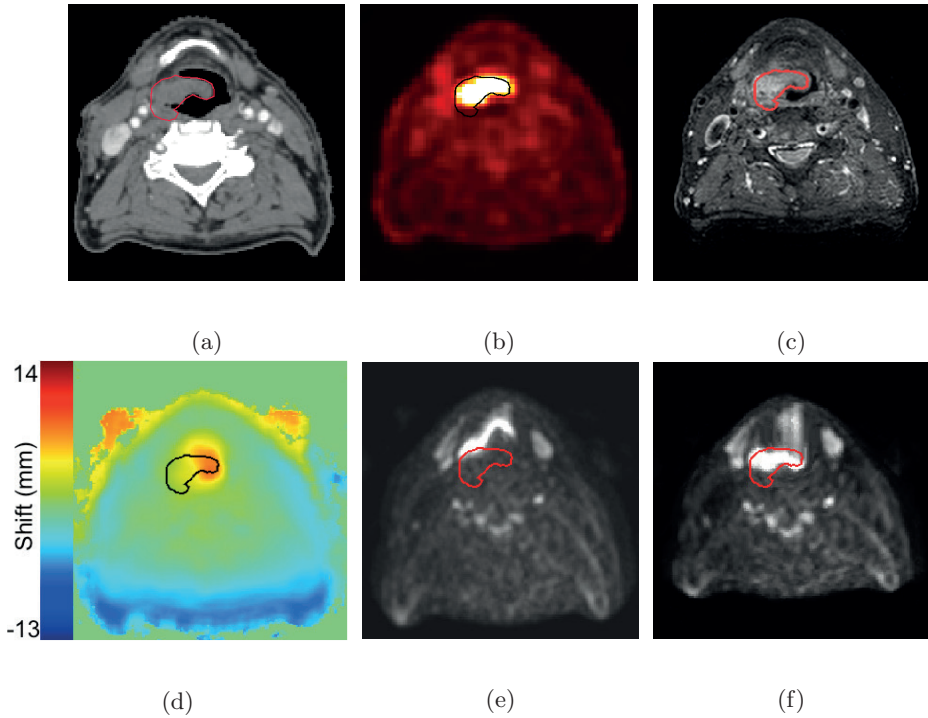
Figure 2.1: MR images of a patient with a T2 hypopharyngeal tumor. Clinical gross target volume (GTV) is shown in black or red and is located close to an air cavity. The tumor delineation is transferred after registration from the contrast enhanced CT **(a)**, to FDG-PET **(b)**, T1w MRI **(c)** with gadolinium, voxel displacement map **(d)** and the DW-MRI (b800 image) **(e)**. The voxel displacement map **(d)** shows large shifts at the position of the GTV. The DW-MRI (b800 image) shows the distortion **(e)**. Corrected DW-MRI using the voxel displacement map, the smearing effect is clearly visible **(f)**.

corrected DW images and the GTV did not entirely coincide. Mostly, the clinical GTV was larger than the volume with a high signal intensity in DW-MRI. An example is given in Figure 2.1f.

## Discussion

This study investigated the geometric accuracy of DW-MRI in HN tumors, by quantifying the distortions. DW-MRI has potential to facilitate GTV definition for these tumors. However, its acquisition, with the commonly used EPI technique, is hampered by geometric distortion.

Geometric distortions were found in all patients. Since squamous cell carci-
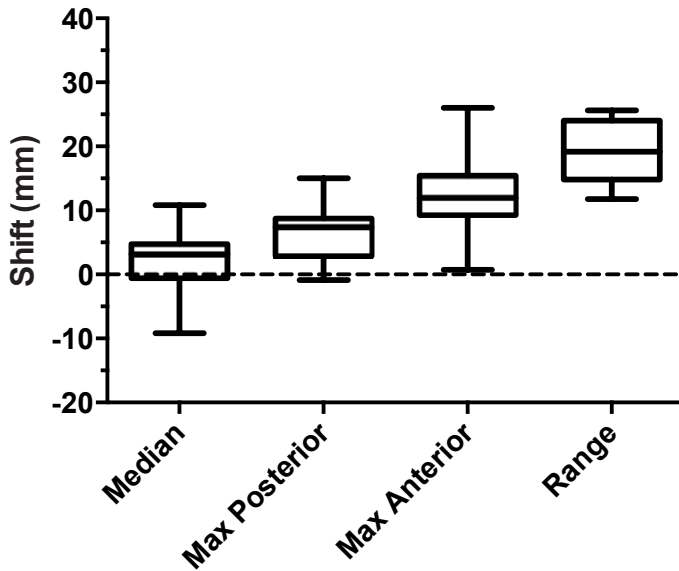
Figure 2.2: Combined voxel shifts in the gross tumor volume (GTV) from all patients. For each patient, the median, maximal posterior and anterior shift and the range of shifts within each GTV was calculated and their distribution is shown.

noma originate from epithelial layers that line the oral, pharyngeal and laryngeal cavity, most head and neck tumors were close to air cavities. In these areas of tissue transition, the magnetic field is disturbed, due to susceptibility differences, which is translated in voxel shifts in the diffusion weighted images. In an EPI sequence the voxels shift primarily in one direction, the phase encode direction, which was in the AP direction in the present study. Voxel shifts were found in both A and P direction due to the sign of the gradient in the magnetic field and the median shift was quite small: 3.2 mm. However, maximal A and P shifts up to 26.0 mm were found. This is also reflected by the large ranges. Large ranges indicate large differences between shifts within a GTV and thus more deformation.

The retrospective correction method which we tested, uses voxel displacement maps to unwarp DW images. However, these methods do not perform well in case of large distortions such as in the HN region. The reason for this is, that in the acquired (distorted) image, multiple voxels can accumulate in a single voxel. After retrospective correction, this accumulated signal intensity is distributed in the intermediary voxels. This can lead to smearing artifacts because information of the original signal intentsity in the individual voxels is lost.
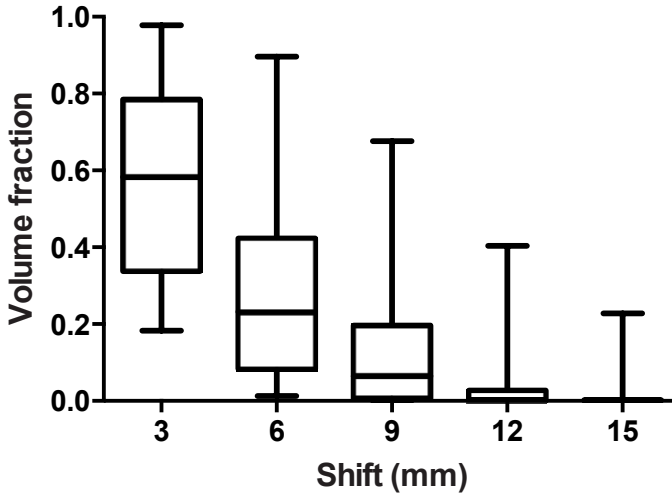
Figure 2.3: Percentage of the gross tumor volumes with a displacements of 1 to 5 voxels as calculated from the voxel displacement maps.

All the voxel shifts were evaluated in the GTV delineated for clinical treatment. We know from previous studies that this volume is overestimating the pathological tumor volume and that a mismatch between the GTV and pathological tumor tissue can occur [41, 42]. Since we lack information on the pathological tumor volume and position, it was not possible to evaluate the correction algorithm in depth in the present study. Non-concordance of the high signal intensity in the DW image and the clinical GTV will not necessarily mean that the correction failed. Therefore, we limited the analysis to a qualitative assessment of the corrected images.

Single shot EPI is the working horse for DW-MRI acquisition; it is very fast and has good signal-to-noise ratio. However, EPI acquisitions are inherently sensitive to susceptibility artifacts leading to image distortions. There are several options to reduce the distortion in DW-EPI images. The first is to further optimize the DW-EPI sequence, by increasing the bandwidth per voxel. This could be done by shortening the readout train, which can be achieved by applying parallel imaging. For the current setup however, this method was already employed and further options for sequence optimization are limited. Development of better hardware, e.g. a receive coil with more arrays that can be used in combination with a positioning mask could increase the parallel imaging factor further. Another method to shorten the readout train is to use a multi-shot acquistion. However, since DW imaging is a technique sensitive to motion, this will lead to motion artifacts between the shots.
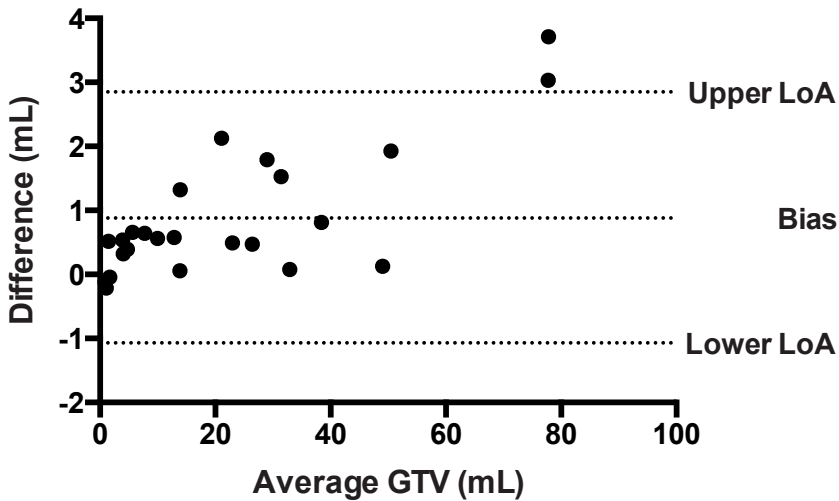
Figure 2.4: Bland-Altman plot of the estimated changes in volume due to deformation. The difference is defined as the distorted minus original gross tumor volume. The bias, upper and lower limits of agreement (95%) are shown as dotted lines.

A second option to reduce image distortion in DW-EPI images is to improve local magnetic field homogeneity. In clinical practice this is achieved by adjustment of the local field with field gradients, referred to as shimming. First and second order shims can be applied at 3T. Several vendors are developing image based shimming methods to optimally estimate gradient coil currents. However, air-tissue transitions and irregular shape in head and neck tumors will cause susceptibility differences that lead to steep gradients in the magnetic field. These are difficult to correct using shimming techniques.

There are various alternatives to acquire DW-MRI that are less sensitive to magnetic field inhomogeneities. Fast spin echo based sequences can provide a good alternative for EPI sequences. The drawback is that they are significantly slower and have lower signal-to-noise ratio. The benefit is that fast spin echo is very robust when it comes to geometric accuracy [56]. However, also here clever data acquisition, parallel imaging and reduced sampling of k-space might improve image quality and scan time.Another alternative is to use steady state free precession sequences. These are also geometrically more robust than EPI, but the signal in these sequences has a relatively complicated dependence on T1, T2, and the flip angle which makes analysis and quantification difficult [57].

Besides the described magnetic susceptibility also time varying eddy currents are also a potential source of image distortion. These eddy currents are induced

currents in the scanner resulting from fast switching of strong gradients, as is typically done in DW-MRI sequences. Using the default eddy current compensation of the system, preemphasis and compensating gradients during the echo train, the effects of these currents are minimized. The influence of eddy currents is considered small when compared to the susceptibility related distortions in the head and neck region. The $B_0$ off set was around 10-25 Hz for eddy currents [58] while we found median susceptibilty induced $B_0$ off sets of 86.5 Hz and 139 Hz in posterior and anterior directions respectively.

Accurate GTV definition is a crucial step in radiotherapy treatment planning which remains challenging. Mostly, CT is used and FDG-PET or MRI can be added. However, MRI based GTV definitions are known to overestimate the GTV [41, 42]. The contrast in DW-MRI reflects the micro anatomy of the underlying tissue and contains different information than the traditional MRI contrasts. Preliminary results showed that DW-MRI was a good estimator of tumor volume and geometric coincidence with the tumor on pathology in these cases where the geometry was not distorted [51]. After the geometric accuracy has been improved, pathological validation of the DW-MRI technique is required to test whether the diffusion contrast helps to reduce tumor volume overestimation.

## Conclusion

Current DW-MRI images of head and neck tumors show severe distortions, up to centimeters. These distortions currently restrict the application of EPI-based DW-MRI scans for GTV definition in RT treatment planning of head and neck cancer.

## Supplementary material

Supplementary table 2.1: Patient characteristics. The patient categorized under 'Other' is a squamous cell carcinoma of the cheek with perineural growth.

| Tumor location | T-stage | Number of lesions |
| --- | --- | --- |
| Hypopharynx | T1 | 1 |
| | T2 | 2 |
| | T3 | 2 |
| Nasopharynx | T1 | 1 |
| | T3 | 3 |
| | T4 | 3 |
| Oropharynx | T2 | 3 |
| | T3 | 1 |
| Larynx | T2 | 2 |
| | T3 | 1 |
| | T4 | 3 |
| Salivary Gland | T3 | 1 |
| Other | T1 | 1 |
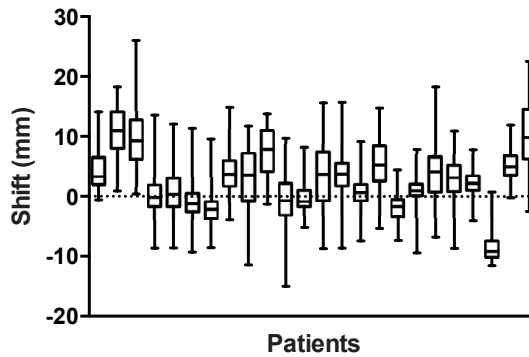


Supplementary figure 2.1: Voxel shifts estimated from magnetic field maps for each patient (n=24).

# Chapter 3

# Distortion free diffusion weighted MRI in head and neck radiotherapy

Schakel, Tim
Hoogduin, Hans M.
Terhaard, Chris H.J.
Philippens, Marielle E.P.

## Abstract

Introduction: Diffusion weighted (DW) MRI, showing high contrast between tumor and background tissue, is a promising technique in radiotherapy for tumor delineation. However, its use for head and neck patients is hampered by the poor geometric accuracy in conventional echo planar imaging (EPI) DW-MRI. An alternative turbo spin echo sequence, DW-SPLICE, is implemented and demonstrated in patients.

Materials & Methods: The DW-SPLICE sequence was implemented on a 3.0 T system and evaluated in 10 patients. The patients were scanned in treatment position, using a customized head support and immobilization mask. Image distortions were quantified at the gross tumor volume (GTV) using field map analysis. The apparent diffusion coefficient (ADC) was evaluated using an ice water phantom.

Results: The DW images acquired by DW-SPLICE showed no image distortions. Field map analysis at the gross tumor volumes resulted in a median distortion of 0.2 mm for DW-SPLICE, whereas for the conventional method this was 7.2 mm. ADC values, measured using an ice water phantom were in accordance with literature values.

Conclusions: The implementation of DW-SPLICE allows for diffusion weighted imaging of patients in treatment position with excellent geometrical accuracy. The images can be used to facilitate target volume delineation in RT treatment planning.

# Introduction

With the increased precision of radiotherapy (RT) treatment delivery, it is becoming increasingly vital to accurately define the target. In head and neck (HN) cancer, Computed Tomography (CT) and Magnetic Resonance Imaging (MRI) based target definition show high interobserver variation. Target volumes determined on CT and MRI are largely overestimated as shown in pathological validation studies [59, 60].

Diffusion weighted (DW) MRI is a functional imaging technique that provides information on the local mobility of water in tissue. Dense tissues with an increased cellularity, such as glandular and nodal structures or tumors, will restrict the motion of water and show high contrast with surrounding tissue [23]. Due to the high contrast on a DW image between a tumor and its surrounding tissue, DW-MRI shows great potential to facilitate target definition [51].

The main reason why DW-MRI is not more widely used for target definition in radiotherapy treatment planning of primary tumors is the poor geometrical accuracy of the technique [61], especially around air cavities. Air-tissue interfaces give rise to strong susceptibility variations which cause large local magnetic field inhomogeneities. Conventional DW-MRI is performed using the single shot echo planar imaging (EPI) technique, which is very fast and provides a good signal-to-noise ratio (SNR). However, using this EPI technique in the presence of local magnetic field inhomogeneities can lead to image distortions up to centimeters [61].

To address these susceptibility induced image distortions, DW-MRI can also be acquired using Turbo Spin Echo (TSE) type imaging sequences. Here, the EPI acquisition module is replaced by a single shot TSE module, which improves the geometrical accuracy. TSE diffusion has been explored previously in the head and neck region for various applications. For the detection and assessment of cholesteatoma, the use of DW-TSE has been investigated rather extensively. Although there does not seem to be consensus on the precise DW-TSE imaging strategy, DW-TSE has been found to have a high predictive and added value [62, 63]. DW-TSE methods have also been applied in imaging the salivary glands [64], the assessment of abscess formation [65] and the differentiation between different types of lesions in the head-and-neck area [66–68]. In head and neck cancer, DW-TSE has previously been reported [56, 69–72] to detect and characterize lesions. The majority of the papers applying DW-TSE, report limited experimental details and the image quality is often sub-optimal.

The acquisition of TSE scans is performed under the Carr Purcell Meiboom Gill (CPMG) conditions. These conditions dictate the timings and phase relations in the sequence. The inclusion of diffusion weighting gradients in a TSE

sequence makes that the CPMG conditions are easily violated when subject motion is present. This motion leads to phase errors which will result in destructive interference between spin echoes and stimulated echoes, creating unstable TSE trains and ultimately signal loss or even signal voids in DW-TSE images. Various approaches exist to deal with this issue and create stable echo trains. One is phase cycling of the refocusing pulses in an attempt to preserve the full signal [33]. Another method is echo parity selection, originally proposed by Norris et al [37], which aims to separate interfering echo contributions. One echo parity is eliminated by means of an RF pulse [35] or by shifting it out of the acquisition window using an imbalanced readout gradient (U-FLARE [37]). These methods lose a factor of two in signal. The echo parity selection method proposed by Schick [32], split acquisition of fast spin-echo signal for diffusion imaging (SPLICE), is similar to U-FLARE however, both echo parities are acquired and reconstructed separately and afterwards their signal magnitudes are combined. The acquisitions are shortened by slightly more than a factor of two to ensure the echo acquisitions do not overlap [32]. This increases the bandwidth, which reduces the sensitivity to distortions even further, but it also lowers the SNR. The resulting SNR is approximately a factor of two lower relative to a comparable CPMG acquisition. So far, only two studies from one research group [69, 71] have reported the use of DW-SPLICE in head-and-neck imaging. To improve the image quality, we moved to higher field strength and a dedicated radiotherapy simulation setup, to obtain images with good SNR within an acceptable acquisition time.

In this technical note we aim to expand upon the existing TSE based DW sequences by implementing and optimizing the DW-SPLICE sequence at a higher field strength (3.0 T). As these images are meant for target volume delineation prior to radiation treatment in head-and-neck cancer patients it demands high geometric accuracy.

## Materials & Methods

### MR imaging setup

MR imaging was performed on a 3.0 T wide bore MR system (Ingenia, Philips Healthcare, Best, The Netherlands) using 2-element Flex-M surface coils. Patients were scanned in treatment position using a personalized head support and 5-point head-and-shoulder immobilization mask [73] (figure 3.1).

Measurements were performed on an ice water phantom to validate ADC values. The phantom was built according to Chenevert et al [74], a spherical tube filled with demineralized water was inserted in a container filled with ice water. The sequence was tested in vivo and a total of 10 patients (7 oropharynx, 1 larynx, 1 hypopharynx and 1 nasopharynx) were included in the study approved

Figure 3.1: MR imaging setup. The patient is positioned using a personalized immobilization mask and head support, surface coils are placed against the sides of the mask.

by the institutional review board. These patients received an MRI exam for the purpose of RT treatment planning. We added the DW-SPLICE sequence to this exam.

### MR imaging sequences

Both DW-EPI and DW-SPLICE were performed as a multi-slice single-shot acquisition using 30 slices of 4 mm. In DW-SPLICE a center-out k-space encoding was used and the refocusing angles were gradually reduced to 60 degrees in the echo train. Diffusion weighting was applied in an isotropic fashion using 3 orthogonal directions with b-values between 0 and 800 s/mm$^2$. Fat suppression was executed using spectral presaturation with inversion recovery (SPIR). Both scanning protocols were individually optimized for image quality. Detailed parameters are given in table 3.1.

A B$_0$ field map was acquired to estimate geometrical accuracy. A 3D gradient echo sequence (flip angle 20°, TE 4.6 ms, $\Delta$ TE 2.3 ms, TR 9.5 ms) was used for this. The FOV, voxel sizes and shim settings were the same for both diffusion sequences. A gadolinium contrast enhanced T1w TSE multi-acquisition Dixon scan was used as anatomical reference.

An ice water phantom was used to measure ADC values [74]. DW-SPLICE and DW-EPI were acquired on the same scanner and with the same parameters as the patient imaging. The signal intensities from the E1 and E2 echo families varies during the initial echoes [32, 37, 75]. Therefore, an extra acquisition of DW-SPLICE was done using additional (5 total) leading dummy echoes.

Table 3.1: Sequence parameters used for the pharynx patient imaging. The FOV and related parameters varied slightly for larynx imaging and are denoted in round brackets.

| Scan | DW-SPLICE | DW-EPI |
|---|---|---|
| FOV (RL x AP x FH) [mm$^3$] | 230 x 280 x 120 (200x200x120) | 230 x 280 x 120 (230x230x120) |
| Acquired voxel size [mm$^2$] | 1.8 x 1.8 | 2.0 x 2.0 |
| Slice thickness [mm] | 4 | 4 |
| TE [ms] | 52 | 63 (61) |
| TR [ms] | 16366 (15844) | 3291 (3167) |
| SENSE acceleration factor | 2 | 2 |
| (Echo) train length {dummies} | 64 {1} (55 {1}) | 69 (57) |
| Bandwidth [Hz] | 900.3 (858.5) | 21.4 (26.7) |
| b-values [s/mm$^2$] {averages} | 0 {2}, 800 {5} | 0 {2}, 50 {2}, 100 {2}, 200{2}, 500 {4}, 800 {6} |
| Total acquisition time | 4m38s (4m29s) | 2m47s (2m41s) |

### Image evaluation

Image distortions can generally be attributed to gradient non-linearities, eddy current or magnetic field variations. The gradient non-linearities are specific for individual MR systems and independent of imaging sequence. The non-linearities were routinely measured using a specialized phantom for geometric fidelity (Philips Healthcare, Best, The Netherlands). The phantom has a diameter of 55 cm and is measured at 7 positions, 7 cm apart, with the central position being the isocenter of the magnet.

Eddy current related distortions were probed using DW acquisitions of a phantom. The diffusion weighting gradients were applied along the principal axes of the MR system (i.e. using only a single gradient axis per acquisition). The phantom was segmented on the b0 image. This contour was then projected onto the images with a high diffusion weighting in the different directions to visually inspect for geometrical deviations due to eddy currents.

Distortions due to magnetic field variations were investigated using B$_0$ field maps. The acquired B$_0$ field maps were processed using in-house developed software 5, 25. First, phase unwrapping was performed to account for phase wraps in the data. The unwrapped field map was converted to a pixel-shift map using the sequence parameters that dictate the effective spectral width per pixel [53]. Pixel-shift maps were converted to shift-maps in millimeters by multiplication with the voxel dimensions. For DW-EPI the shifts occur predominantly in the phase encoding direction, while for DW-SPLICE this is the frequency encoding

direction. In order to assess the distortions in the relevant areas, the delineated gross tumor volume (GTV), as defined for RT treatment planning, was projected onto the shift-maps. For each GTV, we calculated the median, minimum and maximum shifts over all voxels for both acquisition techniques. The results are given as the median value over all patients and a Wilcoxon signed rank test was used to test for differences.

To measure the ADC values, a region of interest (ROI) was defined in the center of the tube in the ice water phantom and this ROI was used to calculate the mean and standard deviation for each technique.

# Results

## Diffusion weighted imaging in patients

DW-MRI was successfully acquired in all patients. Two examples, patients 6 and 5 respectively, of the DW images obtained with the two different methods are shown in figure 3.2. The image distortions around the air cavities are immediately recognized in the DW-EPI scans (3.2b, 3.2f), while the DW-SPLICE scans (3.2c, 3.2g) show the accurate geometry. The diffusion contrast is present in both scans, with the tumor appearing bright on both b800 images and dark on the ADC map. Figure 3.3 shows the $B_0$ field map with the GTV delineation of the same patient as figure 3.2a-d. Additional imaging results, $B_0$ field maps and GTV delineations for all patients can be found in supplementary figure 3.1.

## Image distortions

For the MR system used in this study, routine QA measurements of geometric distortions due to gradient non-linearities were performed. For a central region of at least 25x25x28 cm$^3$, which a head-and-neck anatomy does not exceed, the geometric distortions due to gradient non-linearities were found to be smaller than 1 mm. Visual inspection of the phantom contours showed no deviations due to eddy currents in the DW-SPLICE sequence. For DW-EPI, the eddy currents did result in a minor deviation in the outline of the phantom. Distortion analysis showed that the median shift over all GTVs was 7.2 mm for DW-EPI, with a median minimum and maximum shift of -10.5 mm and 34.9 mm respectively. While for DW-SPLICE, the median shift over all GTVs was 0.2 mm with a median minimum and maximum shift of -0.3 mm and 1.0 mm respectively. Additional results for all patients can be found in supplementary table 3.1. The difference between the two techniques is statistically significant (p=0.002).
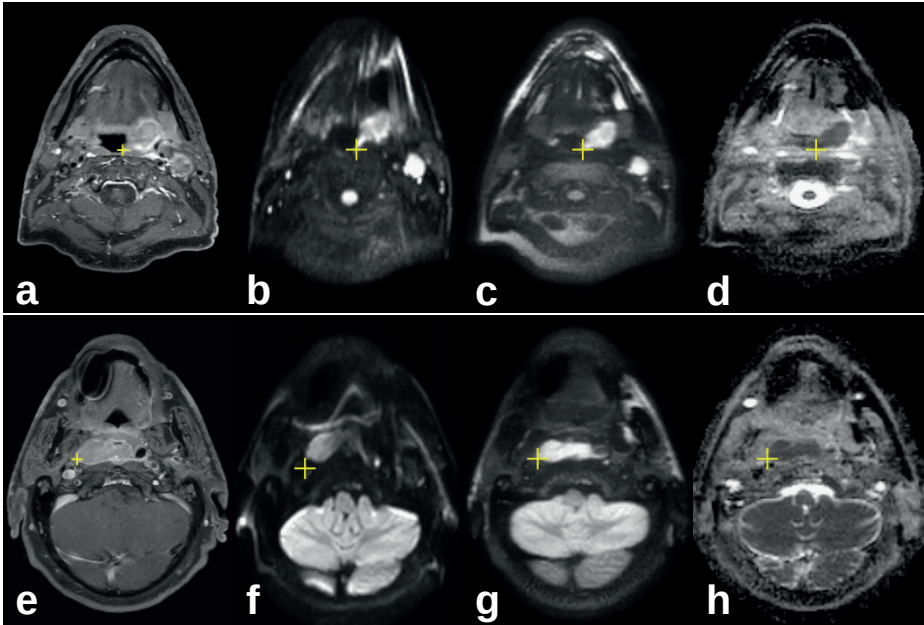
Figure 3.2: Examples of DWI in two patients, top row (a-d) T2N2b oropharynx, bottom row (e-h) T1N0 nasopharynx (with a dental implant causing a signal void). The yellow cursor is linked between different MR scans of the same patient. (a,e) T1w TSE Dixon, water image, with Gd contrast. (b,f) DW-EPI b800. (c,g) DW-SPLICE b800. (d,h) DW-SPLICE ADC map.

## ADC values

The ice-water phantom was scanned with the same sequences as was used for patient imaging (figure 3.4a). The mean ADC of conventional DW-EPI was 1.125 x $10^{-3}$ mm$^2$/s with a standard deviation of 0.032 x $10^{-3}$ mm$^2$/s. DW-SPLICE yielded 1.158 ($\pm$ 0.020) x $10^{-3}$ mm$^2$/s. While for DW-SPLICE with additional startup echoes the ADC was 1.132 ($\pm$ 0.016) x $10^{-3}$ mm$^2$/s. For DW-EPI and DW-SPLICE (with additional startup echoes) the ADC values were within 5% of the reported literature value [74] (figure 3.4b).

## Discussion

The main limitation that prevents DW imaging to be widely incorporated in a HN RT treatment planning setting is the poor geometrical accuracy of the conventional DW-EPI acquisition method. The main factor contributing to geometrical distortion in this region is magnetic field inhomogeneity; while the effects of gradient non-linearity and eddy currents were found to be much smaller. It

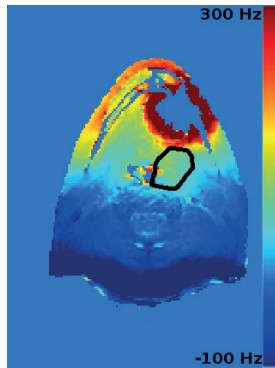Figure 3.3: Example of a $B_0$ field map, same patient as in figure 3.2a-d. The delineated GTV is indicated with the black line. For this patient, the median distortion was 7.40 mm for DW-EPI and 0.16 mm for DW-SPLICE.

was shown that when using the DW-SPLICE sequence, the geometrical accuracy is greatly improved. These susceptibility related distortions were found to be smaller than the acquired voxel size, 0.2 mm vs 1.8 mm for DW-SPLICE. The large difference in the bandwidths of the EPI and TSE sequences already indicates a large intrinsic difference in image distortions. However, as the distortions are related to the magnetic field inhomogeneities, they still need to be evaluated in the relevant area (GTV). The geometric accuracy of DW-SPLICE is comparable to standard anatomical imaging, which allows the diffusion information to be utilized during target volume delineation.

Different methods exist to address the image distortion issue. Techniques such as readout-segmented EPI [76] and reduced FOV imaging [77, 78] will increase the bandwidth of the DW-EPI. However, these approaches will not completely eliminate the image distortions as the magnetic field inhomogeneities around the head-and-neck tumors are often so large that an even larger bandwidth is required. Additionally, a reduced FOV approach is often undesirable due to potential lymph node pathology.

The ADC values as measured with the DW-SPLICE sequence in patients are higher than measured with DW-EPI (figure 3.3). During the initial echoes of the echo train of DW-SPLICE, there is still an intensity variation between consecutive echoes [32, 37, 75]. The addition of more dummy acquisitions at the start of the echo train reduces the intensity variations when the center of k-space is acquired. This will increase TE however, which leads to a reduced SNR. Since we focused on the use of DWI for target delineation, ADC values are used qualitatively to identify T2 shine through or image artefacts rather than quantitatively. Therefore, we chose to use the acquisition protocol with higher
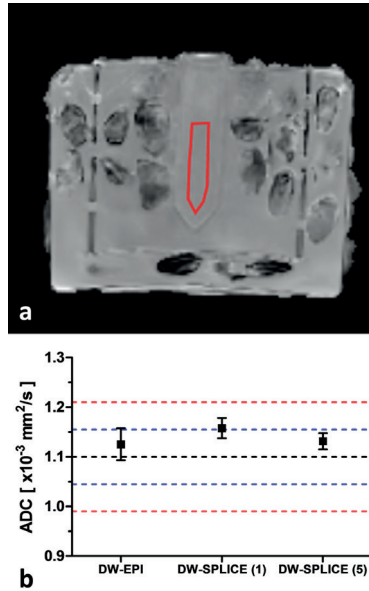
Figure 3.4: a) ADC map of the ice water phantom. The ROI is shown in red. b) ADC values within the ROI (mean ± standard deviation) of DW-EPI and DW-SPLICE with 1 and 5 leading dummy acquisitions. The blue and red dashed lines indicate 5 and 10% deviation respectively of the reference value (black dashed).

SNR in patients.

The main limitation of the DW-SPLICE sequence is its acquisition speed, a TSE acquisition is inherently slower than EPI. In the presented setup, the acquisition time of a single volume of diffusion data is 5 times longer for DW-SPLICE (16.4 s) than DW-EPI (3.3 s). This limits the amount of data (eg. b-values and/or averages) that can be acquired within a clinically acceptable time. DW-SPLICE will also show more blurring in the images due to T2 relaxation in the echo train of the single shot acquisition. To decrease the shot length and thus the amount of blurring, dedicated receive coils with more elements could be used to enable higher parallel imaging acceleration factors. This would also speed up the acquisition.

While good fat suppression still remains challenging in this anatomical region, the effects of failing fat suppression in DW-SPLICE are less severe than in DW-EPI. In DW-EPI, unsuppressed fat will suffer from both distortion and large water-fat shift artefacts, causing it to shift through the image and degrade image quality. An example of this is shown in figure 3.2f. In DW-SPLICE the unsuppressed fat will not shift and will have less impact on image quality. The

application of DW-SPLICE is not limited to the head-and-neck region and has been applied in other sites as well [69, 79–81]. In principle it can be applied to any anatomical region where conventional DW-EPI suffers from susceptibility related image distortions. Delineation studies and pathological validation of DW-MRI using DW-SPLICE are subject of future work.

## Conclusion

In conclusion, when compared to DW-EPI, the DW-SPLICE sequence has a significant increase in geometrical accuracy, eliminating image distortions. Using the DW-SPLICE sequence and a dedicated imaging setup at 3.0T to scan head-and-neck patients in treatment position, we could improve the quality and robustness of DW imaging to facilitate target delineation for RT treatment planning.

## Acknowledgements

## Supplementary materials

Supplementary table 3.1: $B_0$ distortion analysis of all 10 patients. For each patient the minimum, median and maximum image distortion (in mm) is given for both DW-EPI and DW-SPLICE respectively.

| Patient # | GTV (mL) | DW-EPI (mm) | | | DW-SPLICE (mm) | | |
|---|---|---|---|---|---|---|---|
| | | min | median | max | min | median | max |
| 1 | 14.44 | -9.15 | 1.47 | 18.83 | -0.17 | 0.03 | 0.44 |
| 2 | 7.63 | -1.88 | 17.24 | 38.25 | -0.04 | 0.37 | 0.82 |
| 3 | 6.97 | -8.50 | 9.39 | 33.70 | -0.24 | 0.20 | 0.73 |
| 4 | 25.92 | -26.71 | 6.91 | 32.91 | -0.69 | 0.19 | 0.89 |
| 5 | 18.19 | -12.00 | 10.86 | 56.81 | -0.25 | 0.23 | 1.21 |
| 6 | 19.38 | -9.14 | 7.40 | 43.15 | -0.16 | 0.16 | 0.94 |
| 7 | 6.42 | -6.65 | 5.65 | 36.07 | -0.28 | 0.12 | 0.78 |
| 8 | 6.69 | -12.21 | 1.87 | 22.19 | -0.48 | 0.04 | 0.90 |
| 9 | 63.10 | -24.84 | 7.97 | 47.75 | -0.53 | 0.17 | 1.01 |
| 10 | 5.01 | -13.28 | 6.98 | 31.84 | -0.42 | 0.20 | 0.82 |
| | | | | | | | |
| Median | 11.03 | -10.57 | 7.19 | 34.88 | -0.27 | 0.18 | 0.85 |
| Minimum | 5.01 | -26.71 | 1.47 | 18.83 | -0.69 | 0.03 | 0.44 |
| Maximum | 63.10 | -1.88 | 17.24 | 56.81 | -0.04 | 0.37 | 1.21 |
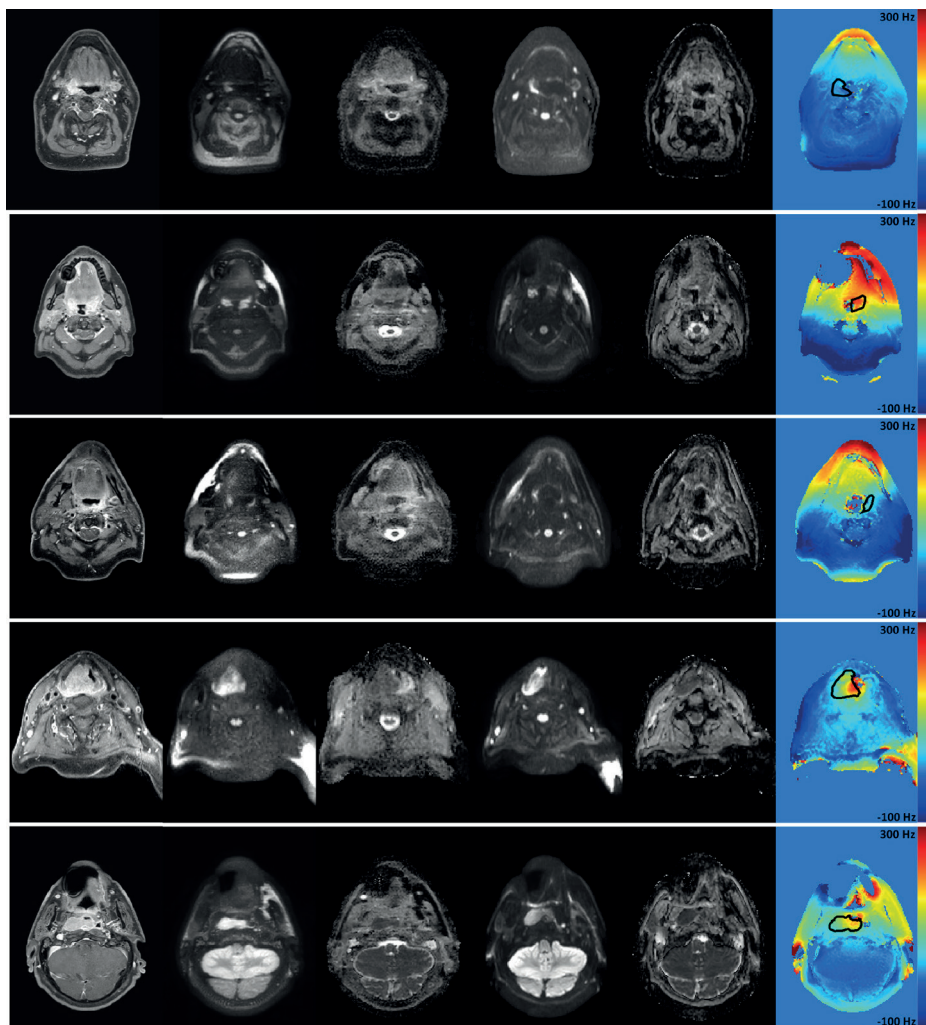
Supplementary figure 3.1: images from all 10 patients. From left to right: T1w mDixon TSE (water image); DW-SPLICE b800; DW-SPLICE ADC map; DW-EPI b800; DW-EPI ADC map; B0 field map. ADC maps are scaled linearly between 0.0 and 3.0 10-3 mm2/s. The delineated GTV (black line) is projected on the B0 field map.
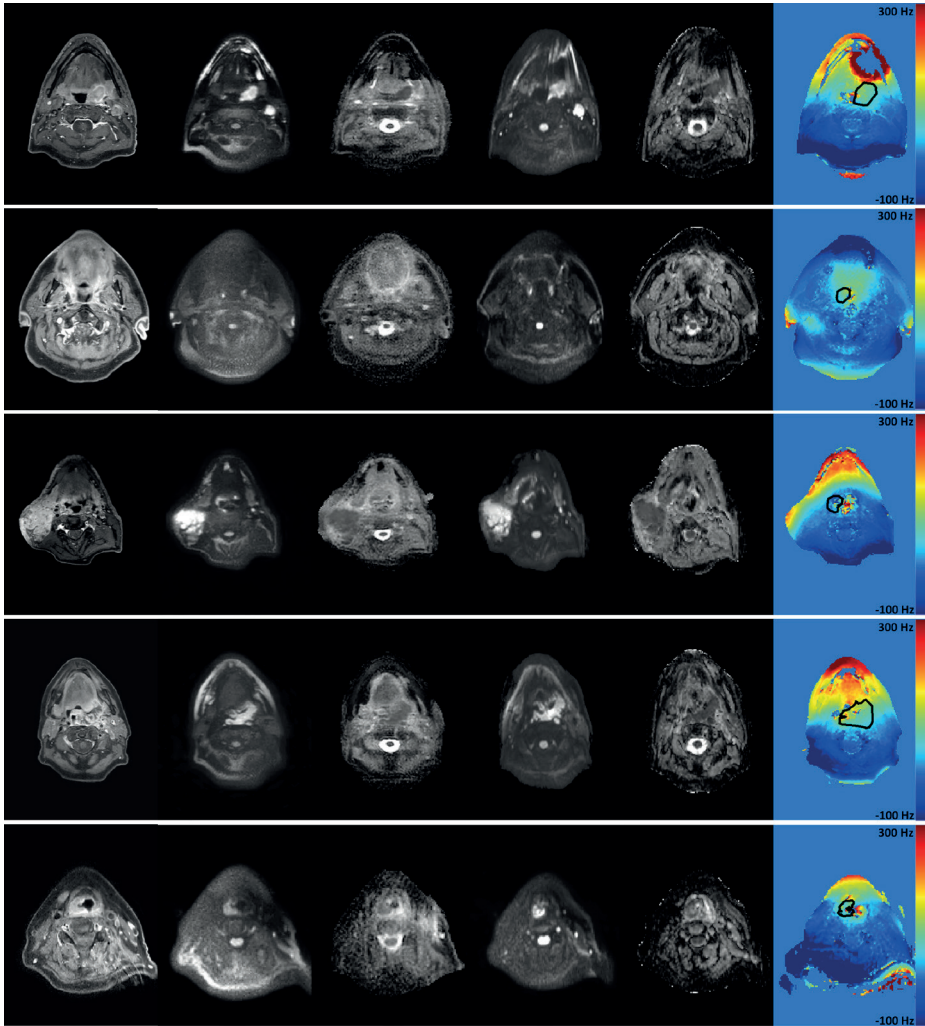
Supplementary figure 3.1 continued: images from all 10 patients. From left to right: T1w mDixon TSE (water image); DW-SPLICE b800; DW-SPLICE ADC map; DW-EPI b800; DW-EPI ADC map; B0 field map. ADC maps are scaled linearly between 0.0 and 3.0 10-3 mm2/s. The delineated GTV (black line) is projected on the B0 field map.

# Chapter 4

# Evaluation of DW-MRI for tumor delineation: comparison with PET

Schakel, Tim
Peltenburg, Boris
Dankbaar, Jan-Willem
Cardenas, Carlos E.
Aristophanous, Michalis
Terhaard, Chris H.J.
Hoogduin, Hans M.
Philippens, Marielle E.P.

## Abstract

Introduction: Diffusion weighted (DW) MRI may facilitate target volume delineation for head-and-neck (HN) radiation treatment planning. In this study we assess the use of a dedicated, geometrically accurate, DW-MRI sequence for target volume delineation. The delineations are compared with semi-automatic segmentations on $^{18}$F-fluorodeoxyglucose (FDG) positron emission tomography (PET) images and evaluated for interobserver variation.

Materials & Methods: Fifteen HN cancer patients underwent both DW-MRI and FDG-PET for RT treatment planning. Target delineation on DW-MRI was performed by three observers, while for PET a semi-automatic segmentation was performed using a Gaussian mixture model. For interobserver variation and intermodality variation, volumes, overlap metrics and Hausdorff distances were calculated from the delineations.

Results: The median volumes delineated by the three observers on DW-MRI were 10.8, 10.5 and 9.0 cm$^3$ respectively, and was larger than the median PET volume (8.0 cm$^3$). The median conformity index of DW-MRI for interobserver variation was 0.73 (range 0.38 0.80). Compared to PET, the delineations on DW-MRI by the three observers showed a median dice similarity coefficient of 0.71, 0.69 and 0.72 respectively. The mean Hausdorff distance was small with median (range) distances between PET and DW-MRI of 2.3 (1.5 - 6.8), 2.5 (1.6 - 6.9) and 2.0 (1.35 - 7.6) mm respectively. Over all patients, the median 95th percentile distances were 6.0 (3.0 - 13.4), 6.6 (4.0 - 24.0) and 5.3 (3.4 - 26.0) mm.

Conclusions: Using a dedicated DW-MRI sequence, target volumes could be defined with good interobserver agreement and a good overlap with PET. Target volume delineation using DW-MRI is promising in head-and-neck radiotherapy, combined with other modalities, it can lead to more precise contouring of the GTV.

## Introduction

Intensity modulated radiotherapy (RT) has allowed for conformal dose distributions, aiming to maximize the dose to the gross tumor volume (GTV) and minimize the dose to normal tissue. Accurate determination of the GTV is a key issue in radiotherapy [82] and forms the basis of treatment planning. However, it is also one of the major sources of uncertainty [6, 7, 83]. The accurate delineation of the GTV is a time consuming step, prone to errors. Delineations of the GTV using computed tomography (CT) and magnetic resonance imaging (MRI) show large variations between observers and an overestimation of the actual pathological tumor volume [59, 60, 84]. Additionally, FDG-PET has shown to result in more conformal segmentations than CT or MRI [42, 85].

To address the interobserver variation, automatic segmentation of the GTV would be ideal. Automatic segmentation is also preferable in online and/or adaptive MRI guided treatments. Several authors have proposed $^{18}$F-fluorodeoxyglucose (FDG) positron emission tomography (PET) as imaging modality for automatic segmentation [86–90] due to its high signal to background ratio. However, the use of PET for segmentation is challenging. The segmentations can depend on the contrast and noise characteristics of the PET images, which, apart from tumor characteristics, originate from different acquisition and reconstruction protocols [91, 92]. Additionally, a variety of segmentation algorithms have been proposed which result in large variations in target volumes [12, 86]. Therefore, successful automatic segmentation requires a careful choice of acquisition and reconstruction parameters and segmentation algorithms. Other drawbacks are the increased radiation burden, resolution limitations and relatively high costs.

Diffusion weighted (DW) MRI might be an alternative imaging modality for FDG-PET as DW-MRI generates images with high contrast between tumor and surrounding normal tissue making it a candidate to improve MRI based delineations and suitable for automatic segmentation. The contrast in DW-MRI is based on differences in the restriction of water diffusion on a microscopic level. The resulting high contrast images, along with the derived quantitative apparent diffusion coefficient (ADC) maps, could be used for delineation purposes [80, 93]. However, the geometrically accurate acquisition of DW-MRI in the head and neck region is difficult due to the presence of air cavities causing large magnetic field inhomogeneities. Using conventional DW-MRI, acquired with echo planar imaging (EPI), image distortions up to centimeters can arise [61]. Recently, we have proposed the use of an alternative DW-MRI sequence; split acquisition of fast spin-echo signal for diffusion imaging (SPLICE). Here, EPI is replaced with turbo spin echo for data acquisition, which leads to less distortions as it is relatively insensitive to magnetic field inhomogeneities introduced by the patient. The DW-SPLICE sequence has excellent geometric performance, allowing the

DW-MRI images to be used for target delineation [94].

As the overestimation of the tumor volume results in a high burden on normal tissues surrounding the tumor due to the large treatment volume, the tumor has to be segmented as close (conformal) as possible. By definition the GTV only includes macroscopic tumor tissue, and requires a clinical target volume (CTV) margin to encompass microscopic spread. To avoid normal tissue burden, the CTV needs to be minimized. Recently, Ligtenberg et al showed in an image validation study with pathology that GTVs automatically segmented from PET showed a tumor volume closest to the tumor volume on histology with a high coverage and the lowest overestimation [85]. Unfortunately, such validation studies cannot be performed in patients treated with primary radiotherapy. However, since the PET-based volume resembled the tumor volume best, and with the smallest overestimation, we chose to use PET-based segmentations as a reference to evaluate GTVs created using DW-SPLICE.

The aim of the present study was to assess the use of the dedicated DW-MRI sequence in target volume delineation. The GTVs were evaluated in terms of interobserver agreement, volume and spatial concordance with PET.

## Materials & Methods

### Patients

A total of 15 head and neck patients were included in this study, patient details are given in supplementary table 4.1. The institutional review board provided a waiver of consent. These patients, scheduled for RT treatment, underwent a clinical FDG-PET/CT and an MRI exam, both in treatment position using a personalized head support and 5-point head and shoulder immobilization mask [73].

### FDG-PET/CT imaging

Patients fastened 6 hours before imaging on a mCT-Biograph PET/CT scanner (Siemens Medical Solutions, USA). An FDG dose of 2.0 MBq/kg was injected 60 minutes before image acquisition. Image acquisition was done at 2 bed positions, at 4 minutes per position. Image reconstruction was done using an ordered subset expectation maximization algorithm, utilizing point-spread function and time-of-flight information, at a reconstructed voxel size of 2.04 x 2.04 x 1.5 mm$^3$ (AP x RL x FH) with body weight corrected standardized uptake values.

## MR imaging

MR imaging was performed on a 3.0 T Ingenia wide bore MR system (Philips Healthcare, The Netherlands) using 2-element Flex-M surface coils. The DW-SPLICE sequence was prototyped and loaded on the system, generating geometrically accurate diffusion weighted images [94]. Diffusion weighting was applied in an isotropic fashion using three orthogonal directions with b-values of 0 and 800 s/mm$^2$ (b0 and b800 respectively). ADC maps were generated on the MR system. Fat suppression was executed using spectral presaturation with inversion recovery. Detailed sequence parameters are given in table 4.1. The exam also contained T1 (with and without contrast) and T2 weighted TSE scans.

Table 4.1: Sequence parameters for the DW-SPLICE sequence. The protocol was adapted for laryngeal imaging (denoted in round brackets).

| Scan | DW-SPLICE |
|---|---|
| FOV (RL x AP x FH) [mm$^3$] | 230 x 280 x 120 (200x200x120) |
| Acquired voxel size [mm$^2$] | 1.8 x 1.8 |
| Slice thickness [mm] | 4 |
| TE [ms] | 52 |
| TR [ms] | 16366 (15844) |
| SENSE acceleration factor | 2 |
| Echo train length {dummies} | 64 {1} (55 {1}) |
| Bandwidth [Hz] | 900.3 (858.5) |
| b-values [s/mm$^2$] {averages} | 0 {2}, 800 {5} |
| Total acquisition time | 4m38s (4m29s) |

## Target volume delineations

For the acquired PET scans, the GTV was segmented semi-automatically using a Gaussian mixture model (GMM). With this method, voxels are classified based on statistical differences in their intensity distributions [95–97]. The GMM assumes independent observations, and models the image intensities with 10 Gaussian distributions. Following an initialization step by placing a selection box around the lesion, Gaussian distribution parameters are initialized automatically. The method was adapted for head and neck [96] by fully automating the initialization of the Gaussian distribution means as described in detail in previous publications [95–97]. Following initialization, the Gaussian distributions are fitted to the image intensities using maximum likelihood estimation method. The algorithm then classifies regions to either tumor or background, generating binary masks.

The GTV was delineated in the diffusion weighted images by three observers. First the hyperintense region on the b800 image was identified, this was aided

by a semi-automatic segmentation. On the b800 image, a seed point was placed centrally within the tumor and using a threshold of 50% of the maximum signal intensity, a region was segmented. Following this initial segmentation, the contours were manually adapted using the contrast of the ADC map, where the individual observers excluded regions of high ADC typically at the edge of the tumors. While doing this the b0 and b800 images were also available to the observers for reference. All contours (referred to as $DW_1$, $DW_2$, $DW_3$) were converted to binary masks.

Additionally, as all of the patients received radiation treatment following imaging, the target volumes were retrieved from the treatment plans for these patients ($GTV_{RT}$) as reference. The radiation oncologists mostly relied on CT and anatomical MRI (T1 weighted, with and without contrast, and T2 weighted), but PET and DW-MRI were also available.

## Data analysis

All scans from the MRI exam were matched with the PET/CT using rigid registration. The resulting transformations were used to resample both the PET and DW-SPLICE masks on the grid of the CT (0.98 x 0.98 x 2.0 mm$^3$), in order to compare the segmentations. While resampling the masks, the volume was kept the same on the new grid.

Using the resampled masks the delineated volumes for PET and DW-SPLICE were determined. For each observer the DW-MRI delineation was further compared to the PET segmentation by means of Dice similarity coefficients (DSC) and Hausdorff distance (HD) analysis. The DSC is a measure of spatial overlap and is defined as: $DSC(A, B) = \frac{2(A \cap B)}{A+B}$ where A and B are the respective delineated regions and $\cap$ is the intersection. A DSC of 0 indicates no spatial overlap at all and a DSC of 1 indicates complete overlap. The distance between two delineated contours is represented using the Hausdorff distance, which measures, for each point on a delineated contour, the Euclidean distance to the nearest point on the other contour. Per contour pair, the mean Hausdorff distance ($HD_{mean}$) and the 95$^{th}$ percentile distance ($HD_{95}$) were calculated. The results for each metric are given as the median (range) over all patients. We tested for significant differences (p < 0.05) in metrics using a Wilcoxon signed rank test.

For the inter-observer analysis of the DW-SPLICE delineations, a generalized conformity index ($CI_{gen} = \frac{\sum_{pairsij} |A_i \cap A_j|}{\sum_{pairsij} |A_i \cup A_j|}$ with $A_i$ and $A_j$ the respective delineated regions and $\cup$ the union) [98] over all observers was calculated per patient, because this metric is independent of the number of observers. Additionally, DSC were calculated per observer pair. Additionally, the HD analysis was also performed for the observer pairs as this metric is independent of the volume of the tumor and has clinical relevance as it is related to uncertainty

margins.

## Results

An example of the imaging data is given in figure 4.1, showing the correspondence between the different modalities as well as between the different observers on the diffusion weighted imaging. Additionally, anatomical T1 weighted images after gadolinium contrast agent injection are shown for reference. Initial semi-automatic segmentation of the b800 images proved difficult in three out of 15 patients, where the pixel intensity gradient was low around the tumor in images with limited SNR. For these patients, the tumor region was cropped manually to avoid other structures, such as unsuppressed fat, to be included in the region of interest.

### Volumes

The volumes found on the GMM segmentation of PET had a median volume of 8.0 cm$^3$ (1.2 - 38.9), while the DW-SPLICE volumes were larger for all three observers: DW$_1$ 10.8 (1.8 - 44.3), DW$_2$ 10.5 (1.8 - 38.1), DW$_3$ 9.0 (1.4 - 37.8) cm$^3$ (figure 4.2). The difference with PET was significant for DW$_1$ (p=0.0001) and DW$_2$ (p=0.0043), but not for DW$_3$ (p=0.0637). The median GTV$_{RT}$ was 15.63 cm$^3$, a significant difference compared to both PET and all DW-MRI volumes. An overview of all delineated volumes is given in supplementary table 4.2.

### Intermodality delineation overlap and distance analysis

The median (range) DSC of the PET segmentation with the each DW-MRI delineation was very similar for the three observers: 0.71 (0.03 - 0.80), 0.69 (0.03 - 0.79) and 0.72 (0.03 - 0.82) respectively (figure 4.3a). An overview of correspondence measures is given in supplementary table 4.2. The DSC was reasonable to good (0.44 - 0.82) in all but 2 patients; these were the patients with the smallest volumes. Patient 1 had practically no overlap between PET and DW-MRI. This patient showed two neighboring hotspots on PET, with the anterior one showing most tracer uptake so this region was segmented by the GMM method. On DW-MRI however, the posterior hotspot showed most diffusion restriction and low ADC (figure 4.1, bottom row). The other patient (number 2) showing poor correspondence, had a tumor located at the base of the tongue. The mismatch was mainly caused by tongue movement between the PET scan and MRI exam.

Using the same delineation pairs, distance analysis was performed (figure 4.3b and 4.3c) and both the HD$_{95}$ and HD$_{mean}$ were calculated. For all three observers the HD$_{mean}$ was small with median (range) distances between PET and DW-MRI of 2.3 (1.5 - 6.8), 2.5 (1.6 - 6.9) and 2.0 (1.35 - 7.6) mm respectively.
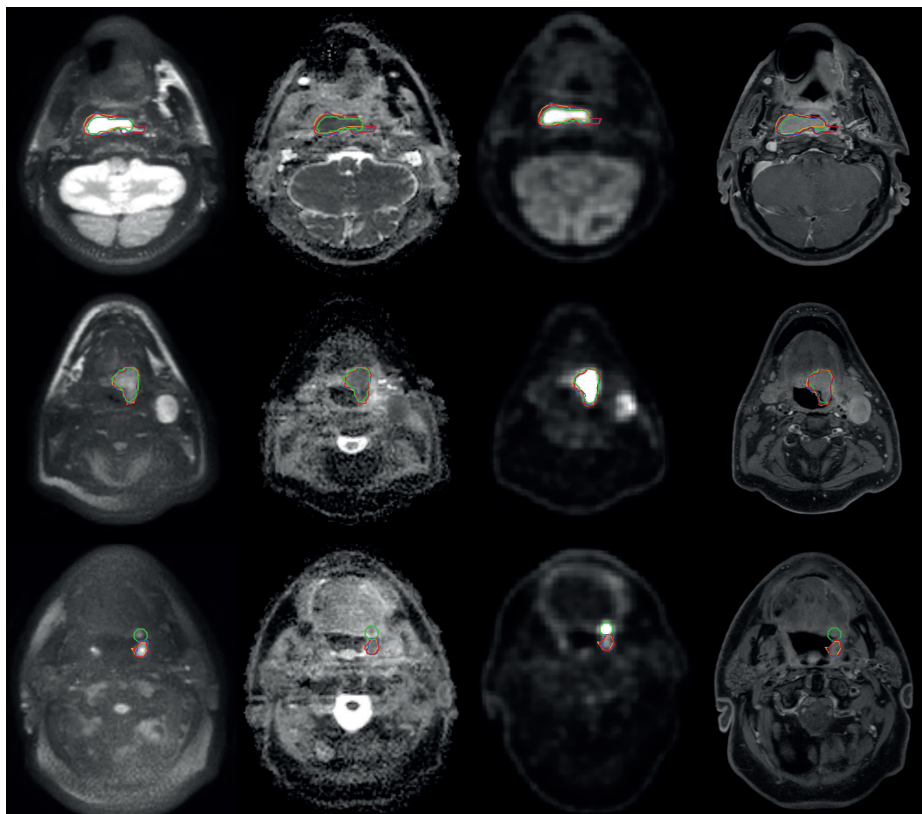
Figure 4.1: Patient examples showing the correspondence of the delineated target volumes. Each row of images is from a single patient and shows transverse slices with, from left to right: DW b800; ADC map; FDG-PET; T1 weighted TSE mDixon water reconstruction after gadolinium contrast agent injection. The images are taken from patient 9, 12 and 1 respectively. The delineations from FDG-PET (green), $DW_1$ (red), $DW_2$ (blue) and $DW_3$ (orange) are shown on all imaging.
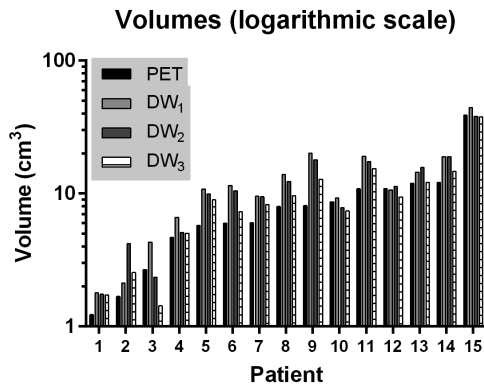
Figure 4.2: The delineated volumes per patient for the different observers and modalities. Patients were ranked in ascending order of the volume determined on FDG-PET.

Over all patients, the median $95^{\text{th}}$ percentile distances were 6.0 (3.0 - 13.4), 6.6 (4.0 - 24.0) and 5.3 (3.4 - 26.0) mm. Similar to the DSC, patients 1 and 2 showed the largest distances between the PET and DW-MRI contours.

## Interobserver agreement

The median $CI_{gen}$ over all patients was 0.73 (0.38 - 0.80) indicating good agreement among the different observers (figure 4.4a). This is also seen in the three pairwise DSCs, median (range): observer 1 and 2, 0.87 (0.52 - 0.90); observer 1 and 3, 0.83 (0.43 - 0.91); observer 2 and 3, 0.82 (0.59 - 0.87). Patient 2 and 3 showed the least interobserver agreement. These were patients with small tumor volumes, located in the oropharynx adjacent to lymphatic tissue (Waldeyers tonsillar ring). Figures 4.4b and 4.4c show the results of the distance analysis between observers. Generally, small distances, both $HD_{95}$ and $HD_{mean}$, were found between the observer pairs except for the two patients (2 and 3) which also showed reduced $CI_{gen}$.

## Discussion

In this study we assessed semi-automated target volume delineation in head and neck cancer patients using a non-EPI diffusion weighted MRI sequence, DW-SPLICE. Furthermore, we investigated the variation between different observers on DW-MRI as well as the agreement between DW-MRI and $^{18}$FDG-PET generated GTV delineations. The agreement between observers was good with a median $CI_{gen}$ of 0.73 and small distances between the individual contours (median $HD_{95} < 3.5$ mm). The delineated volumes on DW-MRI were found to be

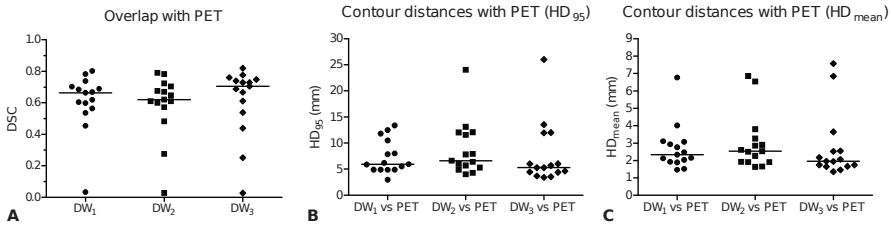Figure 4.3: The agreement between DW-MRI and FDG-PET as measured with Dice Similarity Coefficient (a), the 95th percentile contour distance (b) and the mean contour distance (c). The horizontal bars represent the median.

significantly larger (median volumes 10.8 cm$^3$, 10.5 cm$^3$ and 9.0 cm$^3$) than the PET segmentations (median volume 8.0 cm$^3$), nevertheless there was a substantial overlap between PET and DW-MRI with median DSCs of 0.71, 0.69 and 0.72 for the three different observers respectively. Both the PET and DW-MRI volumes were substantially smaller than the clinically used target volume, GTV$_{RT}$ (median volume 15.63 cm$^3$), which is known to overestimate the GTV [42, 85].

High b-value DW-MRI images have a similar appearance as PET images, which makes them relatively easy to interpret by the observers. This was demonstrated by the good agreement between the different observers in this study. The median CI$_{gen}$ over all patients was 0.73, where 0.7 is considered to be an indicator of good overlap [99]. The two cases showing a low CIgen concerned patients with small tumors located in the oropharynx, adjacent to lymphatic tissue. Lymphatic tissue shows diffusion restriction and thus has diffusion properties similar to that of tumors, i.e. showing high signal on high b-value DW-MRI images and a low ADC. Therefore, DW-MRI should always be used as an addition to high quality anatomical images. Other delineation studies in the head-and-neck area [100, 101] show lower or similar CI$_{gen}$ values. Jager et al. [60] showed 0.61 for laryngeal cancer using CT and 0.57 using CT/MR; Geets et al. reported 0.41 and 0.42 for laryngeal and oropharyngeal GTVs respectively [102]; Mukesh et al. reported 0.54 for CTV delineations on CT [103].

Despite the different biological background and acquisition method of DW-MRI and FDG-PET, there was a large overlap between PET and DW-MRI. For a large part both techniques identified the same target for treatment. Differences mainly occur at the edges of the delineated volumes, but the distances between the different contours were small in general. Over all patients, the median of the average distance between DW-MRI and PET contours was between 2.0 and 2.5 mm for the three different observers. For comparison, the acquired in-plane voxel sizes in DW-MRI and PET were 1.8 and 2.0 mm respectively. Furthermore, the PET GTVs, derived by the GMM segmentation, still require an appropriate
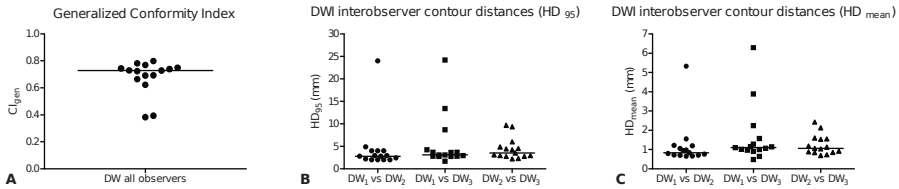
Figure 4.4: Interobserver agreement for all patients on diffusion weighted imaging, expressed as generalized conformity index (a), contour distances $HD_{95}$ (b) and $HD_{mean}$ (c). The horizontal bars are the medians.

CTV margin to encompass all microscopic tumor tissue. According to Ligtenberg et al. [85] this CTV margin is 5.2 mm in laryngeal and hypopharyngeal cancer. In a similar fashion, the DW-MRI GTV delineations will also require an appropriate CTV margin.

Generally, the difficulty of incorporating DW-MRI in the practice of target volume delineation in head-and-neck is the large geometrical distortion. To overcome this issue we used a dedicated sequence, DW-SPLICE, for the acquisition of diffusion images. Although this dealt with the geometrical distortions, some mismatch with other imaging modalities, like PET-CT can appear. Despite the fact that patients were fixated in an immobilization mask, some misalignment may remain since patients were scanned at two different time points. Additionally, internal motion of mobile structures due to breathing, tongue movement or swallowing can still occur. This could explain some of the differences in the delineations between DW-MRI and PET, especially for patient two.

The largest differences between DW-MRI and PET were found in small tumors, adjacent to lymphatic tissue. Both DW-MRI and FDG-PET are prone to false positives in these tissues, as it can show restricted diffusion behavior and increased FDG uptake. PET and DW-MRI visualize different biological processes and previous studies have investigated the relation between PET and DW-MRI in head-and-neck cancer [50, 72, 104–108]. However, these studies mainly looked at the relationship between SUV and ADC characteristics within the tumor and relating these to staging [107], histopathological parameters [104] or response prediction [72] and evaluation [72, 108]. Houweling et al. [50] investigated a radiotherapy application of PET and DW-EPI after deformable registration. They specifically looked into targets for dose painting within a previously defined GTV. The spatial resolution is a limitation of both techniques. The detection limit and point spread function in PET could account for some of the differences found in the smaller lesions (i.e. patients 1 and 2). In PET the spatial resolution is mainly limited by the detector width, where in DW-MRI the resolution is limited due to the usage of a single-shot readout sequence. Advances in MRI

sequence design (i.e., robust multi-shot DW-MRI sequences, faster imaging etc), could still provide additional gains in spatial resolution.

A limitation of the study is that no histopathology was available to compare the target volume with. In order to fully assess the value of DW-MRI for target volume delineation, it would be ideal to use pathology specimens in image validation studies [41, 42]. Unfortunately, this is very challenging for some anatomical sites such as the oro- and nasopharynx. As we know from previous studies, GTV on CT and MRI overestimates the tumor largely and shows large interobserver variation [60, 84, 85]. Therefore, we compared the target volume with an automatic segmentation on PET, as the PET volume approaches the true tumor volume closest and the automatic segmentation method is validated versus pathology. The acquisition of only 2 b-values, b=0 s/mm$^2$ and b=800 s/mm$^2$, in the diffusion sequence is another limitation. This could result in an overestimation of the ADC value in areas with a large blood plasma volume [109]. Finally, the number of patients in this study is limited.

The target volumes derived from DW-MRI were generally smaller than the GTV defined in current clinical practice (DW$_1$, DW$_2$, DW$_3$ vs GTV$_{RT}$). These smaller target volumes already lead to smaller treatment volumes. The addition of DW-SPLICE to the current practice of target volume delineation can help reduce variation among observers, since it allows for semi-automatic segmentations. The region identified by both DW-MRI and PET could be used as a first estimate for the tumor outline. Subsequently, using conventional T1- and T2-weighted MRI and CT, the GTV delineation can be refined. The combination of all these imaging modalities can further improve target volume delineation.

In conclusion, using an optimized DW-MRI sequence, target volumes were defined with good interobserver agreement and a good overlap with PET. Target volume delineation using undistorted DW-MRI is promising in head-and-neck radiotherapy.

## Acknowledgements

## Supplementary material

Supplementary table 4.1: Patient characteristics: tumor, lymph node and distant metastasis staging (TNM), tumor location and patient sex.

| Patient | T | N | M | Location | Sex |
| --- | --- | --- | --- | --- | --- |
| 1 | 2 | 0 | 0 | Tonsillar Region | M |
| 2 | 2 | 3 | 0 | Base of Tongue | M |
| 3 | 2 | 1 | 0 | Tonsillar Region | M |
| 4 | 2 | 0 | 0 | Tonsillar Region | F |
| 5 | 2 | 2b | 0 | Tonsillar Region | M |
| 6 | 1 | 2 | 0 | Nasopharynx | M |
| 7 | 3 | 2c | 0 | Hypopharynx | M |
| 8 | 1 | 0 | 0 | Base of Tongue | F |
| 9 | 1 | 0 | 0 | Nasopharynx | M |
| 10 | 3 | 2b | 0 | Tonsillar Region | M |
| 11 | 1 | 0 | 0 | Nasopharynx | M |
| 12 | 2 | 2b | 0 | Base of Tongue | M |
| 13 | 3 | 2b | 0 | Tonsillar Region | M |
| 14 | 4a | 2b | 0 | Oropharynx | M |
| 15 | 4a | 2b | 0 | Oropharynx | F |

Supplementary table 4.2: Comparison between PET and DWI. Volumes of the different modalities and delineators. Generalized conformity indices Dice similarity coefficients and contour distances between PET and DWI. GTV$_{RT}$ is the treatment volume retrieved from the treatment plan. Patient 11 was ultimately treated at a different institution, therefore, no volume was available.

| Patient # | Volumes (cm³) | | | | | CI$_{gen}$ | DSC vs PET | | | HD$_{mean}$ vs PET (mm) | | | HD$_{95}$ vs PET (mm) | | |
|---|---|---|---|---|---|---|---|---|---|---|---|---|---|---|---|
| | PET | DW$_1$ | DW$_2$ | DW$_3$ | GTV$_{RT}$ | DW$_{all}$ | DW$_1$ | DW$_2$ | DW$_3$ | DW$_1$ | DW$_2$ | DW$_3$ | DW$_1$ | DW$_2$ | DW$_3$ |
| 1 | 1.23 | 1.79 | 1.75 | 1.72 | 12.17 | 0.73 | 0.03 | 0.03 | 0.03 | 6.77 | 6.54 | 6.84 | 11.78 | 12.06 | 11.95 |
| 2 | 1.68 | 2.12 | 4.21 | 2.55 | 6.32 | 0.38 | 0.45 | 0.28 | 0.25 | 2.12 | 6.85 | 7.57 | 4.88 | 24.04 | 26.00 |
| 3 | 2.68 | 4.31 | 2.34 | 1.43 | 3.16 | 0.39 | 0.68 | 0.61 | 0.44 | 1.51 | 1.65 | 3.64 | 4.88 | 4.29 | 13.54 |
| 4 | 4.69 | 6.63 | 5.07 | 5.02 | 7.75 | 0.69 | 0.54 | 0.48 | 0.54 | 2.93 | 2.85 | 2.52 | 8.00 | 6.39 | 6.00 |
| 5 | 5.74 | 10.80 | 9.90 | 9.00 | 18.59 | 0.77 | 0.62 | 0.62 | 0.67 | 3.07 | 2.89 | 2.55 | 13.35 | 12.04 | 12.00 |
| 6 | 6.00 | 11.5 | 10.50 | 7.30 | 9.46 | 0.62 | 0.60 | 0.57 | 0.74 | 3.10 | 3.26 | 1.66 | 10.49 | 11.55 | 5.69 |
| 7 | 6.01 | 9.52 | 9.46 | 8.26 | 19.05 | 0.74 | 0.70 | 0.70 | 0.76 | 1.89 | 1.90 | 1.46 | 4.87 | 5.68 | 3.68 |
| 8 | 7.99 | 13.9 | 12.32 | 9.61 | 2.56 | 0.72 | 0.60 | 0.61 | 0.61 | 2.47 | 2.26 | 2.16 | 5.93 | 5.28 | 5.28 |
| 9 | 8.12 | 20.16 | 17.93 | 12.83 | 17.77 | 0.66 | 0.56 | 0.60 | 0.73 | 4.01 | 3.80 | 1.74 | 12.46 | 13.11 | 4.39 |
| 10 | 8.67 | 9.27 | 7.80 | 7.39 | 13.49 | 0.74 | 0.74 | 0.72 | 0.75 | 1.92 | 1.90 | 1.74 | 5.86 | 4.88 | 4.64 |
| 11 | 10.86 | 19.11 | 17.34 | 15.39 | - | 0.75 | 0.66 | 0.67 | 0.73 | 2.76 | 2.49 | 2.06 | 6.19 | 6.61 | 5.28 |
| 12 | 10.87 | 10.64 | 11.32 | 9.41 | 20.19 | 0.80 | 0.80 | 0.79 | 0.82 | 1.46 | 1.62 | 1.35 | 2.96 | 4.00 | 3.41 |
| 13 | 11.91 | 14.47 | 15.70 | 12.12 | 38.14 | 0.73 | 0.69 | 0.67 | 0.69 | 2.03 | 2.61 | 1.94 | 4.88 | 7.81 | 4.45 |
| 14 | 12.15 | 18.97 | 18.97 | 14.68 | 52.36 | 0.69 | 0.67 | 0.65 | 0.70 | 2.15 | 2.53 | 1.65 | 5.52 | 7.92 | 3.55 |
| 15 | 38.89 | 44.31 | 38.1 | 37.77 | 63.42 | 0.78 | 0.78 | 0.78 | 0.78 | 2.33 | 1.92 | 1.95 | 7.87 | 6.00 | 6.04 |
| Median | 7.99 | 10.80 | 10.50 | 9.00 | 15.63 | 0.73 | 0.66 | 0.62 | 0.70 | 2.33 | 2.53 | 1.95 | 5.93 | 6.61 | 5.28 |
| Minimum | 1.23 | 1.79 | 1.75 | 1.43 | 2.56 | 0.38 | 0.03 | 0.03 | 0.03 | 1.46 | 1.62 | 1.35 | 2.96 | 4.00 | 3.41 |
| Maximum | 38.89 | 44.31 | 38.10 | 37.77 | 63.42 | 0.80 | 0.80 | 0.79 | 0.82 | 6.77 | 6.85 | 7.57 | 13.35 | 24.04 | 26.00 |

# Chapter 5

# Synthetic fat suppression using water-fat separation in DW-MRI

Schakel, Tim
Hoogduin, Hans M.
Philippens, Marielle E.P.

## Abstract

Introduction: In head-and-neck oncology, diffusion weighted (DW) MRI is applied for detection and characterization of lesions and for tumor delineation for radiotherapy treatment planning. Single shot turbo spin echo methods, such as split acquisition of fast spin-echo signals for diffusion imaging (SPLICE), can be used to address magnetic field ($B_0$) homogeneity-related image distortions, found in the commonly used DW echo-planar imaging sequences. Additionally, regularly used spectrally selective fat suppression techniques also suffer from these $B_0$ inhomogeneities, whereas water fat separation techniques (Dixon) are more robust to them. In this work we aim to combine water fat separation with a DW-SPLICE sequence in order to improve fat suppression.

Materials & Methods: The DW-SPLICE sequence was modified to allow for shifting of the acquisition window between consecutive shots. The b = 0 s/mm$^2$ (b0) images were acquired 3 times with shifted acquisition windows to resolve water and fat. The water fat separation was performed using a hierarchical IDEAL algorithm. The results were applied to the b = 800 s/mm$^2$ images to achieve fat suppression. The method was demonstrated in volunteers and in a patient example.

Results: Using the modified DW-SPLICE sequence, water fat separation could successfully be performed, which resulted in good fat suppression in the diffusion weighted images in volunteers and patient example.

Conclusions: The DW-SPLICE sequence combined with water fat separation offers good fat suppression in the head-and-neck region and provides an alternative in applications with a high demand on robustness and geometrical accuracy.

## Introduction

The use of diffusion weighted MRI (DW-MRI) in the head and neck region has increased greatly over the last decade [22, 110]. In oncology, DW-MRI is applied for the detection and characterization of lesions, for tumor delineation for radiotherapy treatment planning and for treatment response monitoring [111, 112].

DW-MRI is typically acquired with fat suppression. The diffusion characteristics of fat are very similar to those of lesions and tumors; usually these have high signal intensity on diffusion weighted images and low apparent diffusion coefficient (ADC) values. Unsuppressed fat can obscure lesion conspicuity and makes images harder to interpret and process. Additionally, due to the chemical shift between water and fat, unsuppressed fat can shift in the images as a function of the pixel bandwidth. This effect is especially pronounced in single shot echo planar imaging (EPI), the most common technique to acquire diffusion data, due to its low pixel bandwidth in the phase encoding direction. Moreover, DW-EPI is very sensitive to geometrical distortions due to magnetic field inhomogeneities [61]. The head and neck area is characterized by multiple air-tissue transitions, resulting in large susceptibility differences. Consequently, for applications with high demands on geometrical accuracy, such as imaging for radiotherapy treatment planning, single shot turbo spin echo (TSE) methods are preferred in this region [94].

The combination of diffusion with TSE does require an approach to mitigate violations of the Carr-Purcell-Meiboom-Gill (CPMG) conditions. Motion during the diffusion weighting gradients creates a non-CPMG signal component at the beginning of the TSE train due to imbalanced phase accumulation around the refocusing pulse. As a result, spin echo and stimulated echo signal can interfere destructively. In SPLICE (split acquisition of fast spin-echo signals for diffusion imaging) an imbalanced readout gradient is used to separate two echo parities in time in order to prevent the interference. The acquisitions of the two echo parities are reconstructed separately, after which their magnitudes are combined [32].

While the use of TSE based sequences provides an alternative to DW-EPI to avoid geometrical distortions, fat suppression remains challenging in the head-and-neck region. Fat suppression in TSE sequences can be applied using various techniques which take advantage of differences in T1 relaxation times or resonance frequency between water and fat. The Short Time Inversion Recovery (STIR) technique utilizes the differences in T1 relaxation times. STIR typically results in good fat suppression, relatively independent of magnetic field homogeneity. However, it also results in an altered image contrast and reduced signal-to-noise ratio (SNR) or prolonged acquisition times. Fat suppression can

also be achieved using spectrally selective techniques such as SPIR or SPAIR. These techniques aim to selectively invert or saturate the signal at the fat frequency. However, these techniques are very sensitive to $B_0$ inhomogeneities and often result in incomplete fat suppression in areas with large field variations, especially at field strengths of 3.0 T and higher. Additionally, good $B_1$ homogeneity is critical for good fat suppression results, which can become challenging at the higher field strengths.

Water-fat separation techniques, commonly known as Dixon methods [38], have been successfully applied in difficult areas due to $B_0$ and $B_1$ inhomogeneity, such as the head and neck region [39, 40]. The chemical shift is encoded through acquisition of a series of images with different echo time shifts. In a postprocessing step, signal from water and fat can be separated and water-only (fat suppressed) and fat-only (water suppressed) images can be produced.

Combining DW-SPLICE with a water-fat separation technique appears to be attractive to obtain high quality images with robust fat suppression in the head-and-neck region. This combination has been explored before in DW-EPI [113, 114], mainly for olefinic fat suppression. There are reports on combining DW-TSE acquisitions with water fat separation [115, 116], though both used a different method for mitigation of the non-CPMG signal (Alsops parity selection method [35]). In this work we aim to combine water fat separation with a DW-SPLICE sequence in order to facilitate fat suppression.

## Theory

The DW-SPLICE sequence uses an imbalanced readout gradient to separate two echo parities in time. By elongating the readout gradient further, there is room to shift the two acquisition windows between different shots. This is schematically presented in figure 5.1. The prephasing gradient is adjusted accordingly. The E1 and E2 acquisitions are shifted between different shots, encoding the chemical shift in different images. The excitation and refocusing RF pulses are 90° out of phase.

The signal from a voxel at the different acquisition times $\tau$, can be described analogous to the iterative decomposition of water and fat with echo asymmetry and least squares estimation (IDEAL [54]) signal model:

$$S_{E1}(\tau) = \Big( \sum_{n=1}^{m} S_n e^{-i2\pi\Delta f_n \tau} \Big) e^{-i2\pi\Phi\tau} e^{-i2\pi\Psi} \tag{5.1}$$

with $m$ the number of chemical species, $\Delta f_n$ the chemical shift frequency offset with respect to water, $\Phi$ the spatially varying $B_0$ field offset and $\Psi$ the spatially varying, random frequency offset caused by bulk motion during diffusion weighting. By using data acquired at different acquisition times (and phase differences
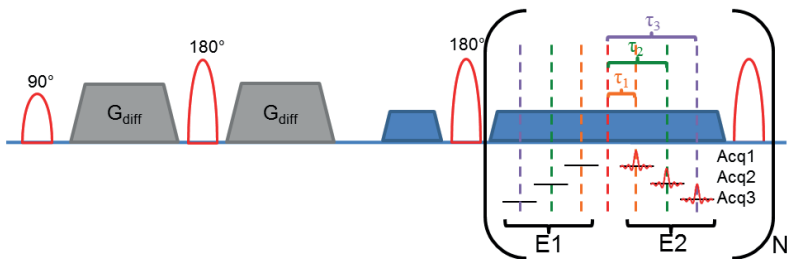
Figure 5.1: Sequence diagram of a DW-SPLICE acquisition, with additional shifted acquisitions. The increased echo spacing allows for the shifting of the acquisition window. The shifted E1 and E2 acquisitions have $\Delta$TEs, $\tau$1-3, with respect to the center of the echo spacing. The diffusion weighted images (b>0) are acquired with the diffusion sensitizing gradients along their respective axis and with the E1 and E2 readouts at position $\tau$1.

between the chemical species), different images for each species (water and fat in this case) can be reconstructed. Explicitly for water and fat, equation 5.1 becomes:

$$S_{E1}(\tau) = \left(S_w + S_f e^{-i2\pi\Delta f_f \tau}\right) e^{-i2\pi\Phi\tau} e^{-i2\pi\Psi} \tag{5.2}$$

With $S_w$ and $S_f$, the water and fat signals, and $\Delta f_f$ the water-fat chemical shift difference. The spatially varying, random, phase $\Psi$ adds complications for the water fat separation. Because it originates from motion, this phase varies between the different acquisitions. And in the presence of such random phases between acquisitions, the water and fat signals cannot be resolved reliably. The only acquisitions that do not suffer from these random phases, ie. the $\Psi$ term is 0, are the b = 0 s/mm$^2$ (b0) images, where the diffusion gradients are switched off. From additional b0 acquisitions with different acquisition times $\tau$, water and fat images can be reconstructed. The Dixon reconstruction is done using the hierarchical IDEAL algorithm [117]. This algorithm takes a multiresolution approach for improved optimization robustness and reduced chemical species ambiguity. The processing is done for each echo parity separately (E1 and E2), after which the results are combined. From the water and fat images, water and fat fractions can be calculated per pixel. These water-fraction maps are filtered using a 3x3 median filter. The diffusion weighted images (b>0) are reconstructed through a conventional SPLICE reconstruction. Synthetic fat suppression is achieved after multiplying a diffusion weighted image with its corresponding filtered water-fraction map. The data processing is schematically shown in figure 5.2.
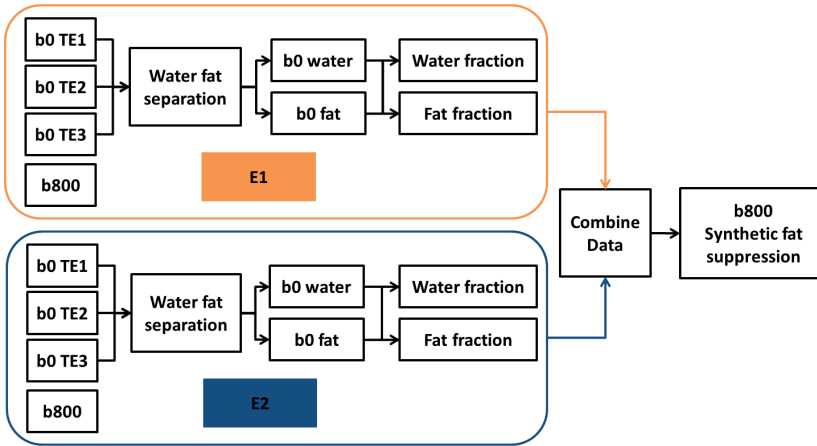
Figure 5.2: Schematic representation of the data processing for synthetic fat suppression. The water fat separation is processed for both echo parties separately on the b0 acquisitions. Subsequently, the data is combined and applied to the diffusion weighted, b = 800 s/mm$^2$ (b800) images.

## Materials & Methods

The sequence was implemented on a 3.0 T system (Ingenia, Philips Healthcare, Best, The Netherlands). Data was acquired, after approval of the IRB, in 5 healthy volunteers using a 16 channel head and neck coil. To demonstrate the clinical application of the sequence, it was added to the clinical scanning protocol of a patient. This head and neck cancer patient was scheduled for radiotherapy and received the MRI exam as preparation for the treatment. Therefore, this patient was scanned in an immobilization mask in treatment position with 2 channel flexible surface coils (Flex-M) [73].

Image acquisition parameters DW-SPLICE: field of view 200 x 280 x 120 mm$^3$ (RLxAPxFH); voxelsize 1.8 x 1.8 mm$^2$; slice thickness 4 mm; TE/TR = 95/19356 ms, echo spacing = 8.9 ms, echo train length = 56, SENSE = 2, b-values = 0, 200, 800 s/mm$^2$ (with 1, 2 and 5 averages respectively) in 3 directions with a gradient overplus (simultaneous application of diffusion encoding gradients in different directions) scheme. The b0 images were acquired 3 times with the acquisition window shifted by $\Delta$TE ($\tau$1-3 = 0.9 / 1.6 / 2.3 ms) for water-fat separation. Total imaging time: 7m44s. For the patient scan, the acquired voxel size was increased to 2.2 x 2.2 mm$^2$ to decrease the total imaging time to 6m41s.

The acquired data was taken offline and processed in Matlab using the Recon-Frame toolbox (Gyrotools, Zurich, Switzerland). A conventional reconstruction was performed on the odd and even echo parity separately, resulting in com-
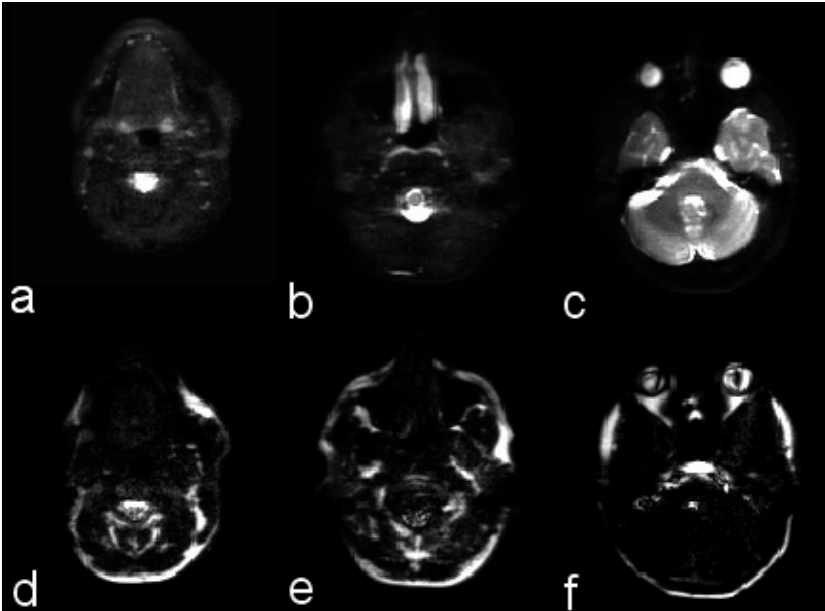
Figure 5.3: Water-fat separation results of the b=0 acquisition of the diffusion series in a volunteer (head and neck region). Three different slices from the acquired field of view are shown from left to right. The top row are the water images, the bottom row shows the fat images.

plex images. The water-fat separation was done using the hierarchical IDEAL algorithm [117] from the ISMRM fat-water toolbox.

Additional measurements using the proposed method were performed using an ice-cooled QIBA DWI phantom (High Precision Devices, USA). The mean value of a region of interest (ROI) in the center tube of the phantom is compared with the reference value provided with the phantom.

## Results

The water-fat separation results in the head and neck region of a volunteer are shown in figure 5.3. It shows the reconstructed, water and fat images derived from the b0 slices of several different levels over the acquired field of view. The T2 contrast of the DW-SPLICE sequence is clearly visible. Figure 5.4 shows the corresponding water-fraction map. The water fractions are high in areas such as the brain, muscles and glandular structures and low in the subcutaneous fat and deeper fatty tissue between the neck muscles.
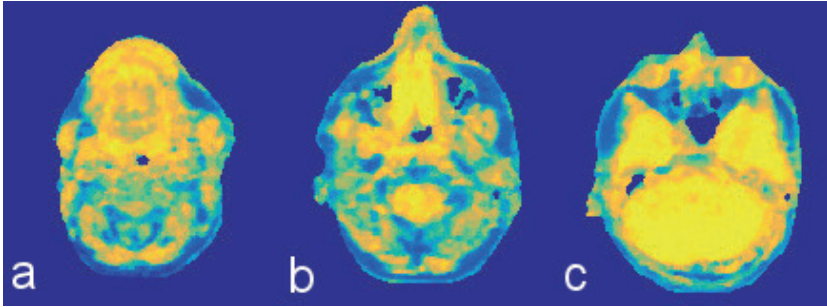
Figure 5.4: Calculated water-fraction maps of the same dataset as figure 5.3.

An example of fat suppression for the diffusion weighted images is given is figure 5.5. It shows a b800 image without fat suppression, with the proposed method for fat suppression and with fat suppression using a SPIR pulse respectively. It illustrates how fat is suppressed with the proposed method and how signals from tissues that show diffusion restriction, such as brain, spinal cord, lymph nodes and glands at the base of the tongue, are preserved. Note that using a conventional SPIR fat suppression pulse, several areas of unsuppressed fat remain.

Figure 5.6 shows the corresponding ADC map of the DW-SPLICE Dixon acquisition. An additional measurement was performed using a QIBA diffusion phantom. The ADC value in an ROI in the center tube was $1.133 \pm 0.019$ x $10^{-3}$ mm$^2$/s (average $\pm$ standard deviation), compared to the provided reference value of $1.109 \pm 0.013$ x $10^{-3}$ mm2/s.

The results obtained from the head and neck cancer patient are presented in figure 5.6. The figure shows a slice with the primary tumor and positive lymph nodes on the same level. The primary tumor is located at the base of tongue (yellow arrow). Positive lymph nodes are indicated with red arrows. Note how these lymph nodes are surrounded by fat tissue and are difficult to identify without or with inadequate fat suppression (i.e. in a case where spectral fat suppression techniques have failed due to field inhomogeneities). It demonstrates how pathology is better visualized using the proposed method.

## Discussion

The head and neck region is challenging for diffusion imaging. The large magnetic field variations cause geometrical distortions when conventional single shot DW-EPI is used. Applications with a high demand on geometrical accuracy have found alternatives in diffusion weighted TSE sequences [63, 94]. However, robust fat suppression remains an issue, as it important for tumor and lymph
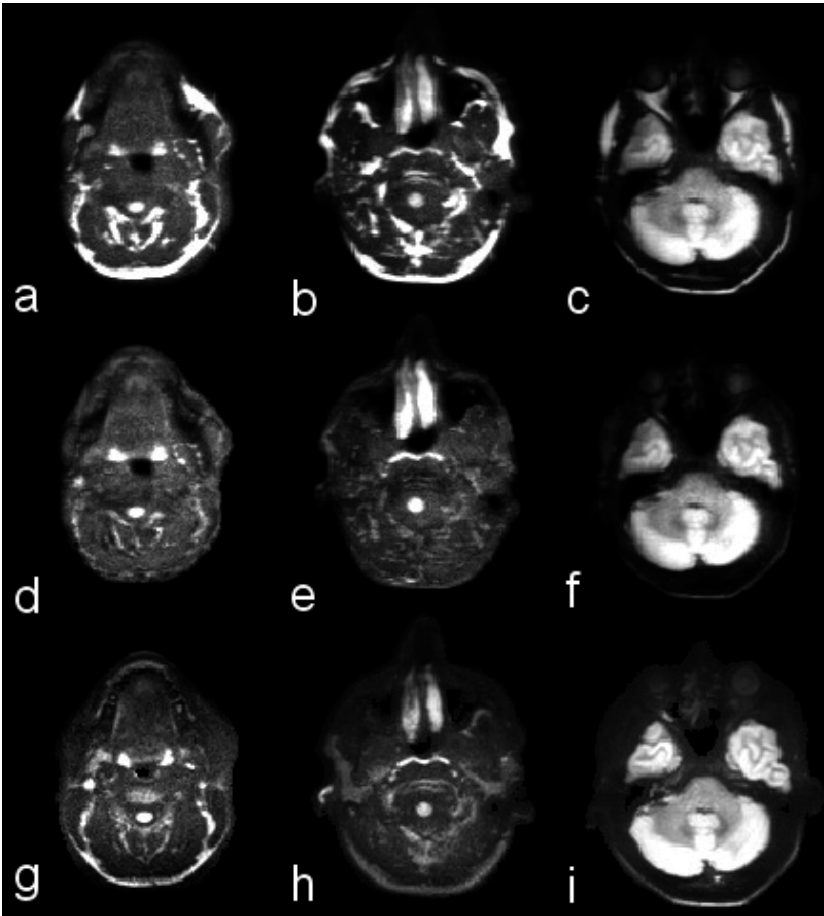
Figure 5.5: DW-MRI, b800 acquisitions. Top row: no fat suppression. Middle row: synthetic fat suppression using the water-fat separation results from the b0 acquisitions. Bottom row: SPIR fat suppression.
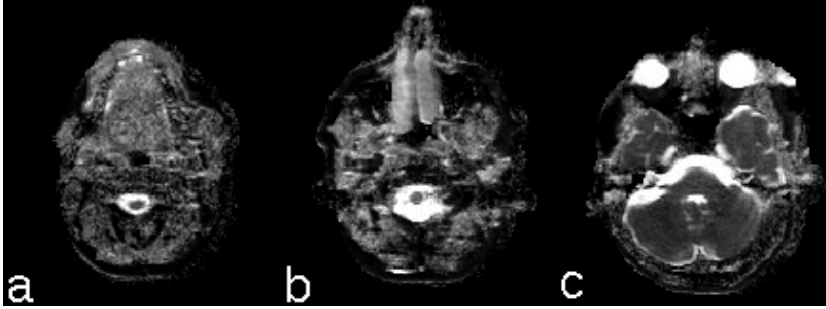
Figure 5.6: ADC map calculated from the DW-SPLICE dixon acquisition.

node conspicuity. The DW-SPLICE sequence with water-fat separation can provide fat suppressed, diffusion weighted images in this challenging region. Using the results from water-fat separation of the b0 images of the diffusion series, the fat in the diffusion weighted images can be suppressed. The proposed method requires limited additional data acquisition, as only the b0 images are acquired multiple times with the shifted readouts. This is particularly advantageous since diffusion weighted TSE sequences are already very time demanding.

The method was demonstrated in volunteers and additionally in a patient example to show how the method can aid in the improved detection of pathology. Due to time constraints, the direct comparison to spectrally selective techniques such as SPIR, which is commonly applied for diffusion weighted sequences, could not be made. However, it is known that these techniques struggle to achieve good fat suppression in the head and neck area.

The ADC values, as measured in a specialized phantom, of the proposed method correspond well with the reference values. Nevertheless, the lack of fat suppression in the diffusion weighted images can introduce a bias in the ADC calculations in mixed voxels as fat tissue has highly restricted water mobility and thus a low ADC [118, 119]. Even correction for water and fat fraction will not result in accurate ADC values, as the signal decay is not mono-exponential due to partial volume averaging in voxels with a mixed contribution of fat and water. For a reliable bi-exponential fit, more b-values are required. We limited the number of b-values to three, as accurate quantification of ADC was not the main purpose of the diffusion imaging

The main challenge of combining water-fat separation with diffusion imaging is the random phase accumulation due to motion during the diffusion weighting gradients. This phase contribution varies per shot and corrupts the phase dependent water fat separation in a multi-acquisition method. Without performing additional measurements, like navigators, to estimate this diffusion phase,
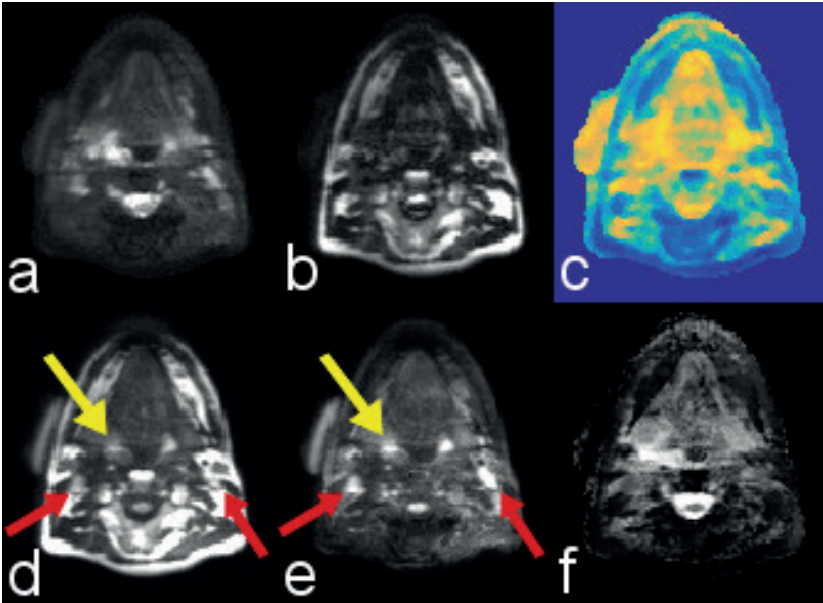
Figure 5.7: Results obtained from a patient with a head and neck tumor. Top row, from left to right: b0 water reconstruction, b0 fat reconstruction, water-fraction map. Bottom row, from left to right: b800 without fat suppression, b800 with synthetic fat suppression using the waterfraction map, ADC map.

the water-fat separation in the diffusion weighted images cannot be performed accurately. In the b0 acquisitions the large diffusion weighting gradients are switched off, thus these do not suffer from the motion dependent phase accumulation. Water-fat separation using solely the b0 acquisitions is also the main limitation of the presented method, as it is not performed on the diffusion weighted images directly. Similarly to any water-fat separation sequence, the chemical shift difference needs to be encoded, which is done through additional echo acquisitions with shifted readouts, lengthening the total acquisition time. In addition, to facilitate the shifting of the readout lengthening of the echo spacing is inevitable, which leads to longer TSE shots. This increases the amount of blurring that occurs, as can be noted in figure 5.5 where the DW-SPLICE Dixon acquisition (middle) shows more blurring than the normal DW-SPLICE acquisition (bottom).

The current study only investigated DW-SPLICE sequences, however, the approach is also applicable to alternative diffusion weighted TSE sequences such as Alsops elimination method [35]. A multi-echo, water-fat separated, diffusion weighted Alsop sequence was recently proposed by Wang et al. [116] for spine imaging. Due to the complications of combining Dixon and diffusion techniques,

there is little literature available on this subject. Recently, Burakiewicz et al. have reported on combining Dixon with conventional DW-EPI for fat suppression in the pelvis [113]. They acquire additional navigators to determine and correct the diffusion phase. In another paper, a new reconstruction method to suppress olefinic fat in skeletal muscle applications is proposed [120].

The shifted acquisitions are only performed for the b0 images. Further improvements to the method could also enable water fat separation of the diffusion weighted images. In order to do this, the pseudo random diffusion phase needs to be estimated or the water-fat separation should not rely on the phase, but on the magnitudes of the signal [114,120]. However, the required additional acquisitions would lead to a substantial increase in scan time, a threefold increase when applying the current acquisition strategy. For applications that assume isotropic diffusion, this increase could be mitigated by acquiring each of the three orthogonal diffusion directions with a shifted readout or by acquiring only one diffusion direction. This would however, require additional sequence modifications.

We have combined a Dixon water-fat separation method with a single shot, diffusion weighted TSE sequence, DW-SPLICE. The method was evaluated in vivo and showed promising results in suppressing fat in an otherwise very challenging region, with only limited additional data acquisition and scan time. The method could be an alternative in applications with a high demand on robustness and geometrical accuracy such as imaging for radiotherapy treatment planning.

# Chapter 6

# Validation of DW-MRI in laryngeal cancer: initial results

Schakel, Tim
Ligtenberg, Hans
Ruiter, Lilian N.
Peltenburg, Boris
Hoogduin, Hans M.
Terhaard, Chris H.J.
Raaijmakers, Niels P.J.
Philippens, Marielle E.P.

## Abstract

Introduction: Diffusion weighted (DW) MRI is a promising technique for tumor delineation in radiotherapy treatment planning. The aim of this study is to validate DW-MRI using pathology in laryngeal cancer. The results from the first patient are presented.

Materials & Methods: MR imaging was performed prior to total laryngectomy. The surgical specimen was processed and matched back to in vivo imaging. Ex vivo MRI of the specimen was acquired. Target volume delineation was performed on hematoxylin-and-eosin stained sections by a pathologist (tumor$_{HE}$) and on DW-MRI (GTV$_{DW}$).

Results: The volumes of tumor$_{HE}$ and GTV$_{DW}$ were 12.3 and 11.7 cm$^3$ respectively. The dice similarity coefficent was 0.82 between tumor$_{HE}$ and GTV$_{DW}$. The sensitivity and positive predictive value of DW-MRI were 0.80 and 0.84 respectively. Similar results were found for the ex vivo DW-MRI.

Conclusions: For this case, DW-MRI showed excellent agreement with pathology delineations. We are awaiting the results from additional patients enrolling in this study before any definitive conclusions can be drawn.

# Introduction

Target volume delineation is a crucial step in the successful delivery of radiation treatments [82]. Incorrect delineation of the target can lead to undertreatment of diseased areas with the potential consequence of reduced local control. On the other hand, overestimation of the target volume can lead to increased normal tissue damage, with possible normal tissue complications as effect [6, 7, 83]. For head and neck cancer, the tumor is typically in close proximity to these organs at risk.

In modern radiotherapy, the gross tumor volume (GTV) is delineated on various imaging modalities. Computed tomography (CT) is traditionally used for tumor delineation. However, positron emission tomography (PET) and magnetic resonance imaging (MRI) are increasingly added to provide additional information. Despite the additional information available for GTV delineation, the correct interpretation of the imaging modalities remains challenging. This is demonstrated by variations in delineations between the different modalities as well as between different observers [59, 60, 84]. Imaging validation studies using surgical specimens and (histo)pathology can evaluate the accuracy of the different imaging modalities and provide insight in the correct interpretation of them [42, 85].

Recently, diffusion weighted MRI (DW-MRI) has gained interest for tumor delineation. DW-MRI provides information on the tissue micro anatomy and reflects the local mobility of water molecules [23]. Consequently, it is sensitive to features such as tissue organization and cellular density, characteristics that also distinguish tumor from healthy tissue. The conventional acquisition method of DW-MRI is not very well suited for use in target volume delineation due to its poor geometrical accuracy especially near air cavities [61]. However, by using a different acquisition scheme, geometrically accurate diffusion weighted images can be acquired in a radiotherapy simulation setup [94].

The aim of this study is to validate tumor delineation using DW-MRI using histopathology in laryngeal cancer. We compare target volume delineations on DW-MRI with corresponding delineations on histopathology using hematoxylin and eosin stained slices. In this chapter a case study is presented, awaiting further patient inclusion.

# Materials & Methods

The study was approved by our ethics review board. The case presented here is a 66 year old male with a T4aN0M0 laryngeal tumor. This patient underwent total laryngectomy (TLE) as primary treatment. Prior to surgery this patient underwent an MRI exam. Time interval between MRI and TLE was 2 days.

## Imaging

All imaging was performed in radiotherapy treatment position using a personalized head support and 5-point head and shoulder immobilization mask [73].

MR imaging was performed on a 3.0 T Ingenia system (Philips Healthcare, The Netherlands) using 2-element flexible surface coils. Diffusion weighted images were acquired using the DW-SPLICE sequence [32], which was prototyped and loaded on the system. Diffusion weighting was done in three orthogonal directions to create an isotropically diffusion weighted image. ADC maps were calculated directly on the MR system.

Furthermore, ex vivo MR was performed on the surgical specimen following fixation. Diffusion and T2 weighted images were acquired. Additional sequence parameters are given in supplementary table 1.

## Surgical specimen processing

Following TLE, the surgical specimen was processed according to Caldas-Magalhaes et al. and adjusted as described by Ligtenberg et al. [41, 85]. The specimen was fixated in 10% formaldehyde. After fixation, a CT scan and MRI scans of the specimen were acquired. The specimen is then enclosed in an agarose block and sliced into approximately 3 mm thick slices. From these slice, 4 µm sections are obtained for staining with hematoxylin-and-eosin (HE). After digitization of the HE stained sections, a head and neck pathologist digitally delineated the tumor tissue (tumor$_{HE}$). Both the HE sections and thick slices were digitized and reconstructed into a 3D volume.

## Image registration

A rigid registration was performed between the in vivo CT and MRI. The in vivo CT and MR were also rigidly registered to their corresponding ex vivo CT and MR of the specimen as an intermediate step. The reconstructed 3D specimen was registered to the ex vivo CT of the specimen. The HE sections were matched to their corresponding thick slice by a point based rigid registration with scaling after manual identification of landmarks on both slices. A detailed overview and flowchart of the registrations is given in Caldas-Magalhaes et al [41].

## GTV delineation

DW-MRI was used to determine the target volume. First, the hyperintense region on the b = 800 s/mm$^2$ (b800) was identified with semi-automatic segmentation. A seed point is placed centrally in the tumor on the b800 image and a region is segmented using a signal intensity threshold of 50% of the maximum

signal intensity. Subsequently, the generated contour was propagated to the corresponding ADC map. Using the ADC map, regions of high ADC, typically at the edge of the tumors, were excluded manually. This was done on both the in vivo ($GTV_{DW}$) and ex vivo DW-MRI ($GTV_{DWex}$).

## Data analysis

All delineations were resampled on the grid of the MR for further analysis. From the resampled delineations binary masks were generated to determine the delineated volumes.

As overlap measure the Dice similarity coefficient (DSC) is calculated. Furthermore, the sensitivity and positive predictive value (PPV) of the delineations were determined. The sensitivity is defined as the part of the $tumor_{HE}$ that is covered by the delineated GTV. Ideally, the sensitivity is 1, meaning no tumor was missed in the GTV delineation. The PPV is defined as the part of the GTV that is covering the $tumor_{HE}$. If this value is 1, all of the defined GTV contains tumor, so no normal tissue was delineated. A good GTV delineation is characterized by both a high sensitivity and PPV.

The Hausdorff distances (HD) between the GTV and $tumor_{HE}$ were calculated. The mean Hausdorff distance ($HD_{mean}$) and the $95^{th}$ percentile distance ($HD_{95}$) are reported. Similar to Ligtenberg et al., the distances are measured from $HD_{mean}$ to the intersection volume between $tumor_{HE}$ and GTV. Any discrepancy between these two volumes ($tumor_{HE}$ and intersection $tumor_{HE}$-GTV) will indicate missed tumor in the GTV delineation.

## Results

All processed pathology slices for this patient are presented in figure 6.1. Both the pathology delineation ($tumor_{HE}$, green) and the DW-MRI delineation ($GTV_{DW}$, blue) are shown. Note that the DW-MRI delineation extends one slice caudally of the last HE slice containing tumor (figure 6.1, top left). Additionally, cartilage invasion could be observed in the HE sections. In figure 6.2 three consecutive slices, through the middle of the tumor, of DW-MRI prior to TLE are shown with corresponding ADC maps. The same delineations are depicted as in figure 6.1. The ex vivo DW-MRI at approximately the same level as in figure 6.2 is displayed in figure 6.3.

## Volumes

The $tumor_{HE}$ volume was 12.3 $cm^3$. $GTV_{DW}$ had a volume of 11.7 $cm^3$, the intersecting region of these two delineations was 9.8 $cm^3$. For $GTV_{DWex}$ this was 11.7 and 9.7 $cm^3$ respectively.
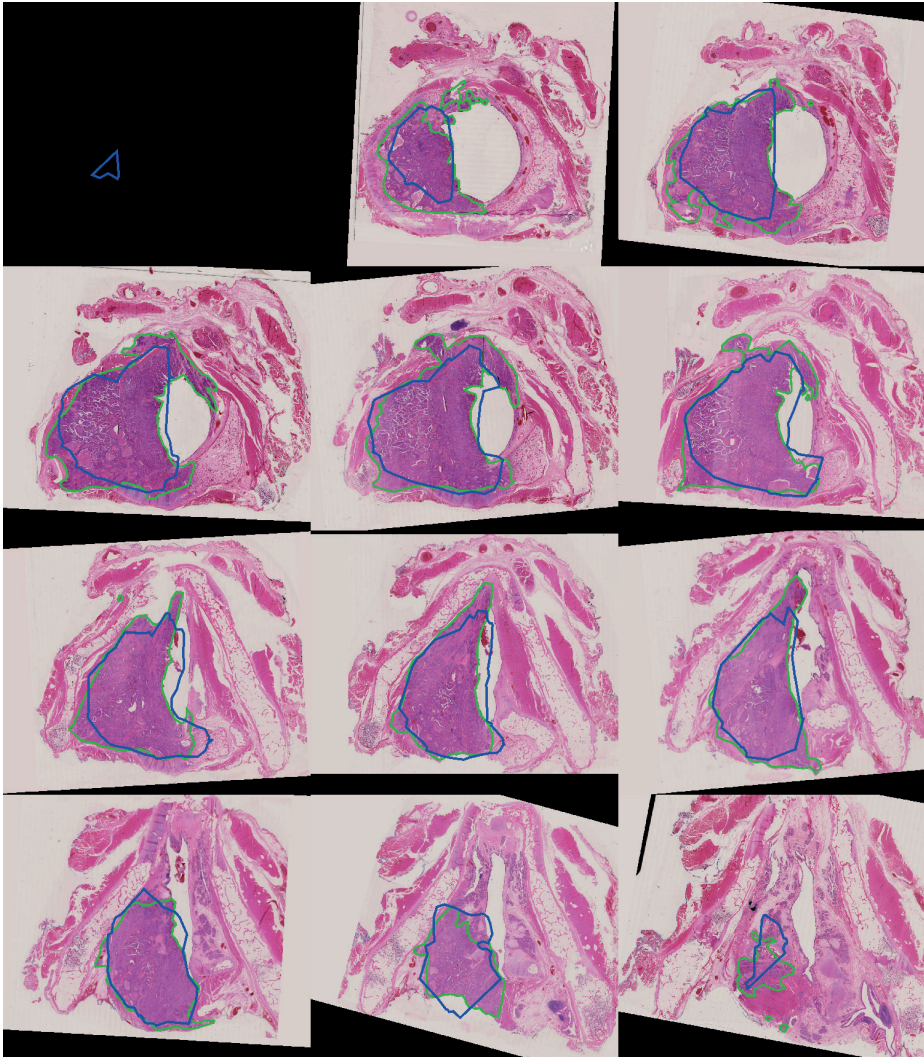
Figure 6.1: HE stained sections of the pathology specimen, sequentially from caudal to cranial. The delineation by the pathologist is shown in green. The GTV delineation on the registered in vivo DW-MRI is shown in blue.

## Overlap measures

Compared with the gold standard tumor$_{HE}$, GTV$_{DW}$ had a DSC of 0.82, sensitivity of 0.80 and PPV of 0.84. The comparison of the tumor$_{HE}$ with ex vivo DW-MRI showed similar results, with a DSC of 0.81, sensitivity 0.79 and PPV 0.83.

Figure 6.2: In vivo DW-MRI, zoom of the larynx. Top row: DW-MRI, b800, three transverse slices; bottom row: corresponding ADC maps. In blue the GTV as determined on DW-MRI is shown ($GTV_{DW}$). The delineation by the pathologist is shown in green ($tumor_{HE}$).

## Distance measures

The mean distance, $HD_{mean}$, between $tumor_{HE}$ and the intersection $tumor_{HE}$-$GTV_{DW}$ was 1.0 mm with a $HD_{95}$ of 3.6 mm. For the comparison between $tumor_{HE}$ and $GTV_{DWex}$, $HD_{mean}$ was 1.0 mm and $HD_{95}$ was 3.2 mm.

## Discussion

For this case, we compared a target volume derived from DW-MRI with matched gold standard pathology of the surgical specimen. The GTV determined on DW-MRI showed very good agreement with the $tumor_{HE}$. The volume difference was only 0.6 cm$^3$. Additionally, there was large spatial overlap between the two, as indicated by a DSC of 0.82 and illustrated in figure 1. Ex vivo DW-MRI of the surgical specimen was very similar to the in vivo DW-MRI.

However, the $GTV_{DW}$ did not include all tumor tissue, the sensitivity was 0.80. Registration inaccuracy and tissue deformation in the pathology procedure can account for some of this mismatch but not all. Hence, part of the microscopic tumor tissue visible on the HE sections is not visible on the DW-MRI. By definition the tumor as delineated in the in vivo imaging is the GTV. This mismatch can be addressed by adding a margin to the GTV in order to cover
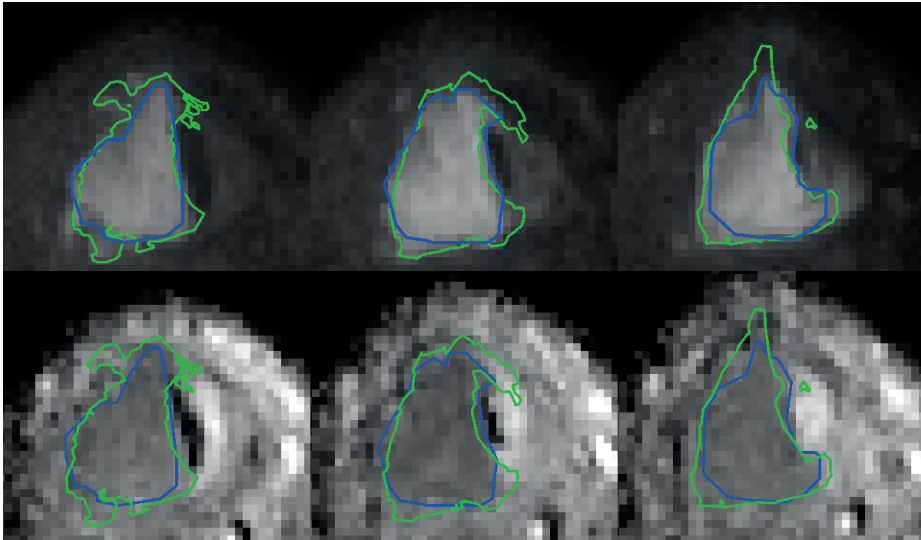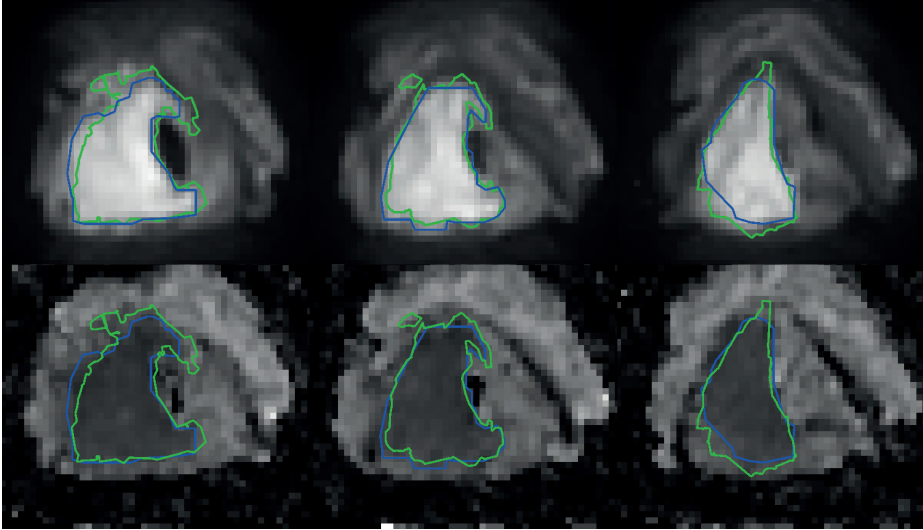
Figure 6.3: Ex vivo DW-MRI of the larynx specimen. Top row: DW-MRI, b800, three transverse slicess; bottom row: corresponding ADC maps. In blue the GTV as determined on ex vivo DW-MRI is shown ($GTV_{DWex}$). The delineation by the pathologist is shown in green ($tumor_{HE}$).

all microscopic tumor. Previously, we proposed a margin of 6.1 mm for MRI to include all microscopic tumor [85]. When this margin is applied to this case, the resulting CTV will cover 99.95% of the tumor, with a total volume of 38.7 cm$^3$.

The PPV of the $GTV_{DW}$ was 0.84, indicating that there was little overestimation. Other modalities, CT, FDG-PET and MRI, showed more overestimation in a previous study resulting in PPV of 0.50, 0.61 and 0.59 respectively [85].

Cartilage invasion is very relevant for tumor staging, but it is also known to be difficult to distinguish on imaging. The HE sections showed cartilage invasion, however, this was not detected on DW-MRI.

Although, we showed previously that MRI, FDG-PET and CT showed better sensitivity of the tumor, they also largely overestimated the tumor volume, leading to relatively large CTVs. DW-MRI results in a more concise GTV, resulting in a relatively small CTV after expanding the delineated volume with a CTV margin to account for the missed tumor volume.

This case represents the first result of an ongoing imaging validation study. Patients in this study have a complete MRI exam with T1 (with and without contrast) and T2 weighted imaging. Additionally, they also have an FDG-PET/CT

scan. Further analysis on the performance of different individual imaging contrasts and modalities as well as the combination of them will be performed [121].

From this single case, it can be noted that DW-MRI shows good correspondence with gold standard pathology and that, delineation on DW-MRI alone, gives a good approximation of the bulk of the tumor. It seems to be less prone to overestimation than T1 and T2 weighted MRI and CT.

## Supplementary material

Supplementary table 6.1: Sequence parameters used for the patient and specimen imaging.

| Scan | DW-SPLICE (in vivo) | DW-SPLICE (ex vivo) |
|---|---|---|
| FOV (RL x AP x FH) [mm$^3$] | 200 x 200 x 120 | 120 x 90 x 120 |
| Acquired voxel size [mm$^2$] | 1.8 x 1.8 | 1.8 x 1.8 |
| Slice thickness [mm] | 4 | 4 |
| TE [ms] | 74 | 73 |
| TR [ms] | 16331 | 14351 |
| SENSE acceleration factor | 2 | 2 |
| Echo train length (dummies) | 55 (5) | 25 (5) |
| Bandwidth [Hz] | 814.6 | 790.6 |
| b-values [s/mm$^2$] | 0, 200, 800 | 0, 200, 800 |
| Averages | 2, 2, 5 | 2, 2, 7 |
| Total acquisition time | 6m15s | 6m56s |

# Chapter 7

# Summary and discussion

In this thesis the use of diffusion weighted MRI for target volume delineation in head and neck radiotherapy was studied. Accurate target volume delineations are essential for the accurate delivery of radiotherapy. DW-MRI reflects the tissue micro anatomy and is dependent on tissue organization and cell density amongst others. These tissue characteristics are distinctly different between tumors and healthy tissue, making DW-MRI an interesting technique for target volume delineation. However, while DW-MRI is an established technique in radiology, mainly in neurological applications [122, 123], its use in radiotherapy is still limited. In order to use an imaging modality for target volume delineation in radiotherapy treatment planning it must have high geometric accuracy. A distorted anatomy will lead to erroneous delineations and could consequently, compromise the treatment of the patient.

## 7.1    Acquisition of diffusion weighted MRI

### Echo planar imaging

DW-MRI is commonly acquired using EPI, primarily for its high speed and SNR efficiency. However, the technique is prone to geometric distortions [25, 26, 53]. The image distortions in DW-EPI are a combination of the underlying patient anatomy and sequence parameters. The patient to be imaged will perturb the static magnetic field, causing magnetic field inhomogeneities. The exact location and extent of these magnetic field inhomogeneities are dependent on the specific anatomy to be imaged, and the magnetic susceptibility variation within the structure. Anatomical sites which are largely homogeneous, such as brain, will show small variations in the magnetic field, whereas more heterogeneous sites,

such as head and neck will show larger variations. The head and neck region shows a large heterogeneity in magnetic susceptibilities, mainly near air-tissue transitions, giving rise to complex magnetic field inhomogeneities. Moreover, when imaging head and neck cancer patients, the majority of their tumors are squamous cell carcinomas which originate from the mucosal layers of the upper aerodigestive tract. Therefore, most of the head and neck tumors are adjacent to these air-tissue transitions. The DW-EPI sequence parameters that influence the geometric accuracy are the ones that dictate the bandwidth in the phase encoding direction, the amount of phase encoding lines and the time between them. N.b. in EPI the image distortions are primarily in the phase encoding direction, as the frequency encoding direction has a much larger bandwidth. The low bandwidth in the phase encoding direction also causes large fat shifts, up to multiple centimeters, which can severely degrade image quality.

In chapter 2, the geometric accuracy of single shot DW-EPI is evaluated for head and neck cancer. This was done by retrospective analysis of magnetic field maps from a patient dataset. The magnetic field maps were evaluated in the most relevant region for target volume delineation, the GTV. It was found that severe image distortions are present in this region, with maximum pixel shifts up to several centimeters, rendering single shot DW-EPI unsuitable for usage in target volume delineation in its current form.

As the image distortions due to off-resonance effects induced displacements can be calculated retrospectively using a magnetic field map, an attempt can be made to use this information for retrospective correction. Various methods have been proposed to retrospectively correct EPI images [53, 55, 124]. For the first method, an additionally acquired magnetic field map is required. Using the phase encoding pixel bandwidth, a pixel shift map can be calculated, which describes the displacement of each pixel in the phase encoding direction. Using this pixel shift map, a distorted EPI image can be unwarped. This was also attempted in chapter 2 and while the undistorted locations of the pixels could be recovered, their signal intensities were smeared out over the path of the distortion. This occurs when multiple pixels from different locations are piled up into the same distorted pixel. Furthermore, this type of retrospective correction relies on additional information from a separate scan. Motion between the field map acquisition and the actual DW-EPI acquisition can cause the distortion correction to produce inaccurate results.Another method is the reversed gradient method. Here, two EPI images with opposing phase encode directions are acquired. The correct position of each pixel is exactly in between the two images acquired with opposite polarities, which is estimated using non-rigid image registration. The advantage of this method is that also eddy currents can be corrected for. However, also this methods requires the acquisition of a second image [125].

Generally, there are two approaches to reduce the distortions in DW-EPI during acquisition. The first is to increase the phase encoding bandwidth, this can be achieved by reducing the number of acquired lines in the phase encoding direction. This easiest way to do this is sacrificing spatial resolution; although generally this is undesirable due to the already limited spatial resolution in single shot EPI. However, when using parallel imaging, the image can be reconstructed in the full resolution while acquiring less lines. This speeds up the acquisition and increases the phase encoding bandwidth. This does come at the cost of increased noise in the images. Additionally, the amount of acceleration is limited by the amount (and configuration) of receiver coils in the imaging setup. In the current coil setup, where patients are scanned in their immobilization mask, the amount of parallel imaging is already maximized. The development of coils with a large number of channels [126],which are compatible with the immobilization mask, can further improve image quality. Not only to allow for higher parallel imaging factors [127], and consequently reduced image distortions in DW-EPI, but also to improve SNR.

The second approach is to decrease the underlying magnetic field inhomogeneity. This can be done through shimming. In active shimming, specialized shimming gradient coils are used to generate a corrective magnetic field to counteract the subject induced magnetic field inhomogeneity [128, 129]. Modern 3.0 T MR systems have shimming gradients that can produce second order corrective field, while 1.5 T MR systems can typically only produce first order fields. In order to calculate the appropriate corrective shim field, some estimate of the magnetic field inhomogeneity is required. Once this field inhomogeneity is known, an optimization algorithm can be used to derive the shim fields [130]. This can be done for the entire field of view, or optimized on a specific region of the anatomy [131]. In the latter case, the magnetic field inhomogeneity of areas not included in the shim optimization algorithm could worsen. Several methods have been proposed to further improve optimization algorithms, using additional constraints in the algorithm [132, 133] or by utilizing information on the location of water and fat in the image [134, 135]. First, shimming on water only will improve the shim by reducing the off-resonance effect of fat. Second, information of water and fat resonance frequencies can be used to optimize shims for spectral fat suppression, since the magnetic field homogeneity also influences the effectiveness of spectral fat suppression methods. However, due to its proximity to the air tissue interface, the magnetic field inhomogeneities around a head and neck tumor are generally more complex than can be corrected for using second order shim gradients. An alternative approach would be to use passive shimming, e.g. by placing a susceptibility-matched material around the patient. While this alleviates some of the magnetic field inhomogeneities around the complex chin-neck-shoulder shapes, the issues with the internal air-tissue transitions remain.

## Turbo spin echo

Alternatively, diffusion weighted MRI can also be acquired using a single shot turbo spin echo (TSE) readout [28–30,32,35]. In single shot TSE, RF refocusing pulses are inserted between every readout line. These RF refocusing pulses will reverse phase accrual from off-resonances (such as magnetic field inhomogeneities or eddy currents), removing the phase encoding errors that are observer in EPI sequences. The geometric accuracy of DW-TSE sequences is comparable to that of standard anatomical sequences.

The DW-SPLICE sequence was implemented as alternative for DW-EPI in chapter 3. Using the DW-SPLICE sequence diffusion weighted images with excellent geometric accuracy and good overall image quality can be acquired. The geometric distortions that DW-EPI produces in the phase encoding direction are not present in TSE based sequences such as DW-SPLICE. Additionally, the bandwidth in the readout direction was large enough such that any distortions in this direction, i.e. due to off-resonance effects, are on the sub millimeter level. This means these images are suitable for target volume delineation and use in radiotherapy treatment planning. An example is also given in figure 7.1, this is the same patient as in the introduction of this thesis (figure 1.2 and 1.3).

The main disadvantage of DW-SPLICE, and TSE methods in general, is the increased acquisition time. TSE methods are inherently slower due to the inclusion of the RF refocusing pulses. In the results presented in chapter 3, it takes 16.4 s to acquire a single volume of diffusion data with DW-SPLICE, while this is 3.3 s with DW-EPI. This limits the amount of data (i.e. b-values or signal averages) that can be acquired within a clinically acceptable time. In practice this means less b-values will be acquired, the signal averages are required in order to have the diffusion weighted images have sufficient SNR. The reduction of the number of b-values limits the diffusion quantification possibilities. Simple models, such as a mono exponential fit to estimate the ADC value can be performed using 2 or 3 b-values. However, more sophisticated methods such as the bi exponential intra-voxel incoherent motion model require more b-values [109]. As DW-SPLICE is a single shot method, it has a limited spatial resolution. Increasing the resolution would increase the number of lines acquired per shot and increase the shot length. This would mean a loss of echo signal along the shot due to the T2 relaxation of the transverse magnetization. This decrease in signal over the echoes also acts as a k-space filter, resulting in blurring in the reconstructed images that increases with shot length.

In order to further improve the DW-SPLICE image and decrease the amount of blurring, multi shot methods are an option. Since less lines are acquired per shot, the shot length decreases and with it the amount of blurring. This could also facilitate the acquisition of images at a higher spatial resolution. However,
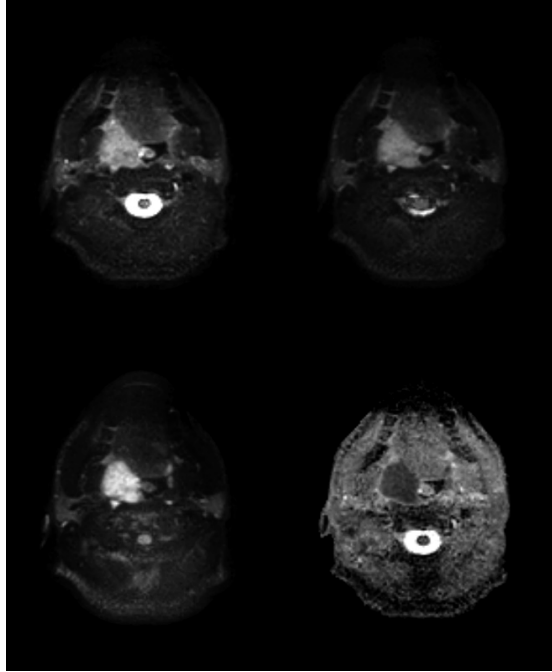
Figure 7.1: Diffusion weighted MRI, acquired with DW-SPLICE, with different diffusion weightings and a calculated ADC map. The primary tumor exhibits diffusion restriction; it shows high signal intensity on the diffusion weighted images and low values in the corresponding ADC map. Top row: b = 0 s/mm$^2$ and b = 200 s/mm$^2$, bottom row: b = 800 s/mm$^2$ and ADC map.

multi shot acquisitions of diffusion weighted data are challenging. This is due to the same problems that hindered TSE acquisitions, motion-induced phase errors. These phase errors will change with every shot making it difficult to align the shots. Some form of phase navigation is required in the multi shot methods. This is typically done using 1D navigators, however, in the case of DW-MRI, these might not suffice because the phase errors have a more complex pattern. To estimate the phase error, a 2D phase navigator would have to be acquired. An alternative approach would be to use a non-cartesian k-space trajectory: PROPELLER (periodically rotated overlapping parallel lines with enhanced reconstruction) [136]. With PROPELLER, a set of adjacent lines (blade) is acquired in the center of k-space with every shot. This blade is then rotated between the shots, such that a common circle of k-space is acquired by all the blades, but every blade also has unique high spatial frequency information from the outer k-space. PROPELLER is a self-navigating method, the common circle of k-space data per blade can be used as navigator data. Combining DW-

SPLICE with a PROPELLER acquisition scheme could provide a gain spatial resolution but also decrease the blurring [34, 81].

Another much needed improvement is acquisition speed. Generally, increasing the acquisition speed, without sacrificing spatial resolution, is done by applying parallel imaging. However, with the current coil setup, the parallel imaging is already maximized. The development of a dedicated receive coil setup with more elements, which is also compatible with the RT immobilization mask, could enable higher parallel imaging factor to speed up the acquisition. Besides the traditional acceleration method, compressed sensing (CS) techniques [137, 138] have been recently introduced in MRI. Following a semi-random undersampling of k-space an iterative reconstruction is performed in order to generate the final image. CS exploits sparsity, the information can be represented using a limited number of non-zero coefficients. The sparsity can be in the image directly, or obtained through some sparsifying transform. Diffusion data seems very well suited for CS, the images themselves are relatively sparse. But a series of corresponding diffusion weighted images is also sparse, the amount of information that changes between the differently diffusion weighted images is limited [139–141]. CS has been shown to enable very high acceleration factors, up to factors of 10 or 20. The disadvantage of CS is the reconstruction time, while the acquisition could be greatly sped up, the iterative reconstruction can take hours.

### Diffusion preparation

The EPI and TSE methods discussed so far are slice selective methods, they apply a slice selective excitation after which the signal is spatially encoded for this slice. 3D acquisitions have an intrinsic higher SNR, making them very promising for diffusion acquisition. To facilitate 3D diffusion acquisitions, driven equilibrium sequences have been proposed [142, 143]. Following diffusion preparation a 90° RF reset pulse is give, tipping all diffusion weighted magnetization to the longitudinal axis. This magnetization can now be excited to perform a 3D readout. This method has been shown with TSE readouts but also with gradient echo readouts (bSSFP, TFE) [144–146]. An added benefit of using 3D over 2D acquisitions is their improved compatibility with CS acceleration, more easily allowing undersampling strategies.

### Fat suppression

The acquisition of DW-MRI is generally accompanied by fat suppression. Unsuppressed fat will appear bright on a diffusion weighted image and has a low ADC value, characteristics similar to tumors. The presence of fat can obscure tumors, degrade image quality and make images harder to interpret and process. Furthermore, unsuppressed fat can shift in the images as a function of the pixel bandwidth, due to the chemical shift between water and fat. In DW-EPI se-

quences this effect is especially pronounced because of its low pixel bandwidth. Fat shifts up to half the field of view are not uncommon here. So even if the tumor is not in close proximity to fat, unsuppressed fat from other parts of the image can shift on top of it.

In chapter 5, the DW-SPLICE sequence was combined with water fat separation in order to achieve more robust fat suppression in the head and neck region. The DW-SPLICE sequence was modified to acquire additional data at different echo times, generating a data set that was suitable for water fat separation. Water fat separation was performed on the b0 images and then applied to the b800 images to remove the fat. The water fat separation could not be performed in the diffusion weighted images directly due to the complications of the previously discussed phase errors. The combination of DW-SPLICE and water-fat separation showed promising results in improving the fat suppression in the head and neck region. Further improvements could also enable direct water fat separation on the diffusion weighted images. Recently, several authors have reported on hybrid techniques that process complex and magnitude-only data sequentially [114, 120].

## 7.2   Diffusion weighted MRI in radiotherapy

### Target volume delineation

The sensitivity of DW-MRI to tissue characteristics such as cell density and tissue organization make it a very promising technique to use in target volume delineation. And the excellent geometrical accuracy of the DW-SPLICE sequence allows for the acquisition of diffusion weighted images that can be used in radiotherapy treatment planning. The information in a diffusion weighted scan is more sparse than in anatomical MR scans, implying that diffusion weighted scans are more straightforward to interpret. This is supported by the high conformity index of delineations on DW-MRI as reported in chapter 4. Three observers had a conformity index of 0.73, indicating good agreement. The inclusion of DW-MRI could help in decreasing delineation variation between different observers.

The sparse nature of the diffusion weighted images also makes them suitable for automatic processing. In chapter 4 a simple method to segment a region in the b800 image using an image intensity threshold of 50% was applied. Delineators then manually adapted this initial segmentation based on information from the ADC map and the rest of the diffusion weighted images. Further development of the automatic segmentation methods should utilize all of the images in the diffusion series. Machine learning methods, such as support vector machines [147] and neural networks [148, 149] seem very well suited for this. The development and training of such methods could benefit greatly from matched

gold standard pathology data that can act as a ground truth [41, 42].

From previous validation studies it was found that automatically segmented PET provides a tumor volume closest to the volume found on histology with a high coverage and the lowest overestimation. Chapter 4 compares delineations on DW-MRI to automatic segmentations of PET. The volumes found on DW-MRI (10.8, 10.5 and 9.0 cm$^3$ respectively) were larger than those on PET (8.0 cm$^3$). The difference was significant for two out of the three observers. There was a substantial overlap between DW-MRI and PET with DSCs of 0.71, 0.69 and 0.72 respectively, indicating that, for a large part, both techniques identify the same target. The DW-MRI and PET volumes were considerably smaller than the clinically used GTV (15.6 cm$^3$) for these patients. However, it is also known, from validation and interobserver studies, that the true GTV tends to be overestimated. The GTVs as segmented on PET still require a CTV margin in order to encompass all tumor tissue [85]. Likewise, the GTVs from DW-MRI will also need an appropriate CTV margin.

This is also indicated by the initial results of an imaging validation study with DW-MRI as described in chapter 6. This imaging validation study continues the one initiated by Caldas-Magalhaes et al. [41] but includes MRI at 3.0 T with an updated imaging protocol, also containing DW-SPLICE. The results of this first patient showed very good correspondence between DW-MRI and pathology, with volumes of 11.7 and 12.3 cm$^3$ respectively. Besides the delineations showing similar volumes, the delineations also had a large spatial overlap as evidenced by a dice similarity coefficient of 0.82. Moreover, the sensitivity and positive predictive value of DW-MRI were high with 0.80 and 0.84 respectively. These first results for DW-MRI are encouraging. Currently, further patient inclusion for this study is ongoing and its results can provide valuable insights in the interpretation of imaging [121].

The addition of DW-SPLICE to the current practice of target volume delineation can help reduce variation among observers and increase target volume delineation accuracy. (Semi-)automatic segmentations can provide a first estimate for the tumor outline. This first estimate can be combined with the segmentation of PET as the region identified by both techniques will be of great importance for treatment.

**Treatment response monitoring**

In addition to target volume delineation DW-MRI can be used evaluate the response to treatment. Successful treatment should result in a loss of cell membrane integrity and a loss of cellularity in general. These changes can be detected as an increase in the ADC values of the tumor. Several studies have investigated the use of DW-MRI for response monitoring and prediction and have showed

promising results [112, 150, 151]. Most studies evaluated changes in the mean ADC of the whole tumor at different time points during treatment. But it is also possible to evaluate the changes in ADC on a per-voxel basis [48]. This does require diffusion weighted images with good geometric accuracy to enable image registration between the different time points. DW-SPLICE, acquired in an immobilization mask, is very well suited for this. Currently, such a study is ongoing at our department.

## 7.3   Future perspectives

### Advances in MRI acquistion

The field of MRI is still very much in development. Advances in hardware and software enable new possibilities and applications. There is an increasing trend in further acceleration of MR acquisitions. Undersampled datasets are reconstructed to full resolution images using advanced reconstruction algorithms. One of the most prominent methods is CS [137, 138]. The additional functional dimension in DW-MRI datasets can be exploited by a CS reconstruction to further accelerate data acquisition. As the MR reconstructions tend to become more complex and computationally demanding, the resources on current clinical MR systems are often insufficient. Therefore, external reconstruction resources, that automatically process acquired data pushed from the MR system, will be very beneficial, not only in developing and prototyping new methods but also to help clinical introduction of promising methods. Non-cartesian acquisition strategies such as PROPELLER can enable higher spatial resolutions. Moreover, these strategies also synergies very well with CS reconstruction methods.

Imaging patients in radiotherapy treatment position, in their customized immobilization masks, limits the type of coils that can be used. Currently, flexible surface coils with two large elements are used. The development of a dedicated coil, compatible with the immobilization mask and with an increased number of receive elements would allow to further exploit parallel imaging strategies and increase SNR.

The imaging for radiotherapy treatment planning in head and neck cancer is multimodal. Taking this into account, another interesting hardware development is the introduction of hybrid PET-MR systems, which allow for the simultaneous acquisition of PET and MR data [152–154]. PET-MR can provide a combination of anatomical, functional and metabolic information in a single exam without misalignment or a time delay between the different acquisitions. The relatively long acquisition time of MR images could be beneficial for the image quality of the PET due to this. Additionally, multimodal reconstructions have been proposed to improve the images of both modalities [155]. An important requirement for PET-MR are electron density maps, for use in correcting

the PET data but also in dose calculations in treatment planning. These would normally be derived from CT, but now have to be derived from MR data.

## Towards daily DW-MRI

The recent introduction of MR-Linac systems enables MR imaging at the time of patient treatment [156]. This provides unique opportunities to perform daily DW-MRI scans. Monitoring changes in the diffusion characteristics of the tumor could help in treatment response assessment and indicate areas in which treatment adaptation would be required. This does require the translation of the results in this thesis from 3.0 T to 1.5 T. Getting sufficient SNR in DW-SPLICE acquisitions on the MRL would most likely be the biggest challenge. The TSE methods benefit from the increased SNR at higher field strengths. Additionally, the MRL has reduced gradient performance when compared with the 3.0 T MR system. This means achieving a certain b-value will take more time and will consequently increase the echo time and lower the SNR. System characterization in terms of eddy currents and gradient performance will allow for further optimization of DW-MRI on the MR-Linac. Promising results in terms of diffusion quantification have already been acquired. Initial ADC measurements using a standardized phantom show excellent correspondence with the calibrated values without image distortions [157].

Chapter 8

# Samenvatting

Radiotherapie wordt vaak toegepast als behandeling van hoofd-hals kanker. Het doel van radiotherapie is het doden van kankercellen met behulp van ioniserende straling. Hoe hoger de stralingsdosis, hoe hoger de kans dat onherstelbare schade wordt aangericht bij de kankercellen. De ioniserende straling kan echter ook schade doen aan het omliggende gezonde weefsel. Het is daarom belangrijk dat de stralingsdosis aan het omliggende weefsel tot een minimum beperkt blijft.

Met moderne radiotherapie technieken is het mogelijk om de dosis driedimensionaal te vormen naar de contouren van de tumor. Op deze manier kan er een hoge dosis afgegeven worden op de tumor, terwijl de dosis aan het omliggende gezonde weefsel minimaal is. Een belangrijke voorwaarde voor de succesvolle toepassing van radiotherapie is dan ook een nauwkeurige definitie van het te behandelen doelvolume.

Bij het definiren van het doelvolume, ook wel intekenen genoemd, wordt gebruik gemaakt van driedimensionale medische beeldvormingstechnieken. Bij het intekenen van de tumor voor radiotherapie van hoofd-hals kanker wordt veelal gebruik gemaakt van CT (*computed tomography*) en PET (*positron emission tomography*). Echter, wordt ook MRI (*magnetic resonance imaging*) steeds vaker gebruikt voor de tumor intekening. MRI heeft een superieur weke delen contrast en is zeer flexibel, het is in staat om via verschillende MRI sequenties beelden met een aantal verschillende contrasten te genereren.

Een van die contrasten is gebaseerd op verschillen in de vrije diffusie van water tussen weefsels, diffusie gewogen MRI (DW-MRI). DW-MRI meet de microscopische mobiliteit van watermoleculen in weefsel. Gedreven door thermische energie verplaatsen watermoleculen zich en afhankelijk van de omgeving zal deze

verplaatsing in meer of mindere mate beperkt worden. In het menselijk lichaam zal de vrije verplaatsing van water moleculen gehinderd worden door aanwezige structuren zoals celmembranen, andere moleculen en weefselorganisatie. Deze beperkte verplaatsing wordt ook wel diffusie restrictie genoemd. Weefsels met een hogere cel dichtheid, zoals tumoren, zullen dus veel diffusie restrictie laten zien. Dit maakt dat het diffusie contrast, DW-MRI, een zeer interessante beeld-vormende techniek is voor gebruik bij het intekenen van tumoren in hoofd-hals radiotherapie.

Dit proefschrift richt zich op het gebruik van DW-MRI binnen de hoofd-hals radiotherapie, in het specifiek voor tumor intekening.

Een belangrijke voorwaarde voor het gebruik van een beeldvormende tech-niek is de geometrische nauwkeurigheid van deze techniek. In **hoofdstuk 2** wordt de geometrische nauwkeurigheid van de meest gebruikte methode van het verkrijgen van DW-MRI beelden, EPI (*echo planar imaging*), gevalueerd. De EPI uitlees techniek is zeer gevoelig voor geometrische vervormingen, met name nabij luchtholtes. Deze luchtholtes veroorzaken namelijk verstoringen van het magnetisch veld en dit heeft invloed op de positie codering in DW-EPI. De gevon-den geometrische vervormingen zijn dermate groot dat de beelden, gemaakt met DW-EPI, ongeschikt zijn voor gebruik bij tumor intekening.

In **hoofdstuk 3** wordt een alternatieve techniek voorgesteld voor het ver-vaardigen van diffusie gewogen beelden: DW-SPLICE. De DW-SPLICE techniek maakt gebruik van een andere uitlees module die veel minder gevoelig is voor ge-ometrische vervormingen. De geometrische vervormingen van DW-SPLICE zijn van dezelfde grootte als conventionele, anatomische, MRI sequenties die reeds gebruikt worden binnen de hoofd-hals radiotherapie.

Het gebruik van DW-SPLICE beelden voor tumor intekening wordt in **hoofd-stuk 4** gevalueerd. Tumor intekeningen op DW-SPLICE beelden worden vergeleken met automatische intekeningen op PET. Van deze automatische intekeningen op PET is uit validatie studies bekend dat deze een zeer goede benadering geven van de daadwerkelijke tumor, zoals bepaald op histopathologie. De tumor intekenin-gen op DW-SPLICE laten sterke overeenkomsten zien met deze automatische intekeningen op PET. Tevens is hier gekeken naar de variatie in intekeningen op DW-SPLICE tussen verschillende intekenaars (*observers*). Deze interobserver variatie bleek laag te zijn, ook in vergelijking met andere interobserver studies in de literatuur.

**Hoofdstuk 5** presenteert een uitbreiding van de DW-SPLICE techniek waar-bij geprobeerd wordt om de vet onderdrukking te verbeteren. Bij de acquisitie van de beelden worden extra metingen verricht zodat het mogelijk wordt om water-vet separatie toe te passen. De combinatie van DW-SPLICE met water-

vet separatie kan het mogelijk maken om een meer robuuste en meer homogene vet suppressie te bewerkstelligen in het hoofd-hals gebied.

Voor de juiste interpretatie van beeldvormende technieken is validatie met histopathologie de gouden standaard. Bij gevorderd strottenhoofd kanker wordt soms het hele strottenhoofd chirurgisch verwijderd (laryngectomie). Na de laryngectomie wordt het chirurgisch preparaat verwerkt en een patholoog bepaalt onder de microscoop de grenzen van de tumor. Het preparaat wordt digitaal gereconstrueerd tot een 3D volume en gekoppeld aan de beeldvorming voorafgaand aan de operatie. Op deze manier kan de beeldvorming gevalideerd worden. Een dergelijke studie is momenteel gaande en in **hoofdstuk 6** worden de eerste resultaten van een patint gepresenteerd. De eerste resultaten laten zien dat het doelvolume, ingetekend op DW-SPLICE, een sterke overeenkomst laat zien met de daadwerkelijk tumor op histopathologie. Dit suggereert dat diffusie gewogen MRI van grote waarde kan zijn bij de intekening van de tumor. Echter, zullen de volledige resultaten van alle patinten moeten worden afgewacht voordat definitieve conclusies getrokken kunnen worden.

In dit proefschrift is het gebruik van diffusie gewogen MRI bij het intekenen van de tumor in hoofd-hals tumoren beschreven. Bij deze toepassing dient rekening te worden gehouden met de mogelijk beperkte geometrische nauwkeurigheid van de beelden. Wanneer diffusie gewogen beelden met voldoende geometrische nauwkeurigheid kunnen worden vervaardigd dan kunnen deze van veel waarde zijn bij het intekenen van hoofd-hals tumoren.

# References

[1] Braakhuis BJ, Leemans CR, Visser O. Incidence and survival trends of head and neck squamous cell carcinoma in the netherlands between 1989 and 2011. Oral Oncology 2014; 50:670–675.

[2] Cijfers over kanker. Integraal kankercentrum Nederland http://www.cijfersoverkanker.nl/; .

[3] Argiris A, Karamouzis MV, Raben D, Ferris RL. Head and neck cancer. The Lancet 2008; 371:1695–1709.

[4] Gregoire V, Neve WD, Eisbruch A, Lee N, den Weyngaert DV, Gestel DV. Intensity-modulated radiation therapy for head and neck carcinoma. The Oncologist 2007; 12:555–564.

[5] Rasch C, Steenbakkers R, van Herk M. Target definition in prostate, head, and neck. Seminars in Radiation Oncology 2005; 15:136–145.

[6] Njeh CF. Tumor delineation: The weakest link in the search for accuracy in radiotherapy. J Med Phys 2008; 33:136–40.

[7] Weiss E, Hess CF. The impact of gross tumor volume (gtv) and clinical target volume (ctv) definition on the total accuracy in radiotherapy theoretical aspects and practical experiences. Strahlenther Onkol 2003; 179:21–30.

[8] Report 83. Journal of the ICRU 2010; 10:NP.1–NP.

[9] Dijkema T, Raaijmakers CP, Haken RKT, Roesink JM, Braam PM, Houweling AC, Moerland MA, Eisbruch A, Terhaard CH. Parotid gland function after radiotherapy: The combined michigan and utrecht experience. International Journal of Radiation Oncology Biology Physics 2010; 78:449–453.

[10] Delouya G, Igidbashian L, Houle A, Bélair M, Boucher L, Cohade C, Beaulieu S, Filion ÉJ, Coulombe G, Hinse M, Martel C, Després P, NguyenTan PF. 18f-FDG-PET imaging in radiotherapy tumor volume delineation in treatment of head and neck cancer. Radiotherapy and Oncology 2011; 101:362–368.

[11] Greco C, Nehmeh SA, Schder H, Gnen M, Raphael B, Stambuk HE, Humm JL, Larson SM, Lee NY. Evaluation of different methods of 18f-FDG-PET target volume delineation in the radiotherapy of head and neck cancer. American Journal of Clinical Oncology 2008; 31:439–445.

[12] Schinagl DAX, Vogel WV, Hoffmann AL, van Dalen JA, Oyen WJ, Kaanders JHAM. Comparison of five segmentation tools for 18f-fluoro-deoxy-glucose positron emission tomography based target volume definition in head and neck cancer. International Journal of Radiation Oncology Biology Physics 2007; 69:1282–1289.

[13] Dirix P, Haustermans K, Vandecaveye V. The value of magnetic resonance imaging for radiotherapy planning. Seminars in Radiation Oncology 2014; 24:151–159.

[14] Ahmed M, Schmidt M, Sohaib A, Kong C, Burke K, Richardson C, Usher M, Brennan S, Riddell A, Davies M, Newbold K, Harrington KJ, Nutting CM. The value of magnetic resonance imaging in target volume delineation of base of tongue tumours – a study using flexible surface coils. Radiotherapy and Oncology 2010; 94:161–167.

[15] Lagendijk JJ, Raaymakers BW, van Vulpen M. The magnetic resonance imaging–linac system. Seminars in Radiation Oncology 2014; 24:207–209.

# References

[16] Mutic S, Dempsey JF. The ViewRay system: Magnetic resonance–guided and controlled radiotherapy. Seminars in Radiation Oncology 2014; 24:196–199.

[17] Bihan DL, Iima M. Diffusion magnetic resonance imaging: What water tells us about biological tissues. PLOS Biology 2015; 13:e1002203.

[18] Bihan DL, Breton E, Lallemand D, Grenier P, Cabanis E, LavalJeantet M. MR imaging of intravoxel incoherent motions: application to diffusion and perfusion in neurologic disorders. Radiology 1986; 161:401–407.

[19] Stejskal EO, Tanner JE. Spin diffusion measurements: Spin echoes in the presence of a time-dependent field gradient. The Journal of Chemical Physics 1965; 42:288–292.

[20] Jones DK, "Diffusion MRI". Oxford University Press, 2010.

[21] Bernstein MA, King KF, Zhou XJ, "Handbook of MRI Pulse Sequences". ACADEMIC PR INC, 2004.

[22] Thoeny HC. Diffusion-weighted mri in head and neck radiology: applications in oncology. Cancer Imaging 2011; 10:209–14.

[23] Thoeny HC, DeKeyzer F, King AD. Diffusion-weighted mr imaging in the head and neck. Radiology 2012; 263:19–32.

[24] Bihan DL, Poupon C, Amadon A, Lethimonnier F. Artifacts and pitfalls in diffusion MRI. Journal of Magnetic Resonance Imaging 2006; 24:478–488.

[25] Farzaneh F, Riederer SJ, Pelc NJ. Analysis of t2 limitations and off-resonance effects on spatial resolution and artifacts in echo-planar imaging. Magnetic resonance in medicine 1990; 14:123–139.

[26] Andersson JL, Hutton C, Ashburner J, Turner R, Friston K. Modeling geometric deformations in EPI time series. NeuroImage 2001; 13:903–919.

[27] Hennig J, Nauerth A, Friedburg H. Rare imaging: a fast imaging method for clinical mr. Magnetic resonance in medicine 1986; 3:823–833.

[28] Beaulieu CF, Zhou X, Cofer GP, Johnson GA. Diffusion-weighted mr microscopy with fast spin-echo. Magnetic resonance in medicine 1993; 30:201–206.

[29] Brockstedt S, Thomsen C, Wirestam R, Holts S, Sthlberg F. Quantitative diffusion coefficient maps using fast spin-echo mri. Magnetic resonance imaging 1998; 16:877–886.

[30] Mori S, van Zijl PC. A motion correction scheme by twin-echo navigation for diffusion-weighted magnetic resonance imaging with multiple rf echo acquisition. Magnetic resonance in medicine 1998; 40:511–516.

[31] Meiboom S, Gill D. Modified spin-echo method for measuring nuclear relaxation times. Review of Scientific Instruments 1958; 29:688–691.

[32] Schick F. Splice: sub-second diffusion-sensitive mr imaging using a modified fast spin-echo acquisition mode. Magn Reson Med 1997; 38:638–44.

[33] LeRoux P. Non-cpmg fast spin echo with full signal. J Magn Reson 2002; 155:278–92.

[34] Pipe JG, Farthing VG, Forbes KP. Multishot diffusion-weighted fse using propeller mri. Magnetic resonance in medicine 2002; 47:42–52.

[35] Alsop DC. Phase insensitive preparation of single-shot rare: application to diffusion imaging in humans. Magn Reson Med 1997; 38:527–33.

[36] Norris DG. Selective parity rare imaging. Magnetic resonance in medicine 2007; 58:643–649.

[37] Norris DG, Bornert P, Reese T, Leibfritz D. On the application of ultra-fast rare experiments. Magn Reson Med 1992; 27:142–64.

[38] Dixon WT. Simple proton spectroscopic imaging. Radiology 1984; 153:189–94.

[39] Barger AV, DeLone DR, Bernstein MA, Welker KM. Fat signal suppression in head and neck imaging using fast spin-echo-ideal technique. AJNR Am J Neuroradiol 2006; 27:1292–4.

[40] Ma J, Jackson EF, Kumar AJ, Ginsberg LE. Improving fat-suppressed t2-weighted imaging of the head and neck with 2 fast spin-echo dixon techniques: initial experiences. AJNR Am J Neuroradiol 2009; 30:42–5.

[41] CaldasMagalhaes J, Kasperts N, Kooij N, van den Berg CA, Terhaard CH, Raaijmakers CP, Philippens ME. Validation of imaging with pathology in laryngeal cancer: accuracy of the registration methodology. International Journal of Radiation Oncology Biology Physics 2012; 82:e289–98.

[42] Daisne JF, Duprez T, Weynand B, Lonneux M, Hamoir M, Reychler H, Grégoire V. Tumor volume in pharyngolaryngeal squamous cell carcinoma: Comparison at CT, MR imaging, and FDG PET and validation with surgical specimen. Radiology 2004; 233:93–100.

[43] Murphy JD, Chisholm KM, Daly ME, Wiegner EA, Truong D, Iagaru A, Maxim PG, Loo BW, Graves EE, Kaplan MJ, Kong C, Le QT. Correlation between metabolic tumor volume and pathologic tumor volume in squamous cell carcinoma of the oral cavity. Radiotherapy and Oncology 2011; 101:356–361.

[44] Wang J, Takashima S, Takayama F, Kawakami S, Saito A, Matsushita T, Momose M, Ishiyama T. Head and neck lesions: Characterization with diffusion-weighted echo-planar MR imaging. Radiology 2001; 220:621–630.

[45] Srinivasan A, Dvorak R, Perni K, Rohrer S, Mukherji S. Differentiation of benign and malignant pathology in the head and neck using 3t apparent diffusion coefficient values: Early experience. American Journal of Neuroradiology 2008; 29:40–44.

[46] Vandecaveye V, Keyzer FD, Poorten VV, Dirix P, Verbeken E, Nuyts S, Hermans R. Head and neck squamous cell carcinoma: Value of diffusion-weighted MR imaging for nodal staging. Radiology 2009; 251:134–146.

[47] Vandecaveye V, Keyzer FD, Nuyts S, Deraedt K, Dirix P, Hamaekers P, Poorten VV, Delaere P, Hermans R. Detection of head and neck squamous cell carcinoma with diffusion weighted MRI after (chemo)radiotherapy: Correlation between radiologic and histopathologic findings. International Journal of Radiation Oncology Biology Physics 2007; 67:960–971.

[48] Galbán CJ, Mukherji SK, Chenevert TL, Meyer CR, Hamstra DA, Bland PH, Johnson TD, Moffat BA, Rehemtulla A, Eisbruch A, Ross BD. A feasibility study of parametric response map analysis of diffusion-weighted magnetic resonance imaging scans of head and neck cancer patients for providing early detection of therapeutic efficacy. Translational Oncology 2009; 2:184–190.

[49] Kim S, Loevner L, Quon H, Sherman E, Weinstein G, Kilger A, Poptani H. Diffusion-weighted magnetic resonance imaging for predicting and detecting early response to chemoradiation therapy of squamous cell carcinomas of the head and neck. Clinical Cancer Research 2009; 15:986–994.

[50] Houweling AC, Wolf AL, Vogel WV, HammingVrieze O, van VlietVroegindeweij C, van de Kamer JB, van der Heide UA. Fdg-pet and diffusion-weighted mri in head-and-neck cancer patients: implications for dose painting. Radiother Oncol 2013; 106:250–4.

[51] CaldasMagalhaes J, Kasperts N, Kooij N, Terhaard C, Raaijmakers C, Philippens M. Validation of diffusion weighted magnetic resonance imaging for automatic tumor delineation in laryngeal cancer. Int J Radiat Oncol Biol Phys 2011; 81:S733–S734.

[52] Padhani AR, Liu G, MuKoh D, Chenevert TL, Thoeny HC, Takahara T, DzikJurasz A, Ross BD, Cauteren MV, Collins D, Hammoud DA, Rustin GJ, Taouli B, Choyke PL. Diffusion-weighted magnetic resonance imaging as a cancer biomarker: Consensus and recommendations. Neoplasia 2009; 11:102–125.

[53] Jezzard P, Balaban RS. Correction for geometric distortion in echo planar images from b0 field variations. Magn Reson Med 1995; 34:65–73.

[54] Reeder SB, Wen Z, Yu H, Pineda AR, Gold GE, Markl M, Pelc NJ. Multicoil dixon chemical species separation with an iterative least-squares estimation method. Magn Reson Med 2004; 51:35–45.

[55] Jenkinson M, Beckmann CF, Behrens TE, Woolrich MW, Smith SM. FSL. NeuroImage 2012; 62:782–790.

[56] Verhappen MH, Pouwels PJ, Ljumanovic R, van der Putten L, Knol DL, DeBree R, Castelijns JA. Diffusion-weighted mr imaging in head and neck cancer: comparison between half-fourier acquired single-shot turbo spin-echo and epi techniques. AJNR Am J Neuroradiol 2012; 33:1239–46.

[57] LeBihan D. Intravoxel incoherent motion imaging using steady-state free precession. Magnetic resonance in medicine 1988; 7:346–351.

[58] Truong TK, kuei Chen N, Song AW. Dynamic correction of artifacts due to susceptibility effects and time-varying eddy currents in diffusion tensor imaging. NeuroImage 2011; 57:1343–1347.

[59] CaldasMagalhaes J, Kooij N, Ligtenberg H, Jager EA, Schakel T, Kasperts N, Pameijer FA, Terhaard CH, Janssen LM, van Diest PJ, Philippens ME, Raaijmakers CP. The accuracy of target delineation in laryngeal and hypopharyngeal cancer. Acta Oncol 2015; 54:1181–7.

# References

[60] Jager EA, Kasperts N, CaldasMagalhaes J, Philippens ME, Pameijer FA, Terhaard CH, Raaijmakers CP. Gtv delineation in supraglottic laryngeal carcinoma: interobserver agreement of ct versus ct-mr delineation. Radiat Oncol 2015; 10:26.

[61] Schakel T, Hoogduin JM, Terhaard CH, Philippens ME. Diffusion weighted mri in head-and-neck cancer: geometrical accuracy. Radiother Oncol 2013; 109:394–7.

[62] MasEstelles F, MateosFernandez M, CarrascosaBisquert B, Facal de Castro F, PuchadesRoman I, MoreraPerez C. Contemporary non-echo-planar diffusion-weighted imaging of middle ear cholesteatomas. Radiographics 2012; 32:1197–213.

[63] van Egmond SL, Stegeman I, Grolman W, Aarts MC. A systematic review of non-echo planar diffusion-weighted magnetic resonance imaging for detection of primary and postoperative cholesteatoma. Otolaryngol Head Neck Surg 2016; 154:233–40.

[64] Juan CJ, Chang HC, Hsueh CJ, Liu HS, Huang YC, Chung HW, Chen CY, Kao HW, Huang GS. Salivary glands: echo-planar versus propeller diffusion-weighted mr imaging for assessment of adcs. Radiology 2009; 253:144–52.

[65] Kito S, Morimoto Y, Tanaka T, Tominaga K, Habu M, Kurokawa H, Yamashita Y, Matsumoto S, Shinohara Y, Okabe S, Matsufuji Y, Takahashi T, Fukuda J, Ohba T. Utility of diffusion-weighted images using fast asymmetric spin-echo sequences for detection of abscess formation in the head and neck region. Oral Surg Oral Med Oral Pathol Oral Radiol Endod 2006; 101:231–8.

[66] Chen X, Xian J, Wang X, Wang Y, Zhang Z, Guo J, Li J. Role of periodically rotated overlapping parallel lines with enhanced reconstruction diffusion-weighted imaging in correcting distortion and evaluating head and neck masses using 3 t mri. Clin Radiol 2014; 69:403–9.

[67] Sakamoto J, Sasaki Y, OtonariYamamoto M, Sano T. Comparison of various methods for quantification of apparent diffusion coefficient of head and neck lesions with haste diffusion-weighted mr imaging. Oral Surg Oral Med Oral Pathol Oral Radiol 2012; 114:266–76.

[68] Wang X, Zhang Z, Chen Q, Li J, Xian J. Effectiveness of 3 t propeller duo diffusion-weighted mri in differentiating sinonasal lymphomas and carcinomas. Clin Radiol 2014; 69:1149–56.

[69] Sakamoto J, Yoshino N, Okochi K, Imaizumi A, Tetsumura A, Kurohara K, Kurabayashi T. Tissue characterization of head and neck lesions using diffusion-weighted mr imaging with splice. Eur J Radiol 2009; 69:260–8.

[70] Sakamoto J, Imaizumi A, Sasaki Y, Kamio T, Wakoh M, OtonariYamamoto M, Sano T. Comparison of accuracy of intravoxel incoherent motion and apparent diffusion coefficient techniques for predicting malignancy of head and neck tumors using half-fourier single-shot turbo spin-echo diffusion-weighted imaging. Magn Reson Imaging 2014; 32:860–6.

[71] Yoshino N, Yamada I, Ohbayashi N, Honda E, Ida M, Kurabayashi T, Maruyama K, Sasaki T. Salivary glands and lesions: evaluation of apparent diffusion coefficients with split-echo diffusion-weighted mr imaging–initial results. Radiology 2001; 221:837–42.

[72] Schouten CS, de Bree R, van der Putten L, Noij DP, Hoekstra OS, Comans EF, Witte BI, Doornaert PA, Leemans CR, Castelijns JA. Diffusion-weighted epi- and haste-mri and 18f-fdg-pet-ct early during chemoradiotherapy in advanced head and neck cancer. Quant Imaging Med Surg 2014; 4:239–50.

[73] Verduijn GM, Bartels LW, Raaijmakers CP, Terhaard CH, Pameijer FA, van den Berg CA. Magnetic resonance imaging protocol optimization for delineation of gross tumor volume in hypopharyngeal and laryngeal tumors. Int J Radiat Oncol Biol Phys 2009; 74:630–6.

[74] Chenevert TL, Galban CJ, Ivancevic MK, Rohrer SE, Londy FJ, Kwee TC, Meyer CR, Johnson TD, Rehemtulla A, Ross BD. Diffusion coefficient measurement using a temperature-controlled fluid for quality control in multicenter studies. J Magn Reson Imaging 2011; 34:983–7.

[75] Dietrich O, Raya JG, Sommer J, Deimling M, Reiser MF, BaurMelnyk A. A comparative evaluation of a rare-based single-shot pulse sequence for diffusion-weighted mri of musculoskeletal soft-tissue tumors. Eur Radiol 2005; 15:772–83.

[76] Foltz WD, Porter DA, Simeonov A, Aleong A, Jaffray D, Chung P, Han K, Menard C. Readout-segmented echo-planar diffusion-weighted imaging improves geometric performance for image-guided radiation therapy of pelvic tumors. Radiother Oncol 2015; 117:525–31.

[77] Taviani V, Nagala S, Priest AN, McLean MA, Jani P, Graves MJ. 3t diffusion-weighted mri of the thyroid gland with reduced distortion: preliminary results. Br J Radiol 2013; 86:20130022.

[78]  Wilm BJ, Svensson J, Henning A, Pruessmann KP, Boesiger P, Kollias SS. Reduced field-of-view mri using outer volume suppression for spinal cord diffusion imaging. Magn Reson Med 2007; 57:625–30.

[79]  Jin N, Deng J, Zhang L, Zhang Z, Lu G, Omary RA, Larson AC. Targeted single-shot methods for diffusion-weighted imaging in the kidneys. J Magn Reson Imaging 2011; 33:1517–25.

[80]  Burbach JP, Kleijnen JP, Reerink O, Seravalli E, Philippens ME, Schakel T, van Asselen B, Raaymakers BW, van Vulpen M, Intven M. Inter-observer agreement of mri-based tumor delineation for preoperative radiotherapy boost in locally advanced rectal cancer. Radiother Oncol 2016; 118:399–407.

[81]  Deng J, Omary RA, Larson AC. Multishot diffusion-weighted splice propeller mri of the abdomen. Magn Reson Med 2008; 59:947–53.

[82]  Baumann M, Krause M, Overgaard J, Debus J, Bentzen SM, Daartz J, Richter C, Zips D, Bortfeld T. Radiation oncology in the era of precision medicine. Nat Rev Cancer 2016; 16:234–49.

[83]  Chen AM, Chin R, Beron P, Yoshizaki T, Mikaeilian AG, Cao M. Inadequate target volume delineation and local-regional recurrence after intensity-modulated radiotherapy for human papillomavirus-positive oropharynx cancer. Radiotherapy and Oncology 2017; 123:412–418.

[84]  Cooper JS, Mukherji SK, Toledano AY, Beldon C, Schmalfuss IM, Amdur R, Sailer S, Loevner LA, Kousouboris P, Ang KK, Cormack J, Sicks J. An evaluation of the variability of tumor-shape definition derived by experienced observers from ct images of supraglottic carcinomas (acrin protocol 6658). Int J Radiat Oncol Biol Phys 2007; 67:972–5.

[85]  Ligtenberg H, Jager EA, CaldasMagalhaes J, Schakel T, Pameijer FA, Kasperts N, Willems SM, Terhaard CHJ, Raaijmakers CPJ, Philippens MEP. Modality-specific target definition for laryngeal and hypopharyngeal cancer on fdg-pet, ct and mri. Radiotherapy and Oncology 2017; 123:63–70.

[86]  Zaidi H, ElNaqa I. Pet-guided delineation of radiation therapy treatment volumes: a survey of image segmentation techniques. Eur J Nucl Med Mol Imaging 2010; 37:2165–87.

[87]  Cheebsumon P, Boellaard R, de Ruysscher D, van Elmpt W, van Baardwijk A, Yaqub M, Hoekstra OS, Comans EF, Lammertsma AA, van Velden FH. Assessment of tumour size in pet/ct lung cancer studies: Pet- and ct-based methods compared to pathology. EJNMMI Res 2012; 2:56.

[88]  Daisne JF, Sibomana M, Bol A, Doumont T, Lonneux M, Gregoire V. Tri-dimensional automatic segmentation of pet volumes based on measured source-to-background ratios: influence of reconstruction algorithms. Radiother Oncol 2003; 69:247–50.

[89]  Zaidi H, Abdoli M, Fuentes CL, ElNaqa IM. Comparative methods for pet image segmentation in pharyngolaryngeal squamous cell carcinoma. Eur J Nucl Med Mol Imaging 2012; 39:881–91.

[90]  Geets X, Lee JA, Bol A, Lonneux M, Gregoire V. A gradient-based method for segmenting fdg-pet images: methodology and validation. Eur J Nucl Med Mol Imaging 2007; 34:1427–38.

[91]  Brambilla M, Matheoud R, Secco C, Loi G, Krengli M, Inglese E. Threshold segmentation for pet target volume delineation in radiation treatment planning: The role of target-to-background ratio and target size. Medical Physics 2008; 35:1207–1213.

[92]  Matheoud R, Monica PD, Loi G, Vigna L, Krengli M, Inglese E, Brambilla M. Influence of reconstruction settings on the performance of adaptive thresholding algorithms for fdg-pet image segmentation in radiotherapy planning. Journal of Applied Clinical Medical Physics 2011; 12:115–132.

[93]  van Rossum PS, van Lier AL, van Vulpen M, Reerink O, Lagendijk JJ, Lin SH, van Hillegersberg R, Ruurda JP, Meijer GJ, Lips IM. Diffusion-weighted magnetic resonance imaging for the prediction of pathologic response to neoadjuvant chemoradiotherapy in esophageal cancer. Radiother Oncol 2015; 115:163–70.

[94]  Schakel T, Hoogduin JM, Terhaard CHJ, Philippens MEP. Technical note: Diffusion-weighted mri with minimal distortion in head-and-neck radiotherapy using a turbo spin echo acquisition method. Med Phys 2017; 44:4188–4193.

[95]  Aristophanous M, Penney BC, Martel MK, Pelizzari CA. A gaussian mixture model for definition of lung tumor volumes in positron emission tomography. Med Phys 2007; 34:4223–35.

# References

[96]  CaldasMagalhaes J, Raaijmakers CP, Aristophanous M, Lee JA, Kasperts N, Jager EA, Kooij N, Terhaard CH, Philippens ME. Fdg-pet semi automatic segmentation methods for gtv delineation in laryngeal and hypopharyngeal cancer. International Journal of Radiation Oncology Biology Physics 2014; 90:S536.

[97]  Aristophanous M, Pelizzari CA. The evaluation of a highly automated mixture model based technique for PET tumor volume segmentation. In: "Medical Imaging 2008: Image Processing (Reinhardt JM, Pluim JPW, Eds.), In: "Medical Imaging 2008: Image Processing (Reinhardt JM, Pluim JPW, Eds.), mar 2008

[98]  Kouwenhoven E, Giezen M, Struikmans H. Measuring the similarity of target volume delineations independent of the number of observers. Phys Med Biol 2009; 54:2863–73.

[99]  Zou KH, Warfield SK, Bharatha A, Tempany CMC, Kaus MR, Haker SJ, Wells WM, Jolesz FA, Kikinis R. Statistical validation of image segmentation quality based on a spatial overlap index. Acad Radiol 2004; 11:178–89.

[100]  Loo SW, Martin WMC, Smith P, Cherian S, Roques TW. Interobserver variation in parotid gland delineation: a study of its impact on intensity-modulated radiotherapy solutions with a systematic review of the literature. The British Journal of Radiology 2012; 85:1070–1077.

[101]  Thiagarajan A, Caria N, Schder H, Iyer NG, Wolden S, Wong RJ, Sherman E, Fury MG, Lee N. Target volume delineation in oropharyngeal cancer: Impact of pet, mri, and physical examination. International Journal of Radiation Oncology Biology Physics 2012; 83:220–227.

[102]  Geets X, Daisne JF, Arcangeli S, Coche E, Poel MD, Duprez T, Nardella G, Grgoire V. Inter-observer variability in the delineation of pharyngo-laryngeal tumor, parotid glands and cervical spinal cord: Comparison between ct-scan and mri. Radiotherapy and Oncology 2005; 77:25–31.

[103]  Mukesh M, Benson R, Jena R, Hoole A, Roques T, Scrase C, Martin C, Whitfield GA, Gemmill J, Jefferies S. Interobserver variation in clinical target volume and organs at risk segmentation in post-parotidectomy radiotherapy: can segmentation protocols help? The British Journal of Radiology 2012; 85:e530–e536.

[104]  Schouten CS, de Graaf P, Alberts FM, Hoekstra OS, Comans EF, Bloemena E, Witte BI, Sanchez E, Leemans CR, Castelijns JA, de Bree R. Response evaluation after chemoradiotherapy for advanced nodal disease in head and neck cancer using diffusion-weighted mri and 18f-fdg-pet-ct. Oral Oncol 2015; 51:541–7.

[105]  Surov A, Stumpp P, Meyer HJ, Gawlitza M, Hohn AK, Boehm A, Sabri O, Kahn T, Purz S. Simultaneous (18)f-fdg-pet/mri: Associations between diffusion, glucose metabolism and histopathological parameters in patients with head and neck squamous cell carcinoma. Oral Oncol 2016; 58:14–20.

[106]  Varoquaux A, Rager O, Lovblad KO, Masterson K, Dulguerov P, Ratib O, Becker CD, Becker M. Functional imaging of head and neck squamous cell carcinoma with diffusion-weighted mri and fdg pet/ct: quantitative analysis of adc and suv. Eur J Nucl Med Mol Imaging 2013; 40:842–52.

[107]  FruehwaldPallamar J, Czerny C, Mayerhoefer ME, Halpern BS, EderCzembirek C, Brunner M, Schuetz M, Weber M, Fruehwald L, Herneth AM. Functional imaging in head and neck squamous cell carcinoma: correlation of pet/ct and diffusion-weighted imaging at 3 tesla. Eur J Nucl Med Mol Imaging 2011; 38:1009–19.

[108]  Subesinghe M, Scarsbrook AF, Sourbron S, Wilson DJ, McDermott G, Speight R, Roberts N, Carey B, Forrester R, Gopal SV, Sykes JR, Prestwich RJ. Alterations in anatomic and functional imaging parameters with repeated fdg pet-ct and mri during radiotherapy for head and neck cancer: a pilot study. BMC Cancer 2015; 15:137.

[109]  LeBihan D, Breton E, Lallemand D, Aubin ML, Vignaud J, LavalJeantet M. Separation of diffusion and perfusion in intravoxel incoherent motion mr imaging. Radiology 1988; 168:497–505.

[110]  Driessen JP, van Kempen PM, van der Heijden GJ, Philippens ME, Pameijer FA, Stegeman I, Terhaard CH, Janssen LM, Grolman W. Diffusion-weighted imaging in head and neck squamous cell carcinomas: a systematic review. Head Neck 2015; 37:440–8.

[111]  Lambrecht M, VanHerck H, DeKeyzer F, Vandecaveye V, Slagmolen P, Suetens P, Hermans R, Nuyts S. Redefining the target early during treatment. can we visualize regional differences within the target volume using sequential diffusion weighted mri? Radiother Oncol 2014; 110:329–34.

[112] Vandecaveye V, Dirix P, DeKeyzer F, Op de Beeck K, VanderPoorten V, Hauben E, Lambrecht M, Nuyts S, Hermans R. Diffusion-weighted magnetic resonance imaging early after chemoradiotherapy to monitor treatment response in head-and-neck squamous cell carcinoma. Int J Radiat Oncol Biol Phys 2012; 82:1098–107.

[113] Burakiewicz J, CharlesEdwards GD, Goh V, Schaeffter T. Water-fat separation in diffusion-weighted epi using an ideal approach with image navigator. Magn Reson Med 2015; 73:964–72.

[114] Hernando D, Karampinos DC, King KF, Haldar JP, Majumdar S, Georgiadis JG, Liang ZP. Removal of olefinic fat chemical shift artifact in diffusion mri. Magn Reson Med 2011; 65:692–701.

[115] Hwang KP, Ma J, Madhuranthakam AJ, Han ET, Sun W, Slavens ZW, Alsop DC. Diffusion weighted ssfse with dixon fat-water separation. Proc. Intl. Soc. Mag. Reson. Med. 16 2008; p. 2293.

[116] Wang X, Eggers H, Pinho MC, Pedrosa I, Lenkinski RE, Madhuranthakam AJ. Diffusion weighted imaging using a dixon based single shot turbo spin echo. Proc. Intl. Soc. Mag. Reson. Med. 25 2017; p. 172.

[117] Tsao J, Jiang Y. Hierarchical ideal: fast, robust, and multiresolution separation of multiple chemical species from multiple echo times. Magn Reson Med 2013; 70:155–9.

[118] Partridge SC, Singer L, Sun R, Wilmes LJ, Klifa CS, Lehman CD, Hylton NM. Diffusion-weighted mri: influence of intravoxel fat signal and breast density on breast tumor conspicuity and apparent diffusion coefficient measurements. Magn Reson Imaging 2011; 29:1215–21.

[119] Baron P, Dorrius MD, Kappert P, Oudkerk M, Sijens PE. Diffusion-weighted imaging of normal fibroglandular breast tissue: influence of microperfusion and fat suppression technique on the apparent diffusion coefficient. NMR Biomed 2010; 23:399–405.

[120] Burakiewicz J, Hooijmans MT, Webb AG, Verschuuren JJ, Niks EH, Kan HE. Improved olefinic fat suppression in skeletal muscle dti using a magnitude-based dixon method. Magn Reson Med 2017; .

[121] Ligtenberg H, Schakel T, Dankbaar JW, Ruiter LN, Peltenburg B, Willems SM, Kasperts N, Terhaard CHJ, Raaijmakers CPJ, Philippens MEP. Target volume delineation using diffusion-weighted imaging for MR-guided radiotherapy: A case series of laryngeal cancer validated by pathology. Cureus 2018; .

[122] Kidwell CS, Alger JR, Salle FD, Starkman S, Villablanca P, Bentson J, Saver JL. Diffusion MRI in patients with transient ischemic attacks. Stroke 1999; 30:1174–1180.

[123] Bihan DL. Looking into the functional architecture of the brain with diffusion MRI. Nature Reviews Neuroscience 2003; 4:469–480.

[124] Andersson JL, Skare S. A model-based method for retrospective correction of geometric distortions in diffusion-weighted EPI. NeuroImage 2002; 16:177–199.

[125] Andersson JL, Skare S, Ashburner J. How to correct susceptibility distortions in spin-echo echo-planar images: application to diffusion tensor imaging. NeuroImage 2003; 20:870–888.

[126] Hardy CJ, Giaquinto RO, Piel JE, AAS KWR, Marinelli L, Blezek DJ, Fiveland EW, Darrow RD, Foo TK. 128-channel body MRI with a flexible high-density receiver-coil array. Journal of Magnetic Resonance Imaging 2008; 28:1219–1225.

[127] Ohliger MA, Sodickson DK. An introduction to coil array design for parallel MRI. NMR in Biomedicine 2006; 19:300–315.

[128] Gruetter R. Automatic, localized in vivo adjustment of all first- and second-order shim coils. Magnetic resonance in medicine 1993; 29:804–811.

[129] Prammer MG, Haselgrove JC, Shinnar M, Leigh JS. A new approach to automatic shimming. Journal of Magnetic Resonance (1969) 1988; 77:40–52.

[130] Vanzijl P, Sukumar S, Johnson M, Webb P, Hurd R. Optimized shimming for high-resolution NMR using three-dimensional image-based field mapping. Journal of Magnetic Resonance, Series A 1994; 111:203–207.

[131] Wen H, Jaffer FA. An in vivo automated shimming method taking into account shim current constraints. Magnetic resonance in medicine 1995; 34:898–904.

[132] Siero J, Philippens M, Simonetti A, Hoogduin J, Luijten P. Cost function guided image based bo shimming at 3t for efficient fat suppression in liver and prostate imaging. Proc Int Soc Magn Reson Med 2010; 18:2589.

# References

[133] Simonetti A, Holthuizen R, Harder C et al. 3d breast segmentation for image based shimming. Proc Int Soc Magn Reson Med 2009; 17:2114.

[134] Simonetti A, Beck G, Hoogduin J, Siero J, Herigault G. Image-based weighted b0 shimming using a fast multi-echo dixon technique: feasibility for abdominal imaging. Proc Int Soc Magn Reson Med 2011; 19:2718.

[135] Schakel T, Siero J, Hoogduin J, Philippens M. The impact of shimming on fat suppression in head-and-neck mri: current practice vs an image based approach. Proc Int Soc Magn Reson Med 2016; 24:1333.

[136] Pipe JG. Motion correction with propeller mri: application to head motion and free-breathing cardiac imaging. Magnetic resonance in medicine 1999; 42:963–969.

[137] Lustig M, Donoho D, Pauly JM. Sparse mri: The application of compressed sensing for rapid mr imaging. Magnetic resonance in medicine 2007; 58:1182–1195.

[138] Lustig M, Donoho D, Santos J, Pauly J. Compressed sensing MRI. IEEE Signal Processing Magazine 2008; 25:72–82.

[139] Ning L, Setsompop K, Michailovich O, Makris N, Shenton ME, Westin CF, Rathi Y. A joint compressed-sensing and super-resolution approach for very high-resolution diffusion imaging. NeuroImage 2016; 125:386–400.

[140] Paulsen JL, Cho H, Cho G, Song YQ. Acceleration of multi-dimensional propagator measurements with compressed sensing. Journal of Magnetic Resonance 2011; 213:166–170.

[141] Wu Y, Zhu YJ, Tang QY, Zou C, Liu W, Dai RB, Liu X, Wu EX, Ying L, Liang D. Accelerated MR diffusion tensor imaging using distributed compressed sensing. Magnetic Resonance in Medicine 2013; 71:763–772.

[142] Thomas DL, Pell GS, Lythgoe MF, Gadian DG, Ordidge RJ. A quantitative method for fast diffusion imaging using magnetization-prepared turboflash. Magnetic resonance in medicine 1998; 39:950–960.

[143] Coremans J, Spanoghe M, Budinsky L, Sterckx J, Luypaert R, Eisendrath H, Osteaux M. A comparison between different imaging strategies for diffusion measurements with the centric phase-encoded TurboFLASH sequence. Journal of Magnetic Resonance 1997; 124:323–342.

[144] Zhang Q, Coolen BF, Versluis MJ, Strijkers GJ, Nederveen AJ. Diffusion-prepared stimulated-echo turbo spin echo (DPsti-TSE): An eddy current-insensitive sequence for three-dimensional high-resolution and undistorted diffusion-weighted imaging. NMR in Biomedicine 2017; 30:e3719.

[145] Jeong EK, Kim SE, Parker DL. High-resolution diffusion-weighted 3d MRI, using diffusion-weighted driven-equilibrium (DW-DE) and multishot segmented 3d-SSFP without navigator echoes. Magnetic Resonance in Medicine 2003; 50:821–829.

[146] Yamashita K, Yoshiura T, Hiwatashi A, Obara M, Togao O, Matsumoto N, Kikuchi K, Honda H. High-resolution three-dimensional diffusion-weighted imaging of middle ear cholesteatoma at 3.0t MRI: Usefulness of 3d turbo field-echo with diffusion-sensitized driven-equilibrium preparation (TFE–DSDE) compared to single-shot echo-planar imaging. European Journal of Radiology 2013; 82:e471–e475.

[147] Artan Y, Haider MA, Langer DL, van der Kwast TH, Evans AJ, Yang Y, Wernick MN, Trachtenberg J, Yetik IS. Prostate cancer localization with multispectral MRI using cost-sensitive support vector machines and conditional random fields. IEEE Transactions on Image Processing 2010; 19:2444–2455.

[148] Trebeschi S, van Griethuysen JJM, Lambregts DMJ, Lahaye MJ, Parmer C, Bakers FCH, Peters NHGM, BeetsTan RGH, Aerts HJWL. Deep learning for fully-automated localization and segmentation of rectal cancer on multiparametric MR. Scientific Reports 2017; 7.

[149] van Heeswijk MM, Lambregts DM, van Griethuysen JJ, Oei S, Rao SX, de Graaff CA, Vliegen RF, Beets GL, Papanikolaou N, BeetsTan RG. Automated and semiautomated segmentation of rectal tumor volumes on diffusion-weighted mri: Can it replace manual volumetry? International Journal of Radiation Oncology Biology Physics 2016; 94:824 – 831.

[150] King AD, Mo FKF, Yu KH, Yeung DKW, Zhou H, Bhatia KS, Tse GMK, Vlantis AC, Wong JKT, Ahuja AT. Squamous cell carcinoma of the head and neck: diffusion-weighted MR imaging for prediction and monitoring of treatment response. European Radiology 2010; 20:2213–2220.

[151] Thoeny HC, Ross BD. Predicting and monitoring cancer treatment response with diffusion-weighted MRI. Journal of Magnetic Resonance Imaging 2010; 32:2–16.

[152] Paulus DH, Thorwath D, Schmidt H, Quick HH. Towards integration of PET/MR hybrid imaging into radiation therapy treatment planning. Medical Physics 2014; 41:072505.

[153] Varoquaux A, Rager O, Dulguerov P, Burkhardt K, Ailianou A, Becker M. Diffusion-weighted and PET/MR imaging after radiation therapy for malignant head and neck tumors. RadioGraphics 2015; 35:1502–1527.

[154] Queiroz MA, Huellner MW. PET/MR in cancers of the head and neck. Seminars in Nuclear Medicine 2015; 45:248–265.

[155] Knoll F, Holler M, Koesters T, Otazo R, Bredies K, Sodickson DK. Joint MR-PET reconstruction using a multi-channel image regularizer. IEEE Transactions on Medical Imaging 2017; 36:1–16.

[156] Raaymakers BW, JrgenliemkSchulz IM, Bol GH, Glitzner M, Kotte ANTJ, van Asselen B, de Boer JCJ, Bluemink JJ, Hackett SL, Moerland MA, Woodings SJ, Wolthaus JWH, van Zijp HM, Philippens MEP, Tijssen R, Kok JGM, de Groot-van Breugel EN, Kiekebosch I, Meijers LTC, Nomden CN, Sikkes GG, Doornaert PAH, Eppinga WSC, Kasperts N, Kerkmeijer LGW, Tersteeg JHA, Brown KJ, Pais B, Woodhead P, Lagendijk JJW. First patients treated with a 1.5 t MRI-linac: clinical proof of concept of a high-precision, high-field MRI guided radiotherapy treatment. Physics in Medicine & Biology 2017; 62:L41–L50.

[157] Schakel T, Tijssen H, Hoogduin J, Philippens M. Robust quantitative diffusion weighted mr on an mr-linac system. Proc Int Soc Magn Reson Med 2018; 26:8558.

# Publications

## Journal articles

**Schakel T.**, Peltenburg B., Dankbaar J.W., Cardenas C.E., Aristophanous M., Terhaard C.H.J., Hoogduin J.M., Philippens M.E.P.. Evaluation of diffusion weighted imaging for tumor delineation in head-and-neck radiotherapy by comparison with automatically segmented 18 f-fluorodeoxyglucose positron emission tomography. *Phys Imaging Rad Onc* 2018; 5:13–18..

**Schakel T.**, Hoogduin J.M., Terhaard C.H.J., Philippens M.E.P.. Technical note: Diffusion-weighted MRI with minimal distortion in head-and-neck radiotherapy using a turbo spin echo acquisition method. *Med. Phys.* 2017; 44:4188–4193.

Ligtenberg H., Jager E.A., CaldasMagalhaes J., **Schakel T.**, Pameijer F.A., Kasperts N., Willems S.M., Terhaard C.H.J., Raaijmakers C.P.J., Philippens M.E.P.. Modality-specific target definition for laryngeal and hypopharyngeal cancer on FDG-PET, CT and MRI. *Radiother. Oncol.* 2017; 123:63–70.

Jager E.A., Ligtenberg H., CaldasMagalhaes J., **Schakel T.**, Philippens M.E.P., Pameijer F.A., Kasperts N., Willems S.M., Terhaard C.H.J., Raaijmakers C.P.J.. Validated guidelines for tumor delineation on magnetic resonance imaging for laryngeal and hypopharyngeal cancer. *Acta Oncol.* 2016; 55:1305–1312.

Burbach J.P.M., Kleijnen J.P.J., Reerink O., Seravalli E., Philippens M.E.P., **Schakel T.**, van Asselen B., Raaymakers B.W., van Vulpen M., Intven M.. Inter-observer agreement of MRI-based tumor delineation for preoperative radiotherapy boost in locally advanced rectal cancer. *Radiother. Oncol.* 2016; 118:399–407.

Jager E.A., Willems S.M., **Schakel T.**, Kooij N., Slootweg P.J., Philippens M.E.P., CaldasMagalhaes J., Terhaard C.H.J., Raaijmakers C.P.J.. Interobserver variation among pathologists for delineation of tumor on H&E-sections of laryngeal and hypopharyngeal carcinoma. How good is the gold standard? *Acta Oncol.* 2016; 55:391–395.

Brisset J.C., Hoff B.A., Chenevert T.L., Jacobson J.A., Boes J.L., Galbn S., Rehemtulla A., Johnson T.D., Pienta K.J., Galbn C.J., Meyer C.R., **Schakel T.**, Nicolay K., Alva A.S., Hussain M., Ross B.D.. Integrated multimodal imaging of dynamic bone-tumor alterations associated with metastatic prostate cancer. *PloS one* 2015; 10:e0123877.

CaldasMagalhaes J., Kooij N., Ligtenberg H., Jager E.A., **Schakel T.**, Kasperts N., Pameijer F.A., Terhaard C.H.J., Janssen L.M., van Diest P.J., Philippens M.E.P., Raaijmakers C.P.J.. The accuracy of target delineation in laryngeal and hypopharyngeal cancer. *Acta Oncol.* 2015; 54:1181–1187.

**Schakel T.**, Hoogduin J.M., Terhaard C.H.J., Philippens M.E.P.. Diffusion weighted MRI in head-and-neck cancer: geometrical accuracy. *Radioth. Oncol.* 2013; 109:394–397.

Houweling A.C., **Schakel T.**, van den Berg C.A.T., Philippens M.E.P., Roesink J.M., Terhaard C.H.J., Raaijmakers C.P.J.. MRI to quantify early radiation-induced changes in the salivary glands. *Radioth. Oncol.* 2011; 100:386–389.

Loerakker S., Oomens C.W.J., Manders E., **Schakel T.**, Bader D.L., Baaijens F.P.T., Nicolay K., Strijkers G.J.. Ischemia-reperfusion injury in rat skeletal muscle assessed with T2-weighted and dynamic contrast-enhanced MRI. Magn. Res. Med. 2011; 66:528–537.

# Conference Proceedings

**Schakel T.**, Peltenburg B., Dankbaar J.W., Cardenas C.E., Aristophanous M., Terhaard C.H.J., Hoogduin J.M., Philippens M.E.P.. Diffusion weighted fast spin echo for tumor delineation in head-and-neck radiotherapy: a comparison with FDG-PET. *Proc. 25th ISMRM* 2017.

Bruijnen T., Tijssen R.H.N., Philippens M.E.P., Terhaard C.H.J., **Schakel T.**, Lagendijk J.J.W., Raaijmakers C.P.J., Stemkens B.. Intra-fraction motion quantification of head-and-neck tumors using dynamic MRI. *Proc ESTRO* 2017.

Peltenburg B., **Schakel T.**, Dankbaar J.W., Aristophanous M., Terhaard C.H.J., Hoogduin J.M., Philippens M.E.P.. Tumor volume delineation using non-EPI diffusion weighted MRI and FDG-PET in head-and-neck patients. *Proc ESTRO* 2017.

**Schakel T.**, Siero J.C.W., Hoogduin J.M., Philippens M.E.P.. The impact of shimming on fat suppression in head-and-neck MRI: current practice vs an image based approach *Proc. 24th ISMRM* 2016.

Terhaard C.H.J., Jager E.A., Philippens M.E.P., **Schakel T.**, Caldas-Magalhaes J., Ligtenberg H., Kasperts N., Pameijer F.A., Willems S.M., Raaijmakers C.P.J. and Validation Is Crucial in Head and Neck Translational Imaging Research. *Proc Multidisciplinary head and neck cancers symposium* 2016.

Bruijnen T., Stemkens B., Philippens M.E.P., Canjels L.P.W., Tijssen R.H.N., **Schakel T.**, Terhaard C.H.J., Lagendijk J.J.W., Raaijmakers C.P.J., Intra-fraction motion characterization of head-and-neck tumors using cine-MRI. *Proc ESTRO* 2016.

Ligtenberg H., Jager E.A., Caldas-Magalhaes J., **Schakel T.**, Kasperts N., Pameijer F.A., Kooij N., Janssen L.M., Terhaard C.H.J., Willems S.M., Raaijmakers C.P.J. and Philippens M.E.P.. GTV delineation of laryngopharyngeal carcinoma on PET is more accurate than on CT and MRI. *Proc ESTRO* 2016.

Jager E.A., Ligtenberg H., Philippens M.E.P., Caldas-Magalhaes J., **Schakel T.**, Pameijer F.A., Kasperts N., Kooij N., Willems S.M., Terhaard C.H.J., Raaijmakers C.P.J.. The accuracy of tumor delineation on MR-images for laryngeal and hypophargeal cancer. *Proc ESTRO* 2016.

Jager E.A., Raaijmakers C.P.J., Ligtenberg H., Caldas-Magalhaes J., **Schakel T.**, Pameijer F.A., Kasperts N., Kooij N., Willems S.M., Terhaard C.H.J., Philippens M.E.P.. Guideline development for tumor delineation on MR-images for laryngeal and hypophargeal cancer. *Proc ESTRO* 2016.

Ligtenberg H., Jager E.A., Caldas-Magalhaes J., **Schakel T.**, Kasperts N., Pameijer F.A., Janssen L.M., Terhaard C.H.J., Willems S.M., Raaijmakers C.P.J. and Philippens M.E.P.. Improvement of Target Definition for Laryngeal and Hypopharyngeal Cancer on Computed Tomography, Magnetic Resonance Imaging, and 18-FDG Positron Emission Tomography Validated by Histopathology. *Proc ASTRO* 2016.

**Schakel T.**, Stemkens B., Hoogduin J.M., Philippens M.E.P.. Fat suppression for DW-FSE sequences using an integrated multi-acquisition dixon method *Proc. 23rd ISMRM* 2015.

Ligtenberg H., Jager E.A., Caldas-Magalhaes J., **Schakel T.**, Willems S.M., Kooij N., Terhaard C.H.J., Pameijer F.A., Kasperts N., Janssen L.M., Raaijmakers C.P.J. and Philippens M.E.P.. Comparison of GTV delineations on CT, MRI and FDG-PET of laryngeal and hypopharyngeal carcinoma with histopathology. *Proc ESTRO* 2015.

Jager E.A., **Schakel T.**, Caldas-Magalhaes J., Ligtenberg H., Kasperts N., Philippens M.E.P., Pameijer F.A., Terhaard C.H.J., Willems S.M., Raaijmakers C.P.J.. Overestimation of tumor volume of laryngeal/hypopharyngeal cancer on MRI in clinical radiotherapy practice. *Proc ESTRO* 2015.

Ligtenberg H., Jager E.A., Caldas-Magalhaes J., **Schakel T.**, Willems S.M., Terhaard C.H.J., Pameijer F.A., Kasperts N., Janssen L.M., Raaijmakers C.P.J. and Philippens M.E.P.. Margin Reduction Based on Comparison of Histopathology with Delineations on CT, MRI and FDG-PET in Laryngeal and Hypopharyngeal Cancer. *Proc ASTRO* 2015.

**Schakel T.**, Hoogduin J.M., Philippens M.E.P.. In vivo high resolution, undistorted diffusion weighted imaging using DSDE-TFE *Proc. 22nd ISMRM* 2014.

Jager E.A., **Schakel T.**, Willems S.M., Kooij N., Slootweg P.J., Philippens M.E.P., Terhaard C.H.J., Raaijmakers C.P.J.. Delineation of tumor tissue on H&E-sections of laryngeal carcinoma. How accurate is the gold standard? *Proc ESTRO* 2014.

Jager E.A., Terhaard C.H.J., Pameijer F.A., Kasperts N., **Schakel T.**, Caldas-Magalhaes J., Philippens M.E.P., Kooij N., Raaijmakers C.P.J.. Improved GTV Delineation of Laryngeal/Hypopharyngeal Carcinoma on MRI by the Use of Delineation Guidelines. *Proc ASTRO* 2014

**Schakel T.**, van Yperen G.H., van den Brink J., Pameijer F.A., Terhaard C.H.J., Hoogduin J.M., Philippens M.E.P.. Diffusion weighted imaging in head-and-neck cancer: comparison between echo planar and turbo spin echo sequences *Proc. 21st ISMRM* 2013.

**Schakel T.**, van Yperen G.J., van den Brink J.S., Pameijer F.A., Terhaard C.H.J., Hoogduin J.M., Philippens M.E.P.. SPLICE, a method to overcome geometric distortions in diffusion weighted imaging in head-and-neck cancer. *Proc ESTRO* 2013.

**Schakel T.**, Terhaard C.H.J., Hoogduin J.M., Philippens M.E.P.. Assessment of geometric distortions in diffusion weighted MR imaging in head-and-neck cancer *Proc. ESTRO* 2013.

**Schakel T.**, Caldas-Magalhaes J., Kasperts N., Kooij N., Terhaard C.H.J., Pameijer F.A., Raaijmakers C.P.J., Philippens M.E.P.. Validation of diffusion weighted magnetic

resonance imaging for automatic tumor delineation in laryngeal cancer. *Proc ESTRO* 2012.

Hoevenaars S., van der Heide U.A., **Schakel T.**, van Vulpen M., Philippens M.E.P.. Geometrical robustness of diffusion weighted MR imaging of the prostate. *Proc ESTRO* 2011.

Houweling A.C., **Schakel T.**, Philippens M.E.P., Roesink J.M., Terhaard C.H.J., Raaijmakers C.P.J.. Understanding xerostomia: the role of MRI to visualize early radiation-induced changes in salivary glands. *Proc ESTRO* 2011.

**Schakel T.**, Houweling A.C., van den Berg C.A.T., Roesink J.M., Terhaard C.H.J., Raaijmakers C.P.J., Philippens M.E.P.. Early and late perfusion and volume changes in salivary glands after radiotherapy monitored by MRI. *Proc ESTRO 2011.*

# Dankwoord

Het heeft even geduurd, maar met dit proefschrift is mijn promotie dan toch afgerond. Het had niet tot stand kunnen komen zonder de hulp van velen die ik hier wil bedanken.

Marielle, het begon allemaal met een afstudeerproject over speekselklieren. Ik ben blij dat je me daarna de kans bood om te beginnen aan deze promotie. Vele uren hebben we doorgebracht achter de MRI scanner en tot in de late uurtjes door gegaan om abstracts in te sturen naar congressen. In al die jaren heb ik altijd fijn met je samengewerkt en ontzettend veel van je geleerd, en ik heb veel bewondering hoe jij al je projecten en verantwoordelijkheden combineert. Ik hoop in de toekomst nog veel met je samen te werken en weer eens wat vaker samen achter de scanner te kunnen zitten.

Hans, kort na het begin van mijn promotie sloot jij aan als co-promotor. Hoewel je, net als ik op dat moment, nog niet zoveel wist van radiotherapie, was je expertise op het gebied van MRI des te groter. En dat was precies wat we nodig hadden. Dank voor al je waardevolle input en leuke discussies. Wie weet krijgen we die diffusie prepulse ooit nog eens aan de praat.

Dank aan mijn promotors, Jan Lagendijk en Chris Terhaard. Jan, bedankt voor het vertrouwen en de vrijheid tijdens de promotie. Mede dankzij de MR-Linac en alle ontwikkelingen er om heen is de afdeling een fijne omgeving voor onderzoekers. Chris, dank voor je enthousiasme, vooral rond de CORRECT studie. Onder andere via jou gaat het onderzoek in dit proefschrift zich een weg naar de klinische praktijk vinden.

Beste leden van de beoordelingscommissie, prof. de Bree, prof. Moonen, prof. Luijten, prof. Nederveen, hartelijk bedankt voor het lezen en beoordelen van het proefschrift en jullie aanwezigheid bij de promotieplechtigheid. Dear prof. Fuller, thank you very much for your time, reading and assessing the thesis and for coming all the way to Utrecht for the defense.

Mede hoofd-hals onderzoekers, in het bijzonder degene met wie ik samen aan de CORRECT studie heb gewerkt, Hans, Boris, Niels, Lisanne, Joana, Juliette, bedankt voor de goede samenwerking en leuke discussies rondom dit project.

Dank aan alle MRI laboranten van de radiotherapie voor het mede includeren en scannen van patiënten en jullie interesse in het onderzoek. Ik hoop dat ik het jullie enigszins duidelijk heb kunnen maken. Ook aan iedereen met wie ik heb samengewerkt binnen de afdeling Radiotherapie; in het bijzonder de (MRI) fysica (Rob en Nico) en ICT (Alexis en Gijs).

Alle collega-onderzoekers van Q2; Tristan, Jean-Paul, Stan, Matteo, Markus, Charis, Maxence, Ellis, Anna, Filipa, Robin, Stefan, Sjoerd, Fieke, Sophie, Soraya. Maar ook die aan de andere kant van de loopbrug, waar ik de laatste jaren verbleef; Erwin, Alex, Sander, Bart, Joep, Tijl, Martijn, Jeroen, Fredy, Dennis en andere leden van de 7T groep. Bedankt voor jullie hulp, niet alleen voor wat betreft de wetenschap, maar voor de koffie en/of bier tijdens en na het werk, zowel in binnen- als buitenland!

Arjan, Frank, Oscar, Matthew, Stefano, Alie, Christel, Kimmy, Mariska. Met jullie als mijn kantoorgenoten heb ik het altijd enorm goed naar mijn zin gehad. Bedankt voor alle hulp en gezelligheid, bij het oplossen van Matlab problemen, verpotten van planten, voorspellen van sport uitslagen, koffie zetten en tafelvoetbal. Mede door jullie ga ik altijd met veel plezier naar het werk.

Mijn paranimfen Bjorn en Janot. Naast collega's zijn jullie goede vrienden geworden. Janot, als kamergenoot zit je de laatste jaren naast me en heb je gelukkig altijd even tijd om de laatste ontwikkelingen in de voetbalwereld (of welke sport dan ook) door te nemen. Bjorn, de congressen samen waren altijd mooi, net als onze samenwerking en de biertjes tijdens carnaval. Ik ben bijzonder verheugd om jullie aan mijn zijde te hebben tijdens de verdediging! En als het een beetje mee zit dan kom ik jullie snel weer vergezellen op het voetbalveld.

Daarnaast wil ik ook graag mijn vrienden uit Boxtel, Oirschot en Best, de vrienden van Bert en de Radio Robbies/Geuken United bedanken voor alle mooie avonden, feestjes, borrels, weekenden en 3e helften.

Papa en mama, jullie zeiden laatst misschien wel dat jullie niks gedaan hadden om hier vermeld te worden, maar daar denk ik toch heel anders over. Dankzij jullie heb ik altijd kunnen doen wat ik graag wilde. Bedankt dat jullie altijd voor me klaar staan. Dennis en Lotte, ook al wisten jullie meestal niet waar het over ging, bedankt voor jullie steun en interesse in het onderzoek.

Lieve Charlotte, bedankt voor al je steun en liefde tijdens mijn promotie. Naast het promoveren hebben we al veel meegemaakt samen, mooie momenten gedeeld en prachtige reizen gemaakt. Ik kijk enorm uit naar onze toekomst samen, ik hou van jou.

# Curriculum vitae

Tim Schakel was born on June 16, 1987 in Oirschot, The Netherlands. After graduating from secondary school at the Jacob Roelandslyceum in Boxtel in 2005, he started with the Bachelor program Biomedical Engineering at the Eindhoven University of Technology. In his subsequent Master in Medical Engineering he focused on medical imaging. During this Master he did an internship at the University of Michigan's Center for Molecular imaging on diffusion weighted MRI as a biomarker for treatment response in prostate cancer. He conducted his Master thesis at the department of radiotherapy at the University Medical Center Utrecht. The subject was quantification of radiation-induced changes in the salivary glands measured with MRI.

After obtaining his Masters degree in 2011, he joined Philips Healthcare, getting more familiar with programming on the Philips MR software platform, before starting his PhD at the department of radiotherapy at the University Medical Center Utrecht in 2012. His research focus was on diffusion weighted imaging in head and neck radiotherapy. The results of his PhD research are presented in this thesis.

Tim is currently a post-doctoral researcher at the Utrecht radiotherapy department, continuing his research on diffusion weighted MRI and working on translating this towards the MR-Linac project.